



Abbreviations

AAS	Atomic Absorption Spectroscopy	HK	Knoop Hardness
AC	Alternative Current	HR	High resolution
AE	Acoustic Emission	HRTEM	High-Resolution Transmission Electron Microscopy
AES	Atomic Emission Spectroscopy	HU	Universal Hardness
AFM	Atomic Force Microscopy	HV	Vickers Hardness
AP	Archimedean Porosimetry	HVOF	High-Velocity Oxy-Fuel
BSE	Back Scattered Electrons	i.d.	Internal Diameter
CBN	Cubic Boron Nitride	IA	Image Analysis
CMAS	Calcium–Magnesium–Aluminosilicate	ICP	Inductively Coupled Plasma
DB	Double Bar method	IRS	Infrared Spectroscopy
DC	Direct Current	JCPDS	Joint Committee Powder Diffraction Standard
DCB	Double Cantilever Beam	JETS	Jet Engine Thermal Shock
D-gun	Detonation Gun	LASAT	Laser Adhesion Test
DOF	Depth of Field	MIP	Mercury Intrusion Porosimetry
DPH	Diamond Pyramid Hardness	MS	Mass Spectrometry
DSC	Differential Scanning Calorimetry	MSANS	Multiple Small Angle Neutron Scattering
DTA	Differential Thermal Analysis	ND	Neutron Diffraction
EB-PVD	Electron Beam Physical Vapor Deposition	NDT	Nondestructive Technique
EDS	Energy-Dispersive X-ray Spectroscopy	NEXAFS	Near Edge X-Ray Absorption Fine Structure
EIS	Electrochemical Impedance Spectroscopy	NS	Neutron Scattering
EN	Electrochemical Noise	OM	Optical Microscopy
EPMA	Electron Probe Microanalysis	OOF	Object-Oriented Finite Element Analysis
ESCA	Electron Spectroscopy for Chemical Analysis	P	Pycnometry
EXAFS	Extended X-Ray Absorption Fine Structure	PS	Porod Scattering
FBR	Fluidized Bed Reactor	PT	Pulsed Thermography
FCT	Furnace Cycle Test	R&D	Research and Development
FESEM	Field Emission Scanning Electron Microscope	RC	Resistive/Capacitive Circuit
FFT	Fast Fourier Transform	RCF	Rolling Contact Fatigue
FGM	Functional Gradient Material	REV	Representative Elementary Volume
FIB	Focused Ion Beam	RFPPS	RF Precursor Plasma Spray Synthesis
FTIR	Fourier Transform Infrared Spectroscopy	RPM	Rotation Per Minute
FWHM	Full-Width at Half-Maximum	RTS	Reactive Thermal Spraying
GP	Gas Permeation	RVE	Representative Volume Element
HA	Hydroxyapatite	SANS	Small-Angle Neutron Scattering
HIP	Hot Isostatic Pressing	SAW	Surface Acoustic Waves
		SAXS	Small-Angle X-ray Scattering
		SB	Single Bar Method

SCE	Standard Calomel Electrode
SEM	Scanning Electron Microscopy
SRV	Sliding, Reciprocating, and Vibrating friction
ST	Stereological Protocols
STF	Strain to Fracture
TAT	Tensile Adhesion Test
TBC	Thermal Barrier Coating
TEM	Transmission Electron Microscopy
TG	Thermo Gravimeter
TG-DTA	Thermo Gravimeter-Differential Thermal Analysis
TGO	Thermally Grown Oxide
TSR	Thermal Shock Resistance
TSS	Thermal Spray Society
URCAS	Ultrasonic Reflection Coefficient Amplitude Spectrum
USAXS	Ultrasmall Angle X-Ray Scattering
VH	Vickers Hardness
XANES	X-Ray Absorption Near Edge Structure
XAS	X-Ray Absorption Spectroscopy
XPS	X-Ray Photoelectron Spectroscopy
XRD	X-Ray Diffraction
XRF	X-Ray Fluorescence
YAG	Yttrium Aluminum Garnet
YPSZ	Yttria Partially Stabilized Zirconia
YSZ	Yttria-Stabilized Zirconia

17.1 Introduction

Coatings as most industrial products must be tested.

At the research and development scale, coatings can be characterized using techniques with varying degree of sophistication and complexity, such as nondestructive testing, metallography coupled with image analysis, materials characterization, void content, and network architecture. In a production environment, on the other hand, testing is mostly oriented toward trouble shooting and the quality control, such as adhesion–cohesion, mechanical properties, thermal properties, wear and corrosion resistance, related to coating performance under service conditions. In this chapter, a review is presented of commonly used coating characterization techniques and testing methods for R&D and industrial production scale in the thermal spray coatings industry. These are grouped in terms of techniques used and properties evaluated. Extensive references relevant to ASTM standards are given in Appendix A, where the reader can find detailed description of these techniques.

17.1.1 Differences Between Coatings and Bulk Materials

As described in Chaps. 15 and 16, thermal-sprayed coatings are made of layered splats; the contacts between splats or between splats and substrate surface correspond to small percent of the total surface of the splats, from 15% to 60%. The response of these coatings to any external solicitation will depend strongly on the mean value of these contacts. Moreover, coatings have an anisotropic behavior: for example, hardness measured at coating surface is different from that measured on its cross-section. Within splats, because of the fast quenching of the flattening melted droplets, material grain or column sizes are rather small (below 0.5 μm in diameter). The coating adhesion is either mechanical, as in most cases, or chemical for few specific sprayed materials associated with specific substrates, or metallurgical, that is, controlled by diffusion when metal coatings are plasma sprayed in soft vacuum on hot metal substrates where the oxide layer has been removed. The coating adhesion to substrate is generally below 70 MPa for mechanical adhesion and much higher for diffusion-controlled adhesion. Sprayed coating properties are also lowered by various defects such as pores and the inclusion of unmelted particles.

Wrought, forged, cast, or sintered metal materials have, on the other hand, quite different properties. For materials prepared by metallurgical processes, grain sizes are larger (a few micrometers, that is, 10–100 times that of coatings) due to much lower cooling rates and also heat treatments to achieve specific precipitates. Tensile strengths are generally much higher than that of coatings, from a few hundreds to thousands or more MPa. For sintered engineering ceramic materials, grain sizes (about 0.6–14 μm) are larger than those of thermal-sprayed coatings and if tensile strengths are lower (hundreds MPa) than those of bulk materials, they are still higher than those of coatings.

17.1.2 Characterization and Testing Methods Used for Coatings

The first characteristics that are important and necessary are those related to the coating microstructures at different depths. According to Pawlowski L. (1995), they involve:

- Chemical composition at macro- and microscales
- Grain or column morphology and orientation (texture)
- Defects such as voids, unmelted particles, micro- and macrocracks, and dislocations with their number and distribution

For such characterizations, in most cases, the critical step is the metallographic examination. However, the heterogeneous or composite nature of the thermal spray coating can render the choice of a metallographic preparation protocol to be used rather difficult. According to Riggs W (2004), and Wigren J and K Täng (2007), the observed coating microstructure can vary significantly depending on the protocol used for sample preparation. For example, they cited the evaluation of plasma-sprayed WC/Co coatings sprayed by one supplier and the corresponding metallographic preparation by 27 laboratories that resulted in a wide range of observed properties. Sample mounting technique, whether hot and cold under vacuum, may be the single most important step in the whole metallographic procedure that can have a significant impact on the observed sample microstructure. Improper grinding and polishing can also be the source of many problems as well as the measurement system analysis using image analysis [Wigren J and K Täng (2007)].

Testing methods make it possible to determine properties such as coating adhesion–cohesion, mechanical and thermal properties, or service properties such as wear and corrosion resistance. However, the test results can also depend on the sample preparation techniques. For instance, the adhesion–cohesion test results depend strongly on the penetration of epoxy and pressure used during curing, e.g., the tensile strength of Ni–5Al/Alumina system was found to vary from 60 down to 15 MPa [Wigren J and K Täng (2007)]. However, when the coating was dense enough to prevent the penetration of the glue, this variation in tensile results was not observed. Such tests must be as close as possible to real-world coating service conditions to be used at the production stage. In addition, they should be rapid to operate and easy to be used by less skilled personnel. Generally, test methods consist in observing or measuring the response of coatings to various external solicitations: loads, stress, applied electric signals, or other stimuli [Wigren J and K Täng (2007)]. The coating response depends on its physical, chemical, and structural properties that in turn depend to a great extent on the real contacts between splats. To characterize a specific coating property, the coating response to the applied stimulus must be sufficiently important and clear to be measured. For example, when applying a load, the response of the coating can be purely elastic or plastic or both and it must be known to interpret correctly the response signal.

The result of every test is practically a number: size of a print for hardness, percent of porosity, and thermal signal propagation for thermal diffusivity. The numbers obtained from tests are supposed to be representative of the studied property. However, numbers are useful only if a certain degree of confidence in them is achieved [Riggs W (2004), Wigren J, Täng K (2007) and Wigren J, Johansson J (2011)]. The degree of confidence is usually expressed statistically based on the results of a significant number of tests, being

highest if a minimal variance or standard deviation from the average value is obtained. For example, a hardness of 400 HV under a load of 5 N is meaningless: the design engineer will be satisfied if this value is $400 \pm 20 \text{ HV}_5$ and very disappointed if it is $400 \pm 150 \text{ HV}_5$.

17.1.3 Statistical Methods

Samuel Clemens wrote: “there are three kinds of lies: lies, damned lies, and statistics.” It underlines that statistical methods to characterize sprayed coating properties must be used properly. The complexity of coating structures, their anisotropy implying to consider the measurement directions, their strong dependence on spray conditions and powder characteristics, and the generally wide scatter in different property values make it necessary to perform statistical analysis when determining coating properties. This will be illustrated for microhardness, which is a basic mechanical property as elastic modulus. They are used to characterize the performance of coatings as they affect the erosion wear-resistance performance, stress–strain behavior, contact stress field, coating delaminating, coating fracture, and residual stress state within coatings [Li J, Ding C (2001)]. However, hardness data are often presented in the literature as a single numerical statistic value without any details of how such a value was obtained, which is meaningless.

The measuring equipment, a factor that can affect hardness measurement, must be, as for any type of measuring equipment, tested regularly in order to avoid systematic errors and biases. The coating surface or cross-section preparation is a nonnegligible parameter. The load also is very important because the indenter penetration increases nonlinearly with it (plastic deformation increases with load). To achieve comparable results, the same load must be used with the same time of application. The indentation size effect is of little significance [Factor M, Roman I (2000a, b)] when comparisons are made between samples while keeping the load constant. Indents should only be discounted if there is reason to believe that the measurement is invalid, such as if the testing equipment suffered vibration during the test. Disqualification of outliers to get a “statistically more meaningful result” is not legitimate if, as is usually the case, these represent true variation of the coating structure. Microhardness indentation is also subject to systematic biases between operators that limit the reproducibility of the technique. As it could be expected, these biases increase significantly when the indent size is decreased [Factor M, Roman I (2000a, b)]. Since they may be more important for low loads and high hardness materials, the hardness data reported in the literature for ceramics materials and cemented carbides are not necessarily sound.

Statistically, Normal, Lognormal, and Weibull distributions are widely used to fit experimental data with

“Normal” and “Weibull” distributions being mostly used to characterize thermal-sprayed coatings [Walpole RE, Myers RH (1978), 17.S1].

17.1.3.1 Normal Distribution

In laboratories when considering N events, x_i , such as for example, indents, the largest and the smallest values are discarded, before averaging the $N-2$ remaining values. The standard deviation, σ , is the square root of the average value of $(x - \eta)^2$, where η is the arithmetic mean of the measured values. In the case where x takes random values from a finite data set x_1, x_2, \dots, x_N , with each value having the same probability, the standard deviation σ , is given by;

$$\sigma = \sqrt{\frac{1}{N} \sum_{i=1}^N (x_i - \eta)^2} \quad (17.1)$$

However, the central limit theorem says that the distribution of a sum of many independent, identically distributed random variables tends toward the famous bell-shaped “normal distribution” with a probability density function proportional to $\exp(-(x - \eta)^2/2\sigma^2)$, which is a Gaussian distribution. Therefore, the standard deviation is simply a scaling variable that reflects how broad the curve will be. When the data distribution is approximately normal then about 68% of the data values are within \pm one standard deviation of the mean value (mathematically, $\eta \pm \sigma$, where η is the arithmetic mean), about 95% are within \pm two standard deviations ($\eta \pm 2\sigma$), and about 99.7% lie within ± 3 standard deviations ($\eta \pm 3\sigma$).

However, the assumption of normal distribution is not always fulfilled for nonhomogeneous materials, such as thermal-sprayed coatings, where the dimensions of the microstructural features have a similar order of magnitude than that of the indent depth. In general, flaws such as subsurface porosity, brittleness, and trapped fine particles will result in larger indents, thus producing right- or positively skewed hardness distributions [Walpole RE, Myers RH (1978)]. For an asymmetrical dataset, Weibull distribution is more appropriate than Gaussian distribution. Lin CK and CC Berndt (1993) were among the first to demonstrate that for yttria partially or totally stabilized thermal spray coatings, Weibull statistic is more appropriate.

17.1.3.2 Weibull Statistic

The Weibull distribution function is given by the following equation:

$$F(x, \lambda, m, \delta) = \frac{m}{\lambda} \left(\frac{x - \delta}{\lambda}\right)^{m-1} \exp\left(-\left(\frac{x - \delta}{\lambda}\right)^m\right) \quad (17.2)$$

where x is the variable, $m > 0$ is the shape parameter, $\lambda > 0$ the scale parameter, and δ the offset.

In materials science, m , the shape parameter is called Weibull modulus. By plotting $[\ln(\ln(1/(1 - F(x - \delta))))]$ versus $[\ln(x - \delta)]$ using a linear regression least-squares fit to calculate the slope and intercept of the best fit straight line, the parameters of the distribution function can be determined [Factor M, Roman I (2000a, b)]. Very often the offset δ is assumed to be zero and the three-factor Weibull distribution is simplified to a two-factor one. “However with modern spreadsheets allowing linear regression and giving the coefficient of determination (r^2 statistic) automatically, finding the offset δ that gives the best fit is trivial, as is the subsequent calculation of the other parameters for this best-fit case” [Factor M, Roman I (2000a, b)]. When measuring Vickers microhardness $HV = x$, and $(HV - dH)$ is the characteristic hardness with 63.2% of data points expected to be below this value, and m describes the shape of the distribution. The Weibull distribution is equal to or approximates several other distributions, depending on the value of m . For $m = 1$ exponential distribution, $m = 2$ Rayleigh distribution, $m = 2.5$ lognormal distribution, $m = 3.6$ normal distribution, and $m = 5$ peaked normal distribution. It must be underlined that Factor M, Roman I (2000a, b) are not favorable to the discounting of lowest and highest values since it affects measures of spread such as the range and standard deviation. This also tends to increase the calculated averages, as the data for most coatings are not normally distributed.

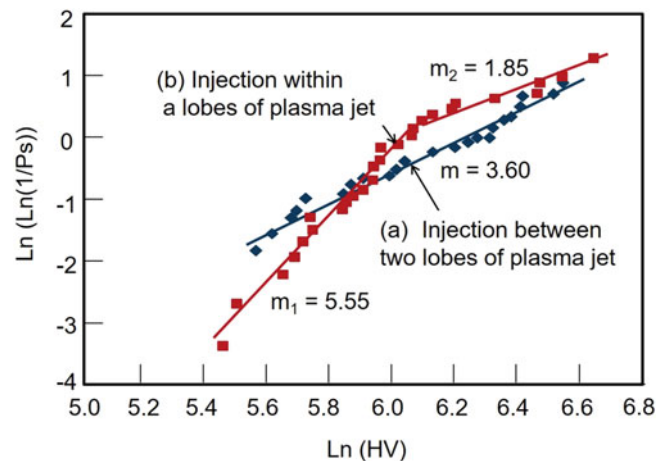


Fig. 17.1 Statistical analysis by microhardness Weibull distribution for lanthanum manganite doped with strontium ($\text{La}_{0.8}\text{Sr}_{0.2}\text{MnO}_3$: LSM) coatings plasma spraying using Triplex II Pro torch anode nozzle i.d. 6.5 mm, $I = 400$ A, 50% He (a) injection between two lobes of plasma jet and (b) injected within a lobe of plasma jet [Brousse E (2010)]. (Reprinted with kind permission from Dr. E. Brousse)

An example of Weibull distributions from Brousse E (2010) is presented in Fig. 17.1 for lanthanum manganite doped with strontium, $\text{La}_{0.8}\text{Sr}_{0.2}\text{MnO}_3$, (LSM), coating plasma sprayed using Triplex II Pro torch with an anode nozzle i.d. 6.5 mm, $I = 400$ A, 50% He. The powder used was in the form of micrometer-sized particles made of agglomerated nanometer-sized grains. With this type of particles when the spray conditions are properly adjusted, coatings are made of nanometer-sized areas imbedded within micrometer-sized ones. Thus, the coating hardness depends strongly on locations where measurements are performed: low values in the nanometer-sized zones and high ones in the others. In Fig. 17.1a, the spray conditions were not optimized and only one Weibull modulus was obtained, most sprayed particles being fully melted, while in Fig. 17.1b two Weibull distributions were obtained with the adapted spray conditions resulting in unmelted zones imbedded within fully melted ones. It must be underlined that Weibull distribution is the only way to characterize properly coatings with bimodal distributions.

17.1.3.3 Variance

An important issue when calculating a statistical distribution is the number of data to be considered to have a reliable distribution. It can be determined by calculating the variance according to the number of events, N , taken into consideration. The variance is defined by the mean value of $(x - \eta)^2$, which is very simply calculated, if all events have the same probability, by $(x - \eta)^2/N$.

For the above given example of plasma spraying of lanthanum manganite doped with strontium, $\text{La}_{0.8}\text{Sr}_{0.2}\text{MnO}_3$ (LSM), coating using a Triplex II Pro, the Vickers hardness results given in Fig. 17.2 after Brousse E (2010) were

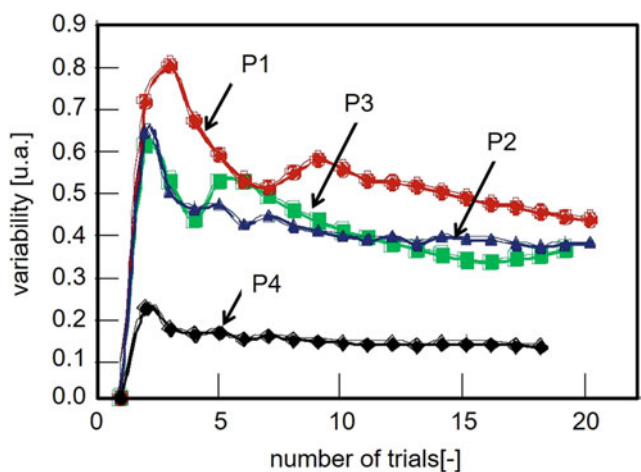


Fig. 17.2 Evolution of the variability of the Vickers hardness for lanthanum manganite doped with strontium, $\text{La}_{0.8}\text{Sr}_{0.2}\text{MnO}_3$ (LSM), coating sprayed using Triplex II Pro, 400A, with different spray conditions [Brousse E (2010)]. (Reprinted with kind permission from Dr. E. Brousse)

obtained for different spray conditions [(P1): $d_a = 6.5$ mm, Ar 60 slm, (P2): $d_a = 6.5$ mm, Ar 58 slm + He 19 slm, (P3): $d_a = 6.5$ mm, Ar 54 slm + He 54 slm, and (P4): $d_a = 9.0$ mm, Ar 60 slm]. These show that with the spray conditions P4 (torch with a 9-mm internal diameter anode nozzle) all particles were melted corresponding to the highest hardness 773 ± 55 HV₃, and the variance was stabilized with a low number, 5, of measurements. On the contrary with the other spray conditions, the coating hardness was lower (in a ratio of almost twice) with rather large standard deviation and, as shown in Fig. 17.2, the variability was more important (about 0.5 against 0.2 for conditions P4) and a stable value was reached only for 12–14 indents.

17.2 Nondestructive Methods

Simple, fast, reproducible nondestructive coating test methods are one of the dreams of sprayers. If significant progress was achieved at the R&D level, relatively few techniques have been implemented in coating industry. This is probably due to the very complex structure of thermally sprayed coatings that is very difficult to interpret through the signals of nondestructive techniques (NDT). The different devices developed in R&D and industry are summarized in the ASM handbook about “Nondestructive Evaluation and Quality Control of Materials and Manufactured Parts” [ASM International (2007)] and the ASTM reference [17.ND1]. The few devices that can be used for thermal spray coatings are summararily presented below.

17.2.1 Visual Inspection

Visual inspection allows detecting and examining a variety of surface flaws due to corrosion, contamination, delaminating, quality of surface finish, and discontinuities. It comprises image sensors for visual records, magnifying systems, dye and fluorescent penetrants, and magnetic particles for enhancing the observation of cracks or defects. Flexible or rigid boroscopes for illuminating and observing internal, closed, or otherwise inaccessible areas [ASM International (2007)] while indispensable for a variety of applications are not very useful for coatings. A boroscope is an optical device consisting of a rigid or flexible tube with an eyepiece on one end and an objective lens on the other linked together by a relay optical system in between. The optical system is usually surrounded by optical fibers used for illumination of the remote object. An internal image of the illuminated object is formed by the objective lens and magnified by the eyepiece.

17.2.2 Laser Inspection

Laser-based measurement systems are used for dimensional measurements and surface inspection of coating. The following techniques are commonly used for dimensional measurements:

- Scanning laser gage with a precision as high as $\pm 0.25 \mu\text{m}$ for parts with dimensions in the range of 10–50 mm. Lower accuracy is to be expected for larger parts.
- Laser triangulation sensors. They measure the standoff distance between a surface and a microprocessor-based sensor providing quick measurements of deviations due to changes in the surface. With two sensors the part thickness or the inside diameter of bores can be measured.
- Surface inspection to detect surface flaws and roughness.

17.2.3 Coordinate Measuring Machines

These provide accurate and flexible 3-D inspection, in-process, before coating, and finished parts, for example, with the coating after machining or rectification. They are normally used in production scale manufacturing facilities, see [ASM International (2007)] for details about the method.

17.2.4 Machine Vision and Robotic Evaluation

A machine vision, also computer vision, includes both visual-sensing and interpretive capabilities allowing identifying shapes, measuring distances and ranges, gaging of sizes and dimensions, determining orientation of parts, and detecting surface shading [ASM International (2007)].

17.2.5 Acoustic Emission

Acoustic emission (AE) is often produced by sudden movement in stressed material due to crack growth and/or plastic deformation. In most cases, the rapid release of energy from localized source within coating or bulk material [Noone MJ, Mehan RL (1974)] produces a stress wave radiated into the structure that can be detected by a sensitive piezoelectric transducer judiciously positioned. It is generally difficult, however, to separate the AE events related to elastic and plastic deformation, and to directly correlate the nature of cracking with the level of AE energy. Multilinear regression analysis of the number of AE events can be helpful to correlate to the spray parameters [Kucuk A et al. (2000b)]. The Weibull modulus of the energy released during four-point bend test can be calculated [Lin CK, Berndt CC (1998)].

AE analysis has been successfully used to monitor cracking in ceramic coatings during mechanical testing such as in four-point bending [Kucuk A, et al. (2000b), Lin CK, Berndt CC (1998) and Lin CK, et al. (1997)] or under thermal cycling conditions [Berndt CC (1985), Voyer J, et al. (1998), Andrews DJ, Taylor JAT (2000) and Robin P, et al. (2010)]. When studying the effect of thermal cycling, the AE behavior monitoring during the heating and cooling periods of a thermal cycle must be separated. These periods show different stress ranges that correspond to different crack lengths and, therefore, correspond to different stress intensity factor ranges that Andrews and Taylor (2000) and Robin P et al. (2010) have used AE as a quality control test for TBCs, as the test is relatively fast and the data can be handled easily by a microprocessor. The test specimens were commercially sprayed straps. The data showed that differences in spraying parameters and microstructure were clearly visible in the emissions during the first thermal cycle.

Recently, Zhao et al. (2010) have extended the ultrasonic coefficient amplitude spectrum (URCAS) to obtain the coating thickness and its longitudinal velocity at the same time on thick substrates. A model was set up first to represent the ultrasonic waves reflected from a coating system at normal incident. Then, an inverse algorithm based on the Gauss–Newton method was introduced to determine the thickness and velocity by comparing the theoretical and measured URCAS. Experimental validation was performed on the inhomogeneous ZrO_2 –7 wt% Y_2O_3 (YSZ) coatings on super alloy substrates. The relative errors of the thickness and velocity measurement were in the ranges of 5.33–5.96% and 8.95–9.66% for YSZ coatings. It seems that the URCAS combined with inversion technique can be applied to obtain the thickness and longitudinal velocity of coatings simultaneously.

17.2.6 Laser Ultrasonic Techniques

Nondestructive ultrasonic techniques have been used to determine the elastic constants, such as Young's modulus and Poisson's ratio, of a variety of bulk materials [Boccaccini DN, Boccaccini AR (1997), Asmani M, et al. (2001)]. It is difficult, however, to measure the elastic properties of thermal spray coatings by conventional ultrasonic techniques due to the porosity and extensive micro cracking. The laser ultrasonic technique uses surface acoustic waves (SAWs) or Rayleigh waves, propagating along the surface of a material, to obtain information about it. SAWs are generated by the instantaneous local thermal expansion, laser ablation, or high-intensity pulsed ion beam. As the wave motion is concentrated near the surface, it makes SAWs interesting for testing coatings [Ma XQ, et al. (2001a, b)] or thin films. The surface waves are generated and detected at lengths

much greater than the dimension of the coating thickness, and the coating thickness-to-wavelength ratio is the key parameter for the penetration depth of the material [Lima RS, et al. (2003a, b)]. A laser pulse can generate simultaneously many wave modes. The laser and its wave detection are performed on the same surface, but at different places, two types of ultrasonic waves, surface longitudinal and Rayleigh wave velocities, permit measuring Young's modulus, E , and Poisson's ratio, ν . E and ν values measured by Knoop indentation were in good agreement with those obtained with laser ultrasonic technique for titania coatings plasma and high-velocity oxy-fuel (HVOF) sprayed coatings [Lima RS, et al. (2003a, b)]. The titania coatings exhibited significantly different Poisson ratio, ν , values, although they had very similar E values. The E values measured on the cross-section of WC-Co coatings agreed well with those measured via laser ultrasonic.

Laser (nanosecond pulsed) ultrasonic has also been used for the nondestructive characterization of ceramic coatings (alumina) and the estimation of their adhesion strength on metallic substrates [Rosa G, et al. (2001)].

17.2.7 Thermography

Measuring the coating thickness is not necessarily straightforward technique that is used to detect spatial variations in the measured surface temperature pattern. Thermography reveals flaws by searching anomalous hot spots after thermal excitation. Two types of thermography inspections are used: passive and active. Passive thermography measures the variation of surface radiation to identify anomalous regions. Active thermography uses a controllable thermal source to excite the testing object and reduces the environmental influence such as ambient conditions and emissivity variations [Hung YY, et al. (2009)]. The most efficient thermal tests are the dynamical or active ones, which can detect the presence of subsurface detachments by monitoring the evolution of the coating temperature during a thermal transient pulse. Pulsed thermography (PT) is used today for the inspection of the manufacturing quality of coatings immediately after their deposition. Because of its speed and simplicity, PT allows the design of an automatic inspection procedure for factory quality control [Maldague X, Marinetti S (1996), Shepard SM (2001)].

When performing in-field tests on thermal barrier coatings (TBCs) deposited on gas turbine blades, the main problem encountered is the difficulty to correctly interpret the experimental data. Marinetti S et al. (2007) have defined a procedure to reliably discriminate thickness changes and real defects, and presented and discussed preliminary results. Their approach was based on the analysis of the apparent effusivity profile.

17.2.8 Coating Thickness

Measuring the coating thickness is not necessarily straightforward and the method for thickness evaluation can also be questioned. Wigren J and K Täng (2007) have considered the thickness evaluation of Ni-5Al plasma-sprayed coating. For that they compared two microscope techniques (average and maximum readings) and two types of micrometer (flat and ball end). Thicknesses were given stroke by stroke (two passes) during the coating buildup. A 50 μm thick metallic coating measured with flat micrometer did not have full metallographic coverage in the above investigation, whereas 50 μm measured with a ball end micrometer did. Important differences in thickness measurements were observed. The measurement tool (flat or ball point micrometer) used for thickness measurements had a significant effect on the reading as well as the microscope techniques [Wigren J, Täng K (2007)].

17.3 Metallography and Image Analysis

Metallography is a critical step to characterize coatings. Sometimes, surfaces are rougher than the original grit-blasted surface, which is especially the case for porous and loose structures such as those observed with certain flame-sprayed coatings. Compared to bulk materials, coating preparation for metallographic examination is rather complex. This is due to coating microstructure that is made of layered splats with porosities and the occasional inclusion of unmelted particles. Ceramic coatings are more brittle than bulk-sintered ceramic materials, mixtures of hard and soft materials in cermets, and mixtures of many phases. All these features offer a challenge for conventional metallographers. In the chapter "Metallography and Image Analysis" by Riggs W (2004), an excellent illustration of the metallographic procedure for a WC-Co coating is given. Pullout of particles during coating preparation for metallographic examination represents one of the main problems that is met especially for cermet coatings. According to Van der Voort GF (1999), George Vander Voort (ed) (2004), Geels K (2007) and 17.Me1-17.Me3 properly prepared metallographic surfaces must meet the following criteria:

- Removal of deformation zone produced during rough polishing
- Be flat and free from scratches, stains, and other imperfections
- Keep all nonmetallic inclusions intact
- Show no chipping or galling of hard and brittle intermetallic compounds
- Be free from all traces of disturbed metal

17.3.1 Coating Preparation

17.3.1.1 Sectioning

The first step of metallographic preparation is sectioning either to reduce the specimen size or to examine its cross-section or both. Of course, the process must not alter the microstructure through generated heat and deformation. Because of the generally good resistance of the coatings to compressive loads and their poor resistance to tensile ones, cutting must be performed from the outermost layer of coating, inward, and then through the coating and not the reverse [Riggs W (2004)]. To limit the flaws created by cutting, the specimen can be first encapsulated in a cold mount-type epoxy before sectioning, which is an excellent technique though rather time consuming.

(a) Abrasive Cutting

This is probably the best solution to eliminate or limit heat generation and deformation during the cutting of the sample. The cutoff machine and abrasive wheels must be matched. Diamond, alumina, and silicon carbide are among the most commonly used abrasives depending on the material to be cut. Independently of bond hardness, the coarser grit size produces the harder action, while finer grits result in a softer action and a smoother surface. The bonding material holding abrasive grains in place is made of either resinoid for dry cutting or rubber for wet cutting. Softer bonds are used to cut hard materials, while harder ones are used to cut soft materials. As already emphasized, the proper cooling of the coating during the cutting process is very important and can be achieved using high volume jets or submerged cutting. The cutting speed is also an important parameter and must be adapted to the wheel dimension used.

For thermally sprayed coatings, Antou G, Montavon G (2007) recommended:

- Cutting speed, that is, the speed of the cutting abrasive surface, should be of the order of a few hundred meters per minute.
- Transverse speed should vary between 0.01 and 0.1 mm/s. It is suggested, when possible, to select the lowest possible transverse speed and to use a device in which the cutting speed can be adjusted rather than the cutting load, since in this latter case the cutting speed varies along the sample.
- Water or oil has to be used as lubricant.

Sauer JP (2005) on behalf of the Thermal Spray Society (TSS) Committee on Accepted Practices has also presented the best practices recommendations for sectioning sprayed coatings.

(b) Precision Sectioning

For small parts with a diameter in the range of 75–125 mm, diamond or CBN (*Cubic Boron Nitride*) rimmed wheels are used. Their speed range extends from a few to 1000 rpm and the load range, if possible controlled electronically, varies from a few tenths to ten Newton. The technique gives excellent results for most coatings, but it is rather slow.

To conclude this part applying the following motto is recommended: “Better spend more time for cutting the sample, this will result in reduced polishing time and in less damage to the structure.” For more details about cutting, see [Riggs W (2004), George Vander Voort (ed) (2004)] as well as the recommendations of cutoff machine manufacturers.

17.3.1.2 Mounting

Metallographic samples are mounted to facilitate their manipulation, protect the coating and preserve all of its features during its sectioning and polishing preparation. According to Riggs W (2004), the role of the mount is to:

- Not only ease their gripping by hand or automatic devices but also firmly hold the specimen.
- Avoid damaging the specimen, for example, by a too high temperature or pressure.
- Penetrate and fill nonoccluded (surface-connected pores) without modifying their original size and shape and also minimizing pullout during grinding and polishing.

Mounting involves essentially the encapsulation of the coated sample in polymeric mounts. Two principal techniques are used:

- Hot mounting process: The compression molding technique consumes the minimum amount of time. It uses thermosetting and thermoplastic materials. The first one requires heat and pressure during the molding cycle and can be ejected at maximum molding temperature. Thermoplastic materials remain fluid at maximum molding temperatures and become dense and transparent with a decrease in temperature and an increase in pressure.
- Cold mounting process: Neither heat nor pressure is applied. The sample is placed in a plastic or rubber cup with epoxies, polyesters, and acrylics all comprising a resin and a hardener. An exothermic reaction occurs during polymerization and thus the mixing by volume or weights of both components is critical. Epoxies and polyesters are transparent, whereas acrylics are opaque. Epoxy can fill pores if the gas they contain is evacuated. It can be achieved by, if necessary, heating the samples to get rid of water vapor and then by placing the samples in soft vacuum at a pressure such that the boiling of the epoxy is avoided and during 10 min at least. Vacuum

impregnation with a suitable liquid epoxy produces non-porous samples well consolidated and rigid. With this technology, it becomes possible to distinguish between oxide stringers and delaminations.

According to Wigren J and K Täng (2007), “The choice between hot and cold (vacuum) mounting may be the single most important step in the whole metallographic procedure.” True microstructure features (cracks and porosities) that never were seen previously are now revealed with cold mount techniques using low viscosity epoxies. The penetration of epoxy during mounting is also crucial for the following steps in the metallographic procedure, especially the grinding step. Mounting defects such as cracking at the corners, bulging in phenolics, soft mounts, and also porous and friable areas (hot mounts), or bubbles (cold mounts) must be strictly avoided.

For more details, see George Vander Voort (ed) (2004), Geels K (2007), Antou G, Montavon G (2007), Sauer JP (2005), Sauer JP, Blann G (2006), Puerta DG (2005) (2006) as well as the recommendations of cutoff machine manufacturers.

17.3.1.3 Grinding

The prepared metallurgical mount is then subjected to a series of grinding and polishing steps in order to achieve a surface suitable for observation at both low and high magnification, see [Riggs W (2004)]. Of course, the grinding procedure depends on the grinded material properties such as hardness and ductility and it must be adapted to each one. The role of grinding, then followed by polishing, is to produce samples with:

- True and undisturbed microstructure.
- Scratch (polishing artifact) must be limited to dimension below those observable at a given magnification.
- Flat specimen with edge rounding: using a polishing surface with high resilience will result in material removal from both the sample surface and the sides. The effect of this is edge rounding and can be seen with mounted specimens if the resin wears at a higher rate than the sample material.

Of course, the process parameters, including the coolant lubricant, must be such that overheating does not occur; the high temperatures generated in the grinding zone can cause different types of thermal damages. Wigren J and K Täng (2007) have underlined that many problems can arise from improper grinding/polishing. By far, one of the biggest issues in grinding is the smearing caused by the SiC papers. The most critical are the unfilled pores and cracks in a metallic coating. Long polishing, while sometimes necessary because of damage created by the grinding steps, can also bring

forward another problem of edge retention, which causes metallic coatings with oxides and pores to be distorted. The width of pores and oxides can also be enlarged. Ceramic coatings can cause other grinding/polishing issues as discussed by Wigren J and K Täng (2007).

The first grinding is the course, one, the purpose of which is to remove the deformation produced during sectioning and achieves a flat surface. It also removes gross amounts of surface material for the micro-sample preparation. The process is performed with abrasive belts or disc-covered rotating wheels and generally water as coolant, which also flush away the surface removal products. In most cases, the abrasive used is alumina or silicon carbide with grit sizes between about 350 and 80 μm . The abrasive action, depending also on the grinding speed, is very aggressive. For more details, see [Puerta DG (2006)] on behalf of TSS Committee on Accepted Practices.

The second grinding is fine grinding performed, generally in wet conditions, with bonded grains of alumina, silicon carbide, and emery. Prepolishing diamond structured discs with diamonds in the size range 3–15 μm can also be used.

A detailed description of grinding materials and process parameters is given by [W. Riggs (2004)] including grinding rates, grinding deformation, and finally material response to (pressure, abrasive type, abrasion fluid, and grinding time).

17.3.1.4 Polishing

The main objective is to remove the abrasion damage layer (plastically deformed material, scratches, slip/twin/shear damage layer immediately beneath the surface) produced by the grinding process. The material removal is achieved with either rolling abrasive particles or fixed abrasive particle. To minimize the time and labor, interchangeable revolving disks are used, each of which covered with emery paper, cloth, or parchment, according to the stage of polishing for which it is required. The abrasive used should permit accurate sizing, which is the case of diamond abrasives that also have a high hardness, a low coefficient of friction, and excellent inertness. They produce uniform and high rate of material removal with very few induced surface damage. Typically, 6- μm mean size is used to achieve the highest removal rates for most materials (rough polishing), the removal rate decreasing very fast for smaller sizes. The type of cloth used is very important for the end result. The final polishing stage removes any deformation zone resulting from the rough polishing. For this polishing, a wide variety of abrasive materials can be used: alumina, chromium oxide, magnesium oxide, colloidal silica, and diamond, with sizes generally around or below 1 μm . The coating materials that are trickier for grinding and polishing are ceramics and cermets. For details about polishing see the Metallography chapter of W. Riggs (2004) or Van der Voort GF (1999), George Vander Voort (ed) (2004), Geels K (2007), Antou G,

Montavon G (2007), Sauer JP (2005), Sauer JP, Blann G (2006), Puerta DG (2005) (2006) or the recommendation of polishing machine manufacturers.

Antou G, Montavon G (2007) recommended to:

- Use semi- or automatic-polishing machine for a higher reproducibility of the operation.
- Adjust independently the load on each sample to polish a given coating nature at the appropriate pressure regardless of the sample size.
- Select identical directions of rotation for the samples and the abrasive support to avoid damage by spallation.

Wigren J and K Täng (2007) underlined that very often long polishing times are necessary, because of the damage created by the grinding steps, especially for ceramic coatings.

17.3.1.5 Etching

Etching is the operation to reveal the microstructural features (grain boundaries, phases, precipitates, and other microstructure constituents) of the polished specimen. Etching is achieved through selective chemical attack of the surface. To prevent uneven attack and stains, especially after polishing, the specimen must be washed and degreased and then cooled in running water before being etched. Etching is performed by immersing the clean specimen in the etching reagent, for a given time, followed by its rapid rinsing in running water and drying. The etching reagent is chosen according to the material to be etched. For example, Nital reagent (2 vol.% of nitric acid in alcohol) is used for steels and cast iron. Electrolytic etching involves the enhancement of standard acid etching by electric current. Many etchants have been developed to reveal the structure of metals and alloys, ceramics, carbides, and nitrides with some etchants revealing the general microstructure of the coating, while others may be selective to certain phases or constituents. For details, see George Vander Voort (ed) (2004), Geels K (2007).

17.3.1.6 Focused Ion Beam

The use of focused ion beam (FIB) is a relatively “high end” surface preparation technique developed in the semiconductor industry. It is similar to SEM, but instead of using electrons it works with a focused ion beam. Ions, being far heavier than electrons, have a high momentum though are much slower than electrons [Giannuzzi LA, Stevens FA (2004)]. As the ion beam hit the surface of the coating, it will remove atoms from the coating and/or substrate. Depending on the beam position, dwell time, and size material, removal is locally controlled in a highly controlled manner, down to the nanometer scale. As with conventional cutting and polishing techniques, ion beams can also produce surface damage and implantation that can be minimized by

FIB milling with lower voltage. For thermally sprayed coatings, FIB milling is essentially the only mean allowing studying the contact between a splat and the substrate since the conventional means described earlier are too aggressive and, in most cases, lead to the separation of the splat from the substrate. FIB can also be used to prepare thin TEM samples in the 100th nm range.

17.3.1.7 Examples of Conventional Coatings Preparation

The Thermal Spray Society (TSS) has carried out round Robin tests for the metallographic preparation of two conventional thermal-sprayed coatings [Puerta DG (2008)] (<http://asmcommunity.asminternational.org/portal/site/tss/>):

- Molybdenum coating with some oxide content after spraying in air.
- Ni-4Cr-4Al/Bentonite coatings containing metallic and nonmetallic phases with a high porosity level (up to 40%).

Mo coatings are intensively used in aerospace industry and also automotive, marine, and heavy industries. For these coatings, vacuum impregnation with a low-viscosity cold mount epoxy is the recommended mounting method. The amount of material, which must be removed, depends on the sectioning methods employed. All accepted practice preparation procedures utilized combined diamond steps totaling a minimum of 5 min.¹ For abrasible coating, the possibility to pullout during metallographic preparation is very high as to the elevated porosity with nonmetallic phases generally loosely bonded. Most laboratories identified vacuum impregnation of a castable epoxy as a critical step to ensure such a coating integrity during preparation.²

17.3.2 Microscopy

17.3.2.1 Optical Microscopy

Optical microscopy (OM) examination is the first instrument to be used for metallographic observations because it is faster and much less expensive than scanning electron microscopy (SEM). OM covers a large area; the contrast at magnification below 500 is better than that of SEM and can give the natural color of the specimen. In most cases, magnifications are between 50 and 1000×. However, with some microscopes, it becomes possible to perform examination at higher magnifications, for example, 2000×, and even higher, as

¹ ASM Thermal Spray Society (TSS), Accepted Practices Committee on Metallography Accepted Practice–Molybdenum Thermal Spray Coatings, see [Puerta DG (2008)].

² ASM Thermal Spray Society (TSS), Accepted Practices Committee on Metallography Accepted Practice–NiCrAl/Bentonite Abradable Coatings, see [Puerta DG (2008)].

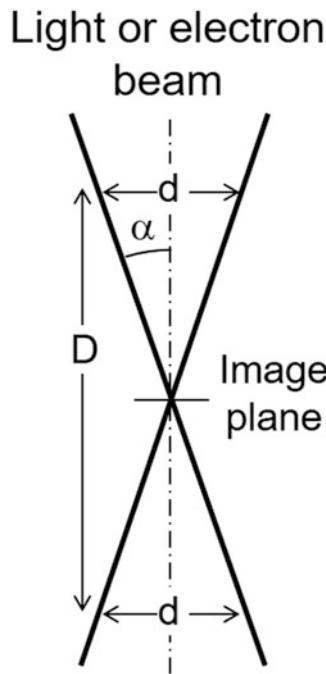


Fig. 17.3 Scheme of the depth of field in optical microscopy

long as diffraction fringes are not present to distort the image. The resolution limit of the OM is at the best about 0.2–0.3 μm . If necessary, special objectives allow using OM at magnifications below 50 \times . One of the key parameters is image contrast, which depends, on one hand, on the quality of the optics, coatings on lenses, and reduction of flare and glare, and, on other hand, on proper specimen preparation and, if necessary, good etching techniques. The important characteristic of OM is the depth of field, D , area in which the specimen that will be in acceptable focus. Figure 17.3 presents a scheme of the depth of field, D , which can be calculated simply by

$$D = \left(\frac{d}{\tan \alpha} \right) \quad (17.3)$$

where α is the beam half angle and d its diameter at the depth of field (DOF) position.

Using optical microscopy, the depth of field is the weak point, with D values typically in the micrometers range or below, for example, $D = 5 \mu\text{m}$ for a magnification of 20 corresponding to a resolution of 5 μm , and $D = 0.7 \mu\text{m}$ for a magnification of 200 corresponding to a resolution of 0.5 μm .

Most observations are performed with bright field illumination where the image of any flat feature perpendicular to the incident light path is bright or appears to be white. Dark field provides higher contrast images and greater resolution than bright field. The light from features perpendicular to the

optical axis is blocked and appears dark, while the light from features inclined to the surface appear bright. Polarized light is also used when studying the structure of metals with noncubic crystal structures. Tint-etched surfaces, where a thin film (such as a sulfide, molybdate, chromate, or elemental selenium film) is grown epitaxial on the surface to a depth where interference effects are created, when examined with bright field, produce color images. The process can be improved with polarized light. Another imaging mode is differential interference contrast that converts minor height differences on the plane of polish, invisible in bright field, into visible detail.

In many circumstances, the ability to capture, display, and preserve specimen images is very important. For that purpose, optical microscopes have increasingly built-in digital cameras transmitting high resolution images viewed within the microscope onto a TV or monitor. Adapted software allows performing image analysis. For details about optical microscopes, see George Vander Voort (ed) (2004), Geels K (2007).

17.3.2.2 Scanning Electron Microscopy

In a scanning electron microscope (SEM), an electron beam with an energy ranging from 0.5 to 40 keV is thermionically emitted from an electron gun. The electron beam is focused by one or two condenser lenses to a spot about 0.4–5 nm in diameter. The beam, generally in the final lens, passes through pairs of scanning coils or deflector plates, which deflect it in the x and y axes so that it scans over a rectangular area of the sample surface. The electron beam loses energy by repeated random scattering and absorption within the interaction volume of the specimen, which extends from less than 100 nm to around 5 μm into the surface. The size of the interaction volume depends on the electron's landing energy, the atomic number of the specimen, and the specimen's mass density. The analysis requires high vacuum conditions and specimens must be vacuum compatible (low vapor pressure) and electrically conductive. The charge-up effects on non-conductive samples can be compensated by reduced probe current, by reduced acceleration voltage or, in most cases, by coating them with a thin metal film (Au or Pt) or carbon layer.

Compared to OM, the depth of field of SEM is excellent, for example, at a magnification of 200 the DOF is 100 μm (against 0.7 μm for OM) and at a magnification of 10,000 the DOF is still 2 μm . This allows studying fractured coating surfaces, showing well the splat or grain microstructure. The fractured surface is cut to a suitable size, cleaned of any organic residues, and mounted on a specimen holder for viewing in the SEM. Actually, SEM can reach magnifications up to 500,000. As scanning electron microscopes have evolved, the electron beam cross-section has become smaller and smaller (they reach now a few nanometers in diameter) increasing magnification several fold. The last generation of

SEM, field emission scanning electron microscope (FESEM), has a beam cross-section close to 1 nm in diameter. The field emission tip is made up of a sharply etched piece of monocrystalline tungsten. A field applied to the tip causes electrons to tunnel out of the tip and accelerate down the column.

In SEM and FESEM, the electrons and photons generated in the excitation volume carry different types of information from the analyzed specimen: secondary electrons, backscattered electrons, absorbed specimen current, and cathodoluminescence. Secondary electrons are produced when the incident electrons from the beam interact with the atoms in the surface region of specimen. The impact (collision cascade) causes a path change for the incident electron and ionization of several specimen atoms. The ejected electrons leave the atom with a very small kinetic energy (< 50 eV) and permit a high resolution (about 3.5 nm) of fine surface morphology. As these electrons are sensitive to the orientation of different surface features, they create an image contrast for evaluating the sample's surface topography. SEM is routinely used to observe:

- Single splats
- Surface of as-sprayed coatings
- Metallographic polished surface of coatings or that of their cross-section to see layered splats, structure (columnar or granular), pores, voids from pullouts, and cracks
- Fractured surface of as-sprayed coatings
- Back scattered electrons (BSE) are high-energy electrons produced by the elastic collision of the incident electron beam with the electron cone of the sample atoms. Imaging with them provides elemental composition variation and surface topography (resolution about 5.5 nm). The yield is proportional to the atomic number (Z contrast) and depends on the beam energy and incidence angle. They also allow mapping of individual elements

An example of SEM images from Ingo GM et al. (2005) is presented in Fig. 17.4 for reactive plasma-sprayed composite

Ti–TiN–Ti_xNy coating starting from SP700 powder (Ti–4.5Al–3 V–2Mo–2Fe). Figure 17.4a shows the coating surface with high roughness as well as melted and unmolten particles, while Fig. 17.4b presents the coating cross-section by back scattered electrons (BSE) allowing distinguishing nitrated and non-nitrated particles.

The electron beam specimen interaction results in the emission of characteristic X-rays, which can be detected and analyzed (electron probe microanalysis, EPMA). For details about scanning electron microscopes, see [George Vander Voort (ed) (2004), Geels K (2007)].

17.3.2.3 Image Analysis

Image analysis is extensively used to assess the area percentages of some attributes such as porosity; see the chapter of [Riggs W (2004)] and the book of [Russ JC (2011)] or to filter images of spray jets, for example, to follow liquid drops injection in a DC plasma jet [Etchart-Salas R, et al. (2007)]. When a digital image is formed, the digitization process divides it into a horizontal grid of very small regions called “picture elements” or “pixels.” In the computer, this digital grid or “bitmap” represents the image. Each pixel is identified by its position in the grid, as referenced by its row (x) and column (y) number. Each pixel has a different color or gray scale value and together they form a representation of the image. Depending on whether pixels are black and white, gray scale, or color, pixels have different bit depths. Bit depth refers to the amount of information allocated to each pixel. For example, in digital color, each color occupies 8 bits (1 byte) while in a gray scale image each picture element has an assigned intensity ranging from 0 to 255. In image analysis, resolution refers to the number of pixels used to represent the image: more pixels correspond to a higher resolving power. With computers, information from image analysis can be easily modified and/or improved:

- Gray scale adjustment to improve the contrast

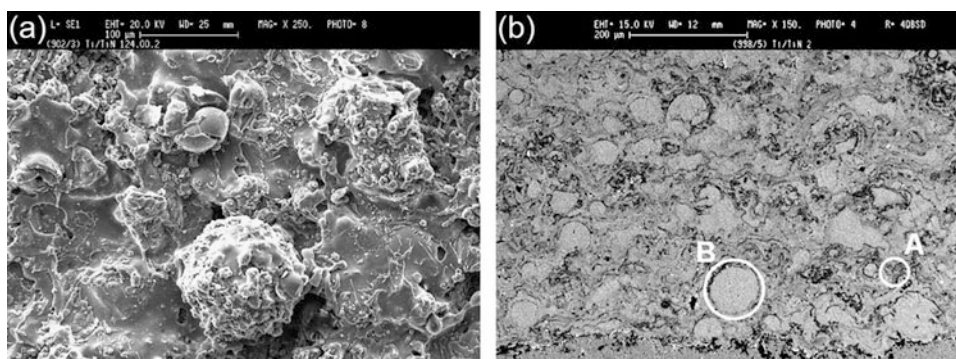


Fig. 17.4 Reactive plasma-sprayed composite Ti–TiN–Ti_xNy: (a) SEM image of the surface. (b) Cross-section of the coating in BSE micrograph (A) nitrated particles and (B) non-nitrated particles [Ingo GM et al. (2005)]. (Reprinted with kind permission from Elsevier)

- Spatial filtering, which generally results in an image with only edges of high contrast visible, fine detail with low contrast being usually lost to the background
- Noise reduction
- Edge enhancement
- Shape measurement
- Thresholding to select features of interest which is controversial since it is strongly operator dependent

For more details, see the paper of [Antou G and G Montavon (2007)] presenting, from a practical viewpoint, some key points to assess when implementing image analysis coupled to stereological protocols to quantify statistically the architecture of thermal spray coatings and their relevant features (pores, lamellae, and so forth).

Image analysis must be used with care and requires a good knowledge of how information is extracted from the image to achieve reliable data, for example, porosity. At last one must keep in mind that image analysis cannot give more precision than that given by the microscope observation of the prepared sample.

17.3.2.4 Atomic Force Microscopy

Atomic force microscopy (AFM) is based on the specimen surface scan by a cantilever with a sharp tip (probe) at its end. The cantilever is typically made of silicon or silicon nitride with a tip radius of curvature on the order of nanometers. When the tip is brought into proximity of a sample surface, forces between the tip and the sample lead to a deflection of the cantilever according to Hooke's law. Forces implied in AFM include mechanical contact force, van der Waals forces, capillary forces, chemical bonding, electrostatic forces, and magnetic forces. The cantilever deflection is generally measured using a laser spot reflected from its top surface onto an array of photodiodes.

A feedback mechanism makes it possible to adjust the tip-to-sample distance to maintain a constant force between the tip and the sample. For that the sample is moved in the z direction by a piezoelectric tube and in the x and y directions for scanning the sample. See [Eaton P, West P (2010)] for details about the different AFM modes: topographic, nontopographic, and surface modification.

Compared to SEM, AFM has several advantages: it provides a 3-D surface profile against a 2-D one for SEM, it works perfectly well in ambient air or liquid environment, and it can provide higher resolution than SEM. However, it also has some disadvantages: in one pass, SEM can image an area in the order of square millimeters with a depth of field in the order of millimeters, while AFM can only image a maximum height in the order of 10–20 μm and a maximum scanning area of about $150 \times 150 \mu\text{m}$. The scanning speed

of AFM is slower than that of SEM that is capable of scanning at near real time, although at relatively low quality.

In thermal spraying, AFM has been used especially to study splat formation and characterize the variation with oxidation of smooth substrate surface topography at the nanometer scale.

17.3.2.5 Transmission Electron Microscopy

Transmission electron microscopy (TEM) works on the same principle as an old-fashioned slide projector, except that an electron beam replaces light. In the projector, the light passing through the film interacts with it. The light going through the film hits the lenses disposed on the other side and the resulting image is projected onto a screen. In a TEM, a beam of electrons is focused on a single, pinpoint spot or element on the sample being studied [Williams DB, Carter CB (2009)]. The electrons interact with the sample and only those that go through unobstructed hit the phosphors screen on the other side. Electrons that hit the screen are converted to light and so an image is formed. The dark areas of the image correspond to areas on the specimen where fewer electrons were able to pass through (either absorbed or scattered upon impact); the lighter areas are where more electrons pass through, although the varying amounts of electrons in these areas enable the user to see structures and gradients. In a TEM, lenses made of electromagnetic devices focus the electron beam to the desired wavelength or size. The amount of power used to generate electrons controls magnification that can be very high, permitting to see objects a few angstroms in size. Of course, TEM works under high vacuum that can be very low (10^{-7} to 10^{-9} Pa) in certain parts. High-resolution TEM (HR-TEM) is the ultimate tool in imaging defects. In favorable cases, it shows directly a 2-D projection of the crystal with defects and its magnification can reach 10^6 .

The drawback of TEM is that specimens studied have to be sliced very thinly (a few micrometers) to ensure that they are electron transparent; they must also be placed in a vacuum. Thus, preparation of specimens is often time consuming. Moreover, it requires expert handling to limit the risk of inadvertent damage during the process, especially for ceramic materials. For example, a wedge-polishing technique was used to prepare samples of YSZ single splats [Chraska T, King AH (2001)]. Wedge-polishing device, supplied by different manufacturers, reduces the need for ion milling by mechanically thinning the area of interest to 0.1 μm or less. These polishing kits are recommended for material applications involving microelectronics, metals, ceramics, minerals, and composites. Electron transparency thickness can be reached for TEM analysis. Focus ion beam (FIB) systems, described earlier in Sect. 17.3.1.6, operate in a fashion similar to a scanning electron microscope (SEM) are also used for TEM sample preparation.

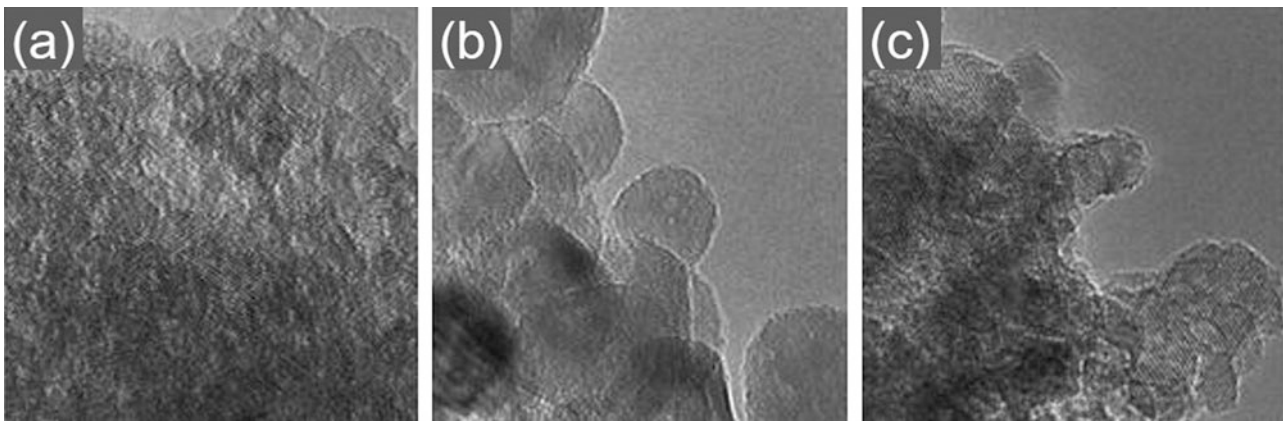


Fig. 17.5 TEM images of (a) as-synthesized, (b) annealed, and (c) hydrothermal treated TiO_2 powders [Tjitra Salim N et al. (2011)]. (Reprinted with kind permission from Elsevier)

TEM allows obtaining information about morphology, crystal size, and chemistry, if equipped as SEM with an EDS (energy-dispersive X-ray spectroscopy) probe. Two observation modes are used: image mode to observe the specimen morphology with a very high magnification and diffraction mode giving information about the crystalline structure. For example, TEM was used by Tjitra Salim N et al. (2011) to characterize TiO_2 powders synthesized by hydrolysis of titanyl sulfate (TiOSO_4) in distilled water with a small addition of inorganic salt. At a relatively low hydrolysis temperature, pure anatase TiO_2 could be obtained and post-synthesis treatments (annealing or hydrothermal treatment) did not alter this phase structure. The powder was then agglomerated with fine nano-primary particles, with different post-synthesis treatments leading to different TiO_2 nanostructures. Figure 17.5a represents the powder as synthesized, while Fig. 17.5b shows the annealed powder, and Fig. 17.5c shows the hydrothermal treated powder with its unique oriented agglomeration structures. The hydrothermal treatment consisted in soaking the TiO_2 powder in distilled water and heat treating it for 5 h in an autoclave at 150 °C.

Among the numerous papers about thermal-sprayed coatings where TEM was used to characterize either powders or coatings or both, Chen H et al. (2010) characterized nanostructured zirconia particles, Yan D et al. (2011) studied the structure of coating prepared by reactive plasma spraying $\text{Fe}_2\text{O}_3/\text{Al}$ composite powders, Ma XQ et al. (2008) observed grain structures of suspensions of Ni–14.55Cr–3.22B–4.7Si–4.78Fe sprayed by HVOF, and Chraska T (1999) studied microstructures and interfaces of zirconia coatings produced by plasma spraying. For more details, see [Williams DB, ASM International (2008)].

17.4 Materials Characterization

The techniques described below are limited to nondestructive analytical techniques, which reveal information about the crystallographic structure, chemical composition, and physical properties of coatings. These are based on the observation of the scattered intensity of X-rays, infrared, neutron, and nuclear gamma ray beams hitting a specimen as to incident and scattered angles, polarization, and wavelength or energy.

17.4.1 X-Ray Fluorescence

When a primary X-ray excitation source strikes a sample, the X-rays can be either absorbed by the atom or scattered through the material. The photoelectric effect occurs when the atom absorbs X-ray, the energy of which is all transferred to an innermost electron. If the primary X-rays have sufficient energy, electrons are ejected from the inner shells, creating vacancies. As the atoms return to stable condition, electrons from the outer shells are transferred to the inner shells. This process creates characteristic X-rays whose energy is the difference between the two binding energies of the corresponding shells. Each element having a unique set of energy levels produces X-rays at a unique set of energies. The theoretical relationship between the measured X-ray intensities and concentrations of elements in the sample allows the nondestructive measure of the elemental composition of a sample. This process is called “X-ray Fluorescence” or XRF. A typical X-ray spectrum from an irradiated sample displays multiple peaks of different intensities. The penetration depth of X-ray depends on the coating material and the wavelength of the beam, but it is generally a few micrometers

at the maximum 10–15 μm . For details, see ASM International (2008).

17.4.2 Infrared Spectroscopy

In infrared spectroscopy (IRS) molecules absorb specific frequencies that are characteristic of their chemical bonds and organization. The frequency of the absorbed radiation matches the frequency of the bond or group that vibrates. The shape of the molecular potential energy surfaces, masses of atoms, and the associated vibration coupling determine the energies. The frequency of the vibrations can be associated with a particular bond type. For example, the characteristic wave numbers of oxides are between 250 and 1000 cm^{-1} .

Fourier transform infrared spectroscopy (FTIR) refers to a recent development in which infrared light is guided through an interferometer and then through the sample (or vice versa). The data are collected and converted from an interference pattern to a spectrum. The sample's spectrum is then compared to standards as described in ASM International (2008) and 17.Ma1.

In thermal spraying, FTIR has been used to characterize the oxide layer formed at the smooth surface of a metal or alloy substrate subjected to the preheating conditions prior to spraying [Chandra S, Fauchais P (2009)]. In this case, the analysis was performed with a quasi-raking incidence of the IR light and its depth was between a few nanometers and few micrometers.

17.4.3 Mössbauer Spectroscopy

Mössbauer spectroscopy (MS) is a spectroscopic technique based on the recoil-free, resonant absorption, and emission of gamma rays in solids. Typically, three types of nuclear interaction may be observed: an isomer shift, also known as a chemical shift; quadrupole splitting; and magnetic or hyperfine splitting, also known as the Zeeman effect (splitting of a spectral line into several components in the presence of a static magnetic field) [Volenk K, et al. (1999)].

Mössbauer spectroscopy gives local information on the nucleus affected, its vibration state, electron density, and magnetic momentum. These data inform about the valence state of the corresponding atoms, bonds with their neighbors, and positions within the crystalline network. The technique is well adapted to the study of iron and its oxides as it allows characterizing phases and their relative percentages. It has been used to characterize the oxidation of steel substrates according to the preheating conditions [Chandra S, Fauchais P (2009)]. It has also been used to characterize the in-flight oxidation of plasma-sprayed alloy steel particles [Volenk K, et al. (1999)].

17.4.4 X-Ray Diffraction

X-ray diffraction (XRD) is a versatile, nondestructive technique that reveals detailed information about the chemical composition and crystallographic structure of natural and synthetic materials, including coatings [ASM International (2008) and 17.Ma2–17.Ma5]. When a monochromatic X-ray beam is projected onto a crystalline material at an angle, θ , diffraction occurs only when the distance traveled by the rays reflected from successive crystal planes differs by an integer number, n of wavelengths. Bragg developed in 1913 the following relationship between the order of reflection, n , of the crystallographic planes and the angles of incidence (θ) of the X-ray beam.

$$n\lambda = 2d_{hkl} \sin \theta \quad (17.4)$$

Where, d , is the distance between atomic layers with the same Miller indices (h , k , l), in a crystal, and λ , is the wavelength of the incident X-ray beam. By varying the angle theta, the Bragg's law conditions are satisfied by different d -spacings (characterized by Miller indices) in polycrystalline materials. Plotting the angular positions and intensities of the resultant diffracted peaks of radiation produces a pattern, which is characteristic of the sample. When the sample is a mixture of different phases, the resultant diffractogram is formed by addition of the individual patterns. The identification of crystalline materials is based on the comparison of experimental values of the reticular distances with reference data banks compiled by the Joint Committee Powder Diffraction Standard (JCPDS). XRD is extensively used in thermal spraying, for example, to characterize structural changes between the sprayed powder and coating. It must be underlined that the penetration distance of the X-ray beam into the sample can vary from few to several micrometers depending on the sample characteristics and wavelength of the beam.

XRD is also used to estimate the average grain size of the feedstock and coating. The applicability of this method was confirmed by comparing results from TEM and XRD techniques [Chraska T (1999), Lima RS et al. (2001a, b)]. The XRD method assumes that the overall broadening of XRD peaks comprises two effects: one arising from the small coherent grain size and one arising from the atomic level micro-strain, that is, $(\Delta d/d)$, where d is the atomic spacing. The peak width resulting from a small grain size effect alone can be described by the Scherrer equation [ASM International (2008)]:

$$B(2\theta) = \frac{K\lambda}{D \cos \theta} \quad (17.5)$$

where $B(2\theta)$ is the true broadening of the diffraction line measured at full width at half-maximum (FWHM), λ is the wavelength of the X-ray radiation, D is the mean dimension of the grains, θ is the Bragg's angle, and K is the Scherrer constant with a commonly used value of 0.9, depending on how the width is determined, the shape of the crystal, and the size distribution. For more information about the K constant, see [Langford JI and AJC Wilson (1978)].

Hugo Rietveld, for the characterization of crystalline materials, showed that the neutron and X-ray diffractions of powder samples result in a pattern characterized by reflections (peaks in intensity) at certain positions. The height, width, and position of these reflections can be used to determine many aspects of the materials structure (see [ASM International (2008)]). X-ray diffraction also makes it possible to measure the angular lattice strain distributions resulting from residual stress. A reflection at high 2θ is chosen and the change in the d -spacing with different orientations of the sample is measured. Using Hooke's law, relating stress and strain, the stress can be calculated from the strain distribution.

In amorphous material, the atoms are not arranged in a periodic fashion such that observed with crystals and the scattering intensity is then the summation of each individual atom. Thus, weak X-ray scattering, scattering spreading throughout reciprocal space, and a detailed analysis are required to obtain real-space information characterizing amorphous coatings. Spectra with amorphous elements are characterized by a broad halo as illustrated in Fig. 17.6 after Liu XQ et al. (2009) who sprayed an FeCrMoMnWBCSi amorphous metallic coating with thickness of about 1 mm,

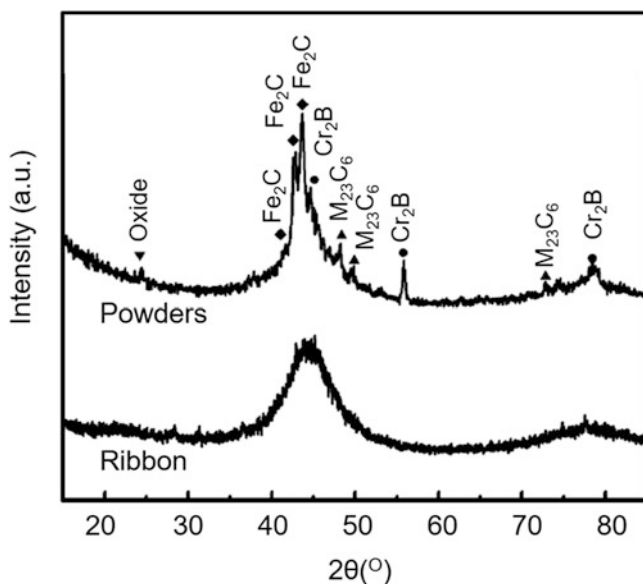


Fig. 17.6 XRD patterns of the as-spun ribbon and the atomized powders of Fe-based alloy [Liu XQ et al. (2009)]. (Reprinted with kind permission from Elsevier)

and porosity less than 0.1%, onto mild steel, using high-velocity plasma gun with axial powder injection. Comparing the XRD pattern of the powder used to that of an as-spun ribbon obtained by melt spinning, Fig. 17.6 reveals a broad halo of fully amorphous phase in the ribbon samples. For the powder, it shows a similar broad halo with some crystalline peaks superposed due to Fe_2C , Cr_2B , and M_{23}C_6 , reflecting that the cooling rate of gas atomization is apparently lower than that of melt spinning. These XRD patterns were also compared to those of coatings obtained with different spray conditions. Similar XRD patterns can be found in many references such as, for example, Kishitake K, Era H, Otsubo F (1996), Zhao XB, Ye ZH (2012).

17.4.5 Small-Angle X-Ray Scattering

Small-angle X-ray scattering (SAXS) is used for the structural characterization of solid and liquid materials in the nanometer (nm) range. It probes inhomogeneities of the electron density on a length scale of typically 1–100 nm, thus yielding complementary structural information to standard XRD data. SAXS is applicable to crystalline and amorphous materials alike. Measurements are commonly performed in transmission geometry, using a narrow, well-collimated, and intense X-ray beam. Scattering angles typically range between 0.1° and 5° . The smallest accessible angle determines the largest resolvable feature size. Some typical applications comprise the determination of nanometer-sized particle and pore size distributions of specific surface areas. For more details, see the book of [Guinier A and G Fournet (1955)].

For coatings, ultra-small-angle X-ray scattering (USAXS) is used as a nondestructive characterization technique recording elastic scattering of X-rays induced by compositional and structural inhomogeneities [Ilavsky J, et al. (2009a, b)]. USAXS has been successfully implemented in quantifying void size distribution in YPSZ-EB-PVD coatings [Flores A, et al. (2007)] and also in YPSZ ($d_{50} = 50$ nm) suspension plasma-sprayed coatings [Bacciocchi A, et al. (2010a, b)]. For the EB-PVD coatings, computer modeling was used to obtain values of stereometric (geometrical and spatial) characteristics of the pore populations in terms of their volume fraction, shape (aspect ratio), size, and orientation, each representing statistical average values based on Gaussian distributions. For the nanometer-sized structured coating, about 80% of voids, in number, exhibited characteristic dimensions smaller than 30 nm, the largest voids in the coatings having characteristic dimensions of a few hundreds of nanometers. Such results are difficult, if not impossible, to obtain from other characterization techniques, since it detects with a very high resolution to the whole set of scatters (voids

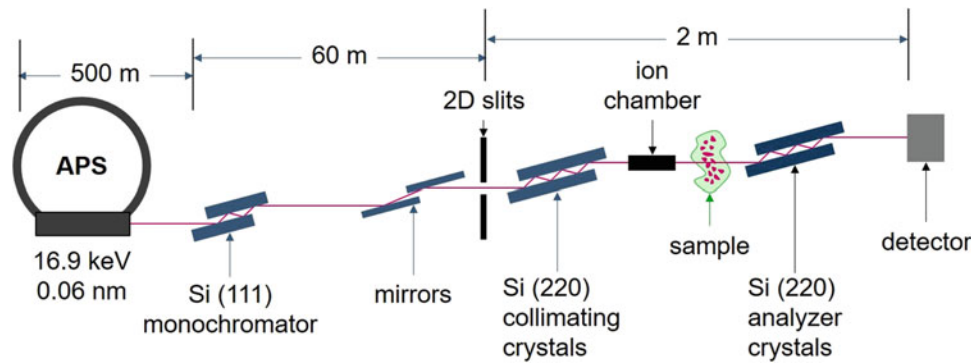


Fig. 17.7 Scheme of the advanced photon source (Argonne National Laboratory, Argonne, IL, USA) (<http://usaxs.xor.aps.anl.gov/>, see also [Ilavsky J, et al. (2009a, b)])

in this case) regardless of their characteristics (open, connected, or closed).

For both examples cited above, USAXS experiments were conducted on beam line 32-IDat Advanced Photon Source (Argonne National Laboratory, Argonne, IL, USA). Measurements were performed in transmission geometry as shown in Fig. 17.7 that shows the characteristic dimensions of this source. The interested reader can find further details on the Web site of Argonne National Laboratory (<http://usaxs.xor.aps.anl.gov/>, see also [Ilavsky J, et al. (2009a, b)]).

The USAXS instrument uses Bonse–Hart crystal diffraction optics, which allows recording of small-angle scattering curves using a photodiode detector. q is the scattering vector, ranges from 10^{-4} to 1 \AA^{-1} with an angular resolution of 10^{-4} \AA^{-1} . The scattering vector $|q|$ [Kishitake K, Era H, Otsubo F (1996)] is a typically used quantity in small-angle scattering and relates to the diffraction angle (2θ), as known from X-ray diffraction, via the relationship:

$$|q| = \frac{4\pi \sin \theta}{\lambda} \quad (17.6)$$

where λ is the X-ray wavelength. Combining this equation with Bragg's law, the length scale, L , probed at a given q range follows the general inverse relationship:

$$L \approx \frac{2\pi}{|q|} \quad (17.7)$$

This setup delivers approximately 10^{13} photons per second in about 1 mm^2 area at the sample position, for incident photons with energy around 16.9 keV and corresponding to a wavelength of 0.775 \AA . The uncertainty estimation for USAXS results is challenging, and absolute intensity of USAXS calibration was estimated, from repeated measurements, to present an uncertainty of about $\pm 5\%$ for the total volume content [Bacciochini A, et al. (2010a, b)].

17.4.6 Small Angle Neutron Scattering

Small angle neutron scattering (SANS) is a laboratory technique, similar to the complementary techniques of small angle X-ray scattering (SAXS) and light scattering. The technique provides valuable information over a wide variety of scientific and technological applications, especially for coatings defects in materials, the data analysis giving information on size and shape. [Allen AJ, et al. (2001a, b), Ilavsky J, et al. (1994) (1999a, b), Kulkarni A, et al. (2003) (2005)].

With SANS experiment a beam of neutrons is directed at a sample, which can be for coatings, a solid or a powder. The neutrons are elastically scattered by changes of refractive index on a nanometer scale inside the sample, which is the interaction with the nuclei of the atoms present in the sample. In this experiment, a monochromatic beam of thermalized neutrons passes through the specimen in transmission geometry and the scattered neutrons are recorded on a 2-D detector. Figure 17.8a shows the principle of the SANS instrument [Kulkarni A, et al. (2003)]. Neutrons are capable of interacting strongly with all atoms, in contrast to X-ray techniques where the X-rays interact weakly with hydrogen, the most abundant element. Small angle neutron scattering is caused by fluctuations of scattering length density $\rho(r)$ on a size scale 1 nm to 5 \mu m in the studied material. These fluctuations are connected with compositional and/or structural inhomogeneity such as pores. The fluctuations of scattering length density result in the scattering contrast $\Delta\rho(r) = \rho(r) - \bar{\rho}$, where r is the coordinate in the real space and $\bar{\rho}$ the average scattering length density of the sample. The scattering contrast gives rise to the coherent elastic scattering of neutrons to small magnitudes of the scattering vector $|q|$; see Eq. 17.6, ($q = k - k_0$, where k is the wave vectors of the incident and scattered neutron, respectively, $|k| = |k_0| = 2\pi/\lambda$, λ being the incident neutron wavelength).

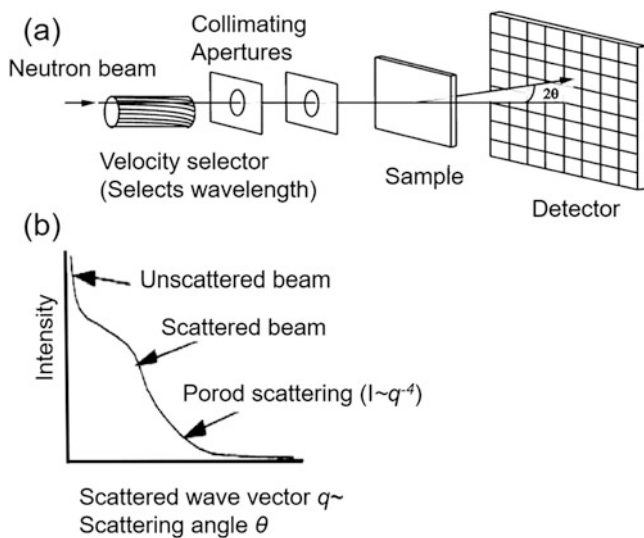


Fig. 17.8 (a) Scheme of the SANS instrument. (b) Evolution of signal intensity with scattered wave vector q [Kulkarni A, et al. (2003)]. (Reprinted with kind permission from Elsevier)

In this experiment [Kulkarni A, et al. (2003)], a monochromatic beam of thermalized neutrons passes through the specimen in transmission geometry and the scattered neutrons are recorded on a 2-D detector, as shown in Fig. 17.8a. Scattering occurs at the void–grain interface due to differences in scattering length density between the material and the pores. The first measurement is the anisotropic Porod scattering (see Fig. 17.8b), where the orientation averaging of the Porod scattering from the sample gives the total void surface area per unit sample volume, independent of the precise void morphology [Kulkarni A, et al. (2003)]. The second type of measurement is anisotropic multiple SANS (MSANS), involving the measurement of the beam broadening due to anisotropic multiple scattering by long wavelength neutrons. In Porod scattering, the scattering intensity, $I(q)$, is a function of the magnitude and direction of the scattering vector, q , and its orientation average, as shown in Fig. 17.8b. More complete microstructural information is obtained by combining MSANS measurements for different sample orientations, anisotropic Porod surface area distributions, and the total porosity determined from precision density measurements [Kulkarni A, et al. (2003)]. The MSANS beam broadening shows much greater sensitivity to the coarse globular and irregular porosity than does the Porod scattering analysis. For interpretation of the anisotropic MSANS beam-broadening data, the interlamellar pores and intra-splat cracks are considered to comprise two space-filling networks of oblate spheroids, each with a fixed aspect ratio, and the globular pores are considered spheres.

Allen et al. (2001a, b) were among the first to use SANS to determine the porosity of ceramic plasma-sprayed coatings. The voids and the grains within the samples have different

scattering length density, ρ , causing some of the neutrons to be scattered at the void/grain interfaces. In the SANS experiment, a beam of “cold” neutrons with wavelength λ , ranging from 5 to 18 Å and controlled by a neutron velocity selector, is passed through parallel-sided sample. Scattered neutrons are recorded in directions orthogonal and parallel to the coating with a 2-D area detector. The intensity of the scattering vector varies with the volume fraction of porosities, the scattering contrast $(\Delta\rho)^2$ (square of the difference in scattering length densities between the grains and the void), and on the distribution of void sizes [Ilavsky J et al. (1999a, b)]. The scattering curve of intensity versus scattering angle can be divided into two regions as shown in Fig. 17.8b. The multiple small angle neutron scattering (MSANS) region is dominated by neutrons scattered many times by large pores inside the sample. The theory of MSANS is useful for pores with sizes in the 0.08–10 μm range. Larger scattering angles are dominated by scattering from the surfaces of pores in a region, which is termed the Porod region [Ilavsky J, et al. (1999a, b)]. The anisotropy in the Porod scattering is strongly amplified by the shape of the scattering material. The anisotropy depends not only on the individual pore shapes and preferred orientation but also on the polydispersity of pore shapes and sizes and to some extent on the surface roughness [Kulkarni A, et al. (2003)].

SANS has the major advantages of not requiring sample preparation and its ability to provide quantitative information concerning the separate crack and pore systems, including their distinctive anisotropies [Ilavsky J, et al. (1999a, b)]. However, the relationship between the SANS results and the underlying structure is more complex and less intuitive than for image analysis. The availability of the SANS technique is limited by the need to have access to a powerful neutron source. Kulkarni et al. (2003) described the quantitative characterization of the microstructure of plasma-sprayed partially stabilized zirconia (PSZ) coatings by means of X-ray and neutron-scattering imaging techniques. Petorak et al. (2010) have used SEM and Porod’s specific surface area analysis of SANS results to determine which void systems, either interlamellar pores or intra-lamellar cracks, contributed to the observed relaxation of stress in plasma-sprayed coatings when simulating TBC service conditions. [Allen et al. (2001a, b) explored the relationships between the feedstock or spray process conditions, anisotropic void and crack microstructures of the deposits, and technologically important deposit properties such as thermal conductivity. Kulkarni et al. (2003) described the quantitative characterization of the microstructure of plasma-sprayed partially stabilized zirconia (PSZ) coatings by means of X-ray and neutron-scattering imaging techniques.

17.4.7 X-Ray Absorption Spectroscopy

X-ray absorption spectroscopy (XAS) is widely used for determining the local geometric and/or electronic structure of matter. Usually, it is performed using synchrotron radiation sources providing intense and tunable X-ray beams. The photon energy is tuned using a crystalline monochromator to a range where core atom electrons can be excited (0.1–100 keV photon energy) with the principal quantum numbers $n = 1, 2,$ and 3 corresponding to the K-, L-, and M-shells, respectively. For instance, excitation of a $1s$ electron occurs at the K-edge, while excitation of a $2p$ electron occurs at an L-edge. When a monochromatic X-ray beam is directed through a sample and the energy of the X-ray is gradually increased such that the X-ray beam crosses an absorption edge of one of the elements of interest in the sample, the transmitted X-ray light will contain small variations in absorbance, on the high energy side of the absorption edge. These absorbance variations provide information about the structural environment of the atoms surrounding the element whose absorption edge is being examined. An X-ray absorption spectrum is generally divided into four sections:

- Pre-edge ($E < E_0$);
- X-ray absorption near edge structure (XANES), where the energy of the incident X-ray beam is $E = E_0 \pm 10$ eV;
- Near edge X-ray absorption fine structure (NEXAFS), in the region between 10 and 50 eV above the edge; and
- Extended X-ray absorption fine structure (EXAFS), which starts approximately from 50 eV and continues up to 1000 eV above the edge.

One of the main interests of XAS is its tunability allowing probing the environments (molecular structure) of different elements in the sample by selecting the incident X-ray energy. For details, see the book of Bunker G. (2010).

17.4.8 Electron Probe X-Ray Microanalysis

Electron probe microanalysis (EPMA) associated with SEM is generally considered as microanalytical technique able to image or analyze materials. Elemental analysis is accomplished at a microscale (about a few μm^2). It makes it possible to identify the elements present and quantify them, down to about 100 ppm with a rather good accuracy. Elements lighter than atomic number 8 cannot be measured without reservations.

EPMA implies that the element densities in the probed volume are uniformly distributed. Thus, to obtain information on a large area, the over-scanning must be avoided, and the large area sampled at many discrete points. For details, see [George Vander Voort (ed) (2004) and 17.Ma6].

17.4.9 Auger Electron Spectroscopy

Auger electron spectroscopy (AES) is used specifically in the study of surfaces. The Auger effect is based on the analysis of energetic electrons emitted from an excited atom after a series of internal relaxation events. Auger effect is produced whenever incident radiation—photons, electrons, and ions—interacts with an atom with an energy exceeding that to remove an inner-shell electron (L, M, ...) from the atom. This interaction leaves the atom in an excited state with a core hole, that is, a missing inner-shell electron. These excited atoms have a limited life and de-excitation occurs very rapidly with the emission of an X-ray or an electron termed Auger electron. SEMs are equipped to detect such electrons and AES is now a practical and straightforward characterization technique for probing chemical and compositional surface environments [George Vander Voort (ed) (2004) and 17.Ma7].

17.4.10 X-Ray Photoelectron Spectroscopy

X-ray photoelectron spectroscopy (XPS), also known as electron spectroscopy for chemical analysis (ESCA), is a quantitative spectroscopic technique that measures the elemental composition, chemical state, and electronic state of the elements that exist within a material. The material is irradiated with a beam of X-rays and the kinetic energy and numbers of electrons that escape from the top (1–10 nm) are measured. XPS works exclusively in ultrahigh vacuum; it allows analyzing the surface chemistry of a material in its “as-received” state or after some treatment. XPS detects all elements with atomic number (Z) of 3 (lithium) and above. Detection limits for most of the elements are in the parts per thousand ranges. For details, see [George Vander Voort (ed) (2004) and 17.Ma8–17.Ma10].

17.4.11 Other Techniques

The characterization means described above are those mostly used for thermal-sprayed coatings. Complementary techniques such as inductively coupled plasma atomic emission spectroscopy (ICP-AES) or inductively coupled plasma mass spectrometry (ICP-MS) can be used for elemental analysis in the, part per million (ppm) or lower concentration range. Atomic absorption spectrometry (AAS) can be used for measuring relatively low concentrations of metallic or semi-metallic elements in a solution of the sample containing the metals, for details, see [ASM International (2008)].

model is wrong for the majority of engineered materials. For more complicated pore microstructures, one can imagine pores that are better approximated by other geometrical shapes, such as ellipsoids or platelets [Ilavsky J (2010)].

Several methods are commonly implemented to quantify voids network in a porous medium at the micrometer scale. Reviews on the subject have been presented by Ilavsky J. (2010), Andreola F et al. (2000) and Fauchais P et al. (2011). A listing of conventional techniques used to qualify voids in thermal spray coatings is given in Table 17.1 after Fauchais P et al. (2011) identifying the void characteristics and basic concepts used. In the following, a brief description is presented of some of these techniques highlighting their main characteristics, potential and limitations when applied to nanometer-sized pores in thermal spray coatings.

17.5.1 Archimedean Porosimetry

Archimedean porosimetry (AP) makes it possible to quantify the nonconnected “closed” porosity [Andreola F et al. (2000), Mancini CE, et al. (2001), Matějček J et al. (2006)]. The substrate is generally removed by chemical etching in acid medium, followed by the weighing of a “freestanding” sample of the coating in ambient air and with the sample immersion into de-mineralized water. Knowing the specific mass of water w_{water} (i.e., depending upon temperature), the volume of the coating sample used is calculated, according to Archimedean, by measuring:

- The dry weight of the sample, w_{dry} .
- The weight of the sample, w_{sat} after complete impregnation of open porosities.
- The weight of water-saturated sample while it is immersed in water, w_{wet} .

The weight of water displaced, w_{wd} , can be calculated as;

$$w_{\text{wd}} = w_{\text{sat}} - w_{\text{wet}} \quad (17.8)$$

Knowing the water temperature and accordingly its specific mass, ρ_w the bulk volume of the sample, V_b is given by;

$$V_b = w_{\text{wd}}/\rho_w \quad (17.9)$$

The open pores volume, V_p is obtained by calculating the weight of water they contain, w_{wp} dividing it by the specific mass of water ρ_w

$$w_{\text{wp}} = w_{\text{sat}} - w_{\text{dry}} \quad (17.10)$$

$$V_p = w_{\text{wp}}/\rho_w \quad (17.11)$$

the apparent porosity, ϕ_a is given by

$$\phi_a = V_p/V_g \quad (17.12)$$

A value for porosity can alternatively be calculated from the bulk mass density ρ_{bulk} and particle mass density ρ_{part} :

$$\phi_a = 1 - \rho_{\text{bulk}}/\rho_{\text{part}} \quad (17.13)$$

Closed or sealed pores are not included in the apparent porosity value. The latter is usually close to the total porosity as long as the closed porosity in the sample is low. The first limitation of Eq. 17.13 is that the coating bulk-specific mass must be known. It depends on the coating phase content that can be analyzed by X-ray diffraction analysis. Equation 17.12 on the other hand is limited by the size of the accessible of pores. Percolation test of deionized water drops through the coating can be used to determine the smallest open pore diameter into which the water can penetrate. This is governed by the contact angle, θ , which is for zirconia and deionized water about 59° and the surface energy, γ , of deionized water 72.8 mN/m at room temperature. At atmospheric pressure (about 10^5 Pa), pure water percolates, according to Lucas–Washburn’s equation [Washburn EW (1921)], into open voids of equivalent diameter equal or larger than 1.5 μm , while most of open voids in nanometer-sized coatings exhibit characteristic dimensions smaller than micrometer.

17.5.2 Mercury Intrusion Porosimetry

Mercury intrusion porosimetry (MIP) is based on the concept that nonwetting mercury percolates through the open voids according to the applied impregnation pressure. This results in the intrusion versus pressure curve, which can be normalized with respect to sample weight or volume [Ilavsky J, et al. (1997), Van Brakel J, et al (1981), Siebert B, et al. (1999), Mauer G, et al. (2009)]. The experimental data are analyzed on the basis of the Washburn equation:

$$d = \frac{-4\gamma \cos \theta}{p} \quad (17.14)$$

where d represents the equivalent pore diameter (m), γ is the surface tension of mercury (N/m), θ is the contact angle between the pore walls and mercury, and p is the applied pressure (Pa). The result is converted into equivalent pore sizes on the assumption of tubular pores. Often the mercury

porosimetry consists of two parts: the low pressure part (0.1–400 kPa) for the measurement of large pores up to a maximum dimension of 60–100 μm , depending on how much mercury is used, and the high pressure part (0.1 ± 400 MPa) detecting pores and micro-cracks down to the size of 1.8 nm.

However, while MIP techniques cover a large void size range, they are limited to the measurement of accessible open-void networks that combined with the necessity to apply high pressure of mercury can lead to sample deformation and even structural failures [Zhu S, et al. (1995)] and the distortion of the volume distribution versus pore characteristic dimension relationship.

17.5.3 Gas Permeation and Pycnometry

Gas permeation (GP) is determined by measuring the pressure drop across the sample of the coating of known thickness, as function of the gas (air) flow rate. This is usually achieved by applying a gas pressure to one face of the sample while the other face is kept at a reference pressure (usually atmospheric). After checking the linear evolution of the pressure drop versus the gas flow rate, the permeability can be determined from the Darcy's law [Wittmann-T  n  ze K et al. (2008)]:

$$Q = k \frac{A \cdot \Delta p}{\mu \cdot e} \quad (17.15)$$

The leakage rate is then calculated from the linear regression of the curve, $(Q/A)\mu$ versus $(\Delta p/e)$, Q is the imposed gas flow rate (m^3/s), A sample measured area (m^2), μ gas dynamic viscosity (Pa.s), e sample thickness (m), Δp , pressure drop (Pa), and k permeability of the material.

The ability of measuring the gas permeation of the coating at elevated temperatures (corresponding usually to coating operating temperature) and the possible use of different gases are the two major advantages of this technique [Li C-J, et al.

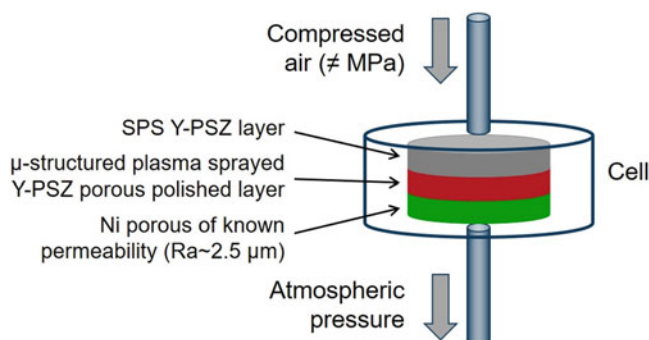


Fig. 17.9 Principle of the permeation measurement of an YSZ coating suspension plasma sprayed [Brousse E (2010)]. (Reprinted with kind permission from Dr. E. Brousse)

(2005), Fox AC, Clyne TW (2004), Golosnoy IO, et al. (2008), Reed JS (1995), Curran JA, Clyne TW (2006), Bacciochini A, et al. (2010a, b), Ilavsky J et al. (1999a, b)]. For thin nanostructured YSZ coatings resulting from thermal-sprayed suspension or liquid precursors, multiple-layered coatings as shown in Fig. 17.9 after [Brousse E (2010)] are used for gas permeation measurement. The under-layer, made of a material of known permeation rate, can influence the coating void architecture, which would have not been the case if the under-layer had been dense as a conventional substrate.

Helium pycnometry is used to determine the skeletal density of (non) porous solid and gives indirect information about pore volume and closed porosity. The simplest type of gas pycnometer (no moving parts) consists of two chambers: one (with a removable gas-tight lid) to hold the sample and a second chamber of fixed, calibrated internal volume, referred to as the reference volume or added volume. A valve allows admitting a gas under pressure to one of the chambers. The pressure in the first chamber is measured with a transducer, the two chambers can be connected, and the second chamber can be vented. The working equation of a gas pycnometer wherein the sample chamber is pressurized first is as follows:

$$V_s = V_c + \frac{V_r}{(1 - p_1/p_2)} \quad (17.16)$$

where V_s is the sample volume, V_c is the volume of the empty sample chamber (known from a prior calibration step), V_r is the volume of the reference volume (also known from a prior calibration step), p_1 is the first pressure (i.e., in the sample chamber only), and p_2 is the second (lower) pressure after expansion of the gas into the combined volumes of sample chamber and reference chamber.

While pycnometers of any type are recognized as density measuring devices, they are in fact devices for measuring volume only. The volume measured in a gas pycnometer is the amount of 3-D space, which is inaccessible to the gas used, that is, the volume within the sample chamber from which the gas is excluded. Therefore, the volume measured depends on the atomic or molecular size of the gas. Helium is most often the prescribed gas, because of the atom small size and also because it is inert. Indeed, gas atoms form a single layer on the total surface of material and penetrate into open and connected porosity. This technique has already been successfully employed to determine the mass density of plasma-sprayed coatings [Golosnoy IO, et al. (2008)]. By comparing with the theoretical mass density, this measurement gives the percentage of closed porosity of the sample. It has been used for nanometer-sized suspension plasma-sprayed coatings [Reed JS (1995)].

17.5.4 Small Angle Neutrons Scattering

A quantitative characterization of the microstructural features has been demonstrated successfully in the case of plasma-sprayed YPSZ coatings, using a combination of anisotropic Porod scattering (PS) and multiple small angle neutron scattering (MSANS) techniques. The experiment is the same as that described in Sect. 17.4.6. The scattering occurs at the void–grain interface due to differences in scattering length density between the material and pores. Two types of measurements are performed: anisotropic Porod scattering (PS) and anisotropic MSANS [Ilavsky J, et al. (1999b)]. The anisotropic Porod scattering can be divided into two anisotropic contributions: one from interlamellar pores that are predominantly parallel to the substrate and the other from intra-splat cracks that are predominantly perpendicular to the substrate. Orientation averaging of the Porod scattering from the sample makes it possible to obtain the total void surface area per unit sample volume.

Two examples of results are presented in Fig. 17.10 after Ilavsky et al. (1999a, b). Water-stabilized plasma-sprayed alumina SANS results, presented in Fig. 17.10a, show high anisotropy of the apparent Porod surface area distribution dominated by intralamellar cracks. Apparent Porod surface area can be defined as the Porod surface area, which would be viewed in any particular direction by an observer standing in

the center of the sample. Knowledge of this apparent surface area in all directions (over 4π) allows calculation of the specific surface area in the sample, and the identification of more surface systems can be distinguished.

Allen AJ et al. (2001a, b), and Kulkarni A. et al. (2003) used this method to study the effect of partially stabilized zirconia feedstock characteristics (particle density, size, and shape) on the anisotropic void structure of plasma-sprayed coatings. They correlated the results with the thermal conductivity and elastic modulus of coatings; properties that are most sensitive to these microstructural features. Ilavsky J. et al. (1999b) used SANS to study the effect of heating on the pores and cracks in YSZ coatings. Strunz P et al. (2004) also studied the effect of heating on plasma-sprayed TBCs using SANS and compared the results with those obtained by mercury porosimetry. Kulkarni A et al. (2006) have also used SANS to study EB-PVD thermal barrier coatings and quantified the voids in terms of component porosities, anisotropy, size, and gradient through the coating thickness.

17.5.5 Ultra Small Angle X-Ray Scattering

Ultra small angle X-ray scattering (USAXS) has been used to characterize EB-PVD thermal barrier coatings [Flores Renteria A, et al. (2007)]. Two data collection methods

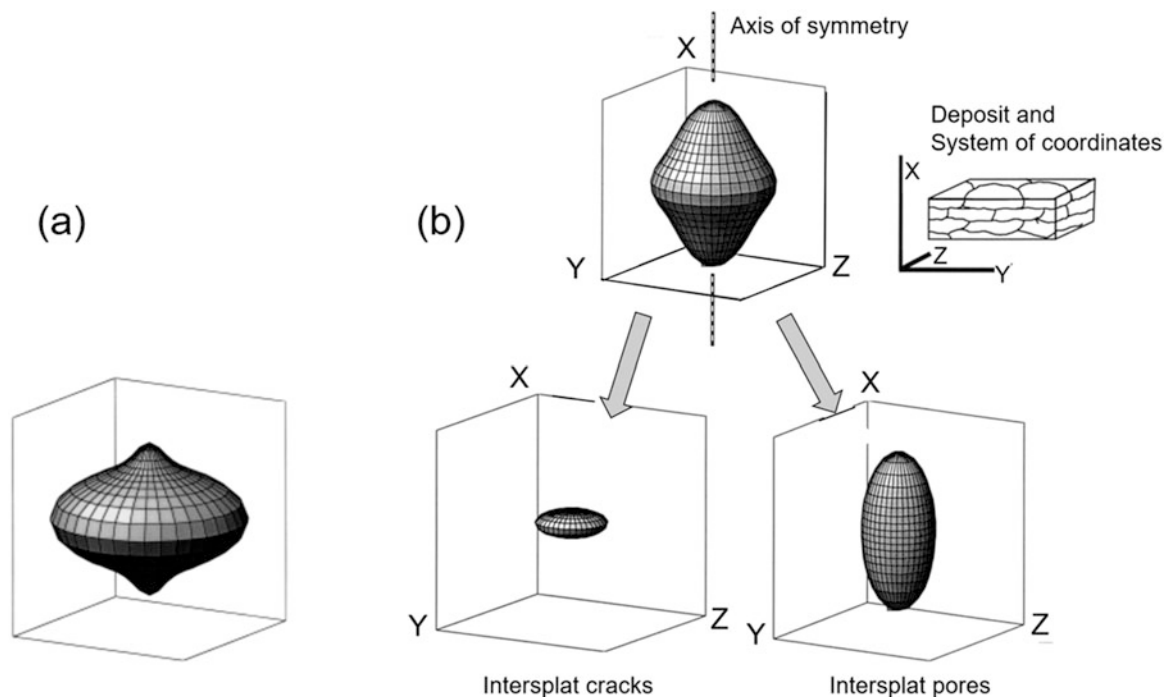


Fig. 17.10 Apparent Porod surface area distribution of (a) water-stabilized plasma sprayed alumina and (b) gas-stabilized plasma-sprayed alumina separated into two void surface areas: Left (prolate

ellipsoid) representing intra-lamellar cracks and right (elongated ellipsoid) representing interlamellar pores [Ilavsky et al. (1999b)]. (Reprinted with kind permission from Elsevier)

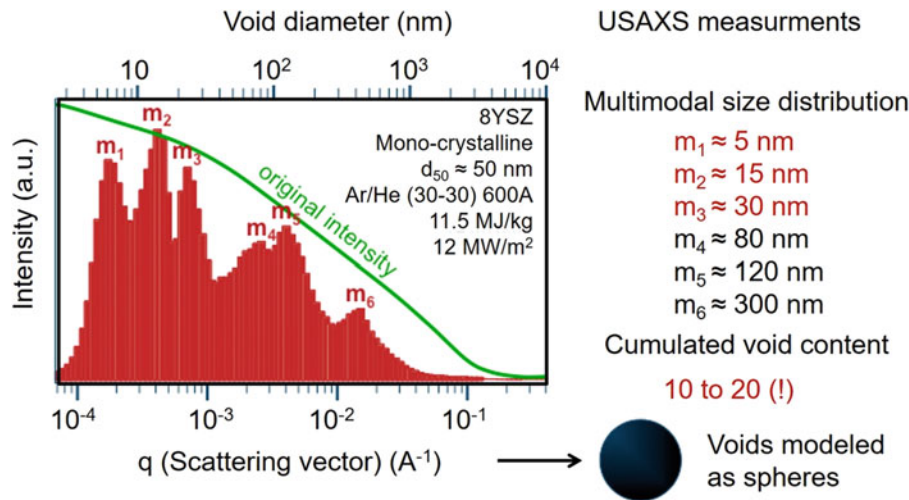


Fig. 17.11 Evolution of the USAXS signal intensity with the scattering vector, q (in \AA^{-1}) and the calculated corresponding pore size distributions for YSZ suspension plasma-sprayed coating with particle

mean size: 50 nm, Ar-He plasma, 30-mm standoff distance [Bacciochini A et al. (2010a, b)]. (Reprinted with kind permission from Elsevier)

were combined. In the first, the scattered intensity was measured as a function of $|q|$ (see Eq. 17.6) for each orientation of the sample azimuthal angle α . In the second, the scattered intensity at a fixed $|q|$ was measured as a function of α by rotating the sample in the beam. Variations in the scattering anisotropies observed at different $|q|$ were associated with the variation in the microstructure anisotropy at different length scales and gave, thus, a quantitative map as a function of the sizes of the scattering populations. The anisotropies in the scattered intensity at different $|q|$ values were presented as a function of azimuthal angle with respect to the substrate-normal direction [Kulkarni A, et al. (2006)]. Flores Renteria A, et al. (2007) have studied, via USAXS-measurement, the stereometric characteristics of the pores within EB-PVD TBCs. A subsequent use of the appropriate statistically representative values made it possible to predict the thermal conductivity by a noninteracting scheme. The projected values agreed well with the measured values.

USAXS measurement was reported by Bacciochini A et al. (2010a, b) to characterize suspensions plasma-sprayed YSZ (50-nm average particle diameter, Ar-He plasma gas mixture, 30-mm spray distance). Figure 17.11 shows the evolution of the signal intensity with the $|q|$ scattering vector (in Angström) and the calculated corresponding pore size distribution, assuming that the pores have spherical shapes. Rotating the analyzer and recording the scattered photons received by the detector enabled the measurement of the X-ray scattering from the sample. USAXS data were fully corrected for instrument effects and analyzed using Igor Pro1 software from Wave Metrics Inc. (Oswego, OR, USA) coupled to Irena1 package for analyzing small angle scattering data. The total void content was about 14.3%. The

void distribution was multimodal and characterized by several modes' diameters (i.e., average diameter of an equivalent monomodal distribution) contrary to micrometer sized YSZ coatings, which usually exhibited a bimodal distribution of voids [Bacciochini A et al. (2010a, b)]. In SPS coatings, the typical void mode diameters that were identified are $m_1 < 5$ nm, $m_2 < 15$ nm, $m_3 < 30$ nm, $m_4 < 80$ nm, $m_5 < 120$ nm, and $m_6 < 300$ nm. The most numerous population of voids corresponded to voids exhibiting mode diameter $m_5 < 120$ nm. It is important to underline that commonly applied porosity characterization methods, based on analysis of cross-sectioned coatings or on liquid impregnation, are not suitable to address the void content of SPS nanometer-sized coatings. On the other hand, combination of helium pycnometry and ultra small angle X-ray scattering proved to be suitable for quantifying SPS deposits void contents with sufficient details. Large populations of nanometer and larger voids have been detected. Their characteristic dimensions cover four orders of magnitude (i.e., from 1 to 10,000 nm). About 90% of voids (by number) in the coatings exhibit characteristic dimensions smaller than 50 nm. The photon scattering phenomena and thermal resistance effects are most likely responsible for the significantly lower thermal diffusivity values (about $0.025 \text{ mm}^2/\text{s}$) measured in the temperature range of 20–300 °C for these SPS coatings compared to typical values for micrometer-sized conventional APS coatings.

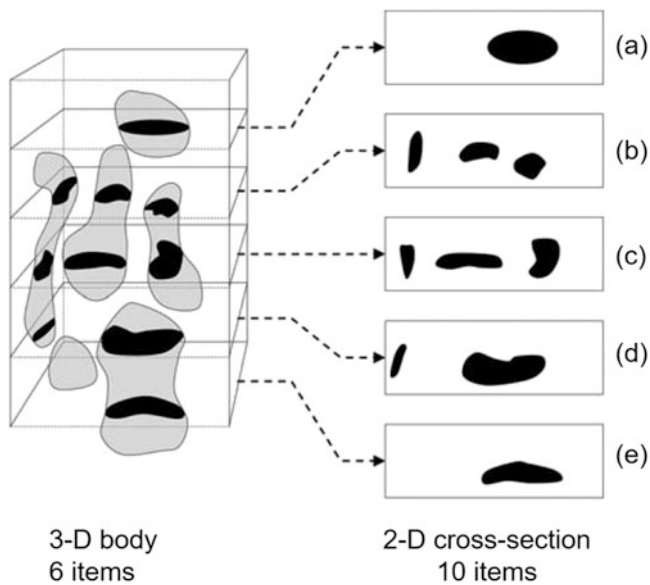


Fig. 17.12 Analyses of the Wicksell corpuscular problem [Antou G, et al. (2004a, b) and Montavon G and G Antou (2007)]. (Reprinted with kind permission from Springer Science Business Media, copyright © ASM International)

17.5.6 Stereological Protocols (Coupled to Image Analysis)

Assuming that resolution limits are considered, porosity within a microstructure can be easily detected by image analysis due to the high degree of contrast between the dark pores (voids) and the most highly reflective coating material [Deshpande S, et al. (2004)]. However, image analysis gives only 2-D pore distributions of the coating cross-section (the intersection of the structure with this specific plane). If the cross-section images can show the effect of the coating densification, for example, after laser remelting [Antou G, et al. (2004a, b)], it does not mean that such images are representative of the real 3-D structure. It is illustrated in Fig. 17.12 after [Montavon G and G Antou (2007)] and representing the Wicksell's corpuscle problem demonstrating that “an accurate estimation of the number of objects of interest cannot be obtained from profile counts on individual cross sections.” This figure illustrates that the three bodies of the 3-D structure cannot be represented by the ten objects resulting from 2-D cross-sections (a, b, c, d, e).

According to Montavon G and G Antou (2007), the procedure to analyze different 2-D cross-sections of the 3-D coating comprises successively

- sample preparation,
- image acquisition,
- image pretreatment,
- image treatment, and finally,

- stereology implementation to achieve the quantitative interpretation of the coating architecture.

The image acquisition is made either with either, optical microscopy (OM) equipped with cameras for image analysis, but the resolution is low, or by SEM. For SEM, BSE imaging, which is sensitive to the average atomic number of the sample, gives sufficient contrast between dissimilar phases for automatic threshold determination due to the electron–matter interaction. With OM magnification is generally below 500, while with SEMs magnification values can be up to 1000 or more. If high magnification allows seeing many details (pores and cracks), the small surface (between about one-tenth and one square millimeter) analyzed does not necessarily represent the whole coating. Experience indicates that image characteristic dimension should be between 10 and 15 times larger than the objects of interest (voids) to be analyzed to account for the representative elementary volume (REV) of the structure. Thus, statistical measurements (in general 10–15 locations within the coating) are necessary to ensure a representative sample for qualitative analysis. Moreover low-magnification images (100×) can also be taken to reveal larger cross-sections of the coating for porosity analysis as did, for example, Hanson TC, Settles GS (2003) to analyze 316 L stainless steel HVOF-sprayed coatings.

Several mathematical filters can be implemented to reveal specific structural data from the initial image [Russ JC (1995)]. The objective of this pretreatment is to remove singularities and to reveal feature outlines prior to morphological analysis. It consists of altering the pixel values (i.e., pixel intensities) using mathematical treatments. Four main types of filters are usually implemented at this stage of the treatment [Antou G, Montavon G (2007)]:

- Filters that make it possible to modify the image contrast (linear or nonlinear filters).
- Arithmetic and logic filters.
- Spatial filters (linear or nonlinear filters).
- Frequency filters (fast Fourier transform, FFT, applicable only on square images).

An example of such a processing is presented in Fig. 17.13 after Antou G, Montavon G (2007) showing the different treatments to discriminate globular pores from cracks of the SEM image of Al_2O_3 –13TiO₂ coating plasma sprayed in air.

As coating architectures are heterogeneous, they must be characterized at several scales and the size of the representative elementary volume (REV) must be defined to describe the overall structure of the material [Antou G, Montavon G (2007)]. The REV must be small enough to resolve the thinner details of the structure: high magnification and image resolution. But the REV must be large enough to

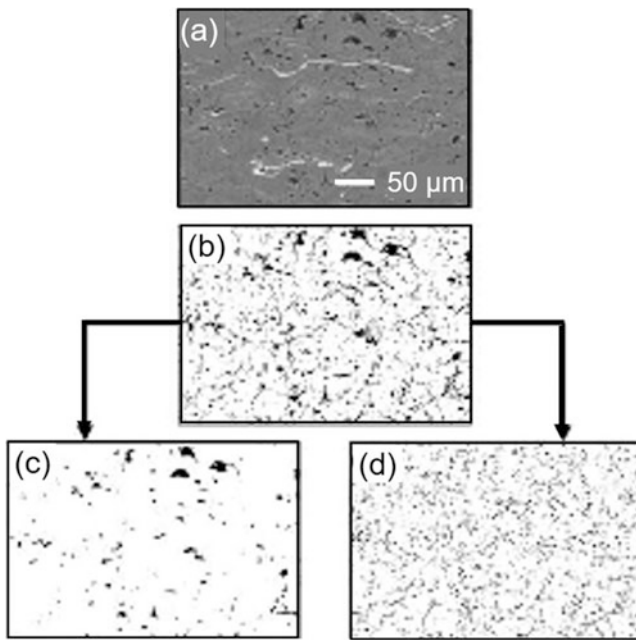


Fig. 17.13 SEM images of $\text{Al}_2\text{O}_3\text{-13TiO}_2$ plasma-sprayed coating in air (a) initial SEM image, (b) image treated by an image analysis software, (c) globular pores, and (d) cracks isolated after several filtering and morphological protocols [Antou G, Montavon G (2007)]. (Reprinted with kind permission from Springer Science Business Media, copyright © ASM International)

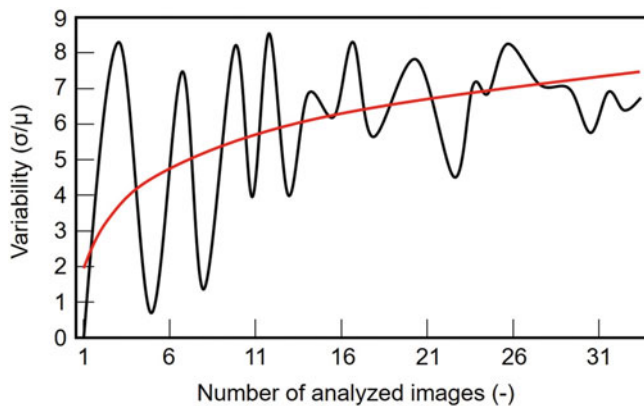


Fig. 17.14 Determination of the number of images to be analyzed [Antou G, Montavon G (2007)]. (Reprinted with kind permission from Springer Science Business Media, copyright © ASM International)

describe the whole material structure: low magnification. To find the compromise, the evolution of the result variability (standard deviation over average value) must be followed as a function of the considered number of images (Fig. 17.14). The appropriate number of images corresponds to the value where this function tends toward an asymptote.

For example, Zhang XC et al. (2009b, c) have proposed the following procedure divided into four steps, that is, gray level transformation, fuzzy enhancement of image, binary

segment of image, and removing the impurities and identification of pores and micro-cracks. Venkataraman R et al. (2007) have processed and analyzed the digitally stored images with image analysis software such as ImageJ and Adobe Photoshop to identify the pores and their distribution. Elsebaei A et al. (2010) have used the Matlab code to identify the pores and their distribution. The measured data of porosity can be highly scattered. The adjustment of the porosity dataset almost does not lead to the variation of the mean value of porosity calculated from the Gaussian distribution, as shown by Zhang XC et al. (2009b). However, the adjustment of the porosity dataset by subtracting the two largest and two smallest data greatly decreases the variance. It was also observed that the measured data of coating porosity might follow the Weibull distribution [Venkataraman R et al. (2007)]. The first limitation of this method is the limited resolution, which makes difficult to take into consideration features smaller than $0.1\ \mu\text{m}$ in average value. So, the technique cannot be used to characterize nanometer-structured coatings. The second limitation is the artifacts (i.e., pullouts, scratches) that result from the cutting and polishing steps [Sauer JP (2005), Puerta DG (2006), Russ JC (1995), Nolan DJ, Samandi M (1997)]. This can be particularly the case for cermet coatings where the hard-ceramic particles imbedded within the soft metal matrix can be pulled out easily if the polishing step is not made carefully. For example, Nolan DJ, Samandi M (1997) have shown that the potential for smearing over (or filling in of) pores is important and insufficient polishing can result in considerable underestimation of porosity, thus providing incorrect representation of coating structure.

This method of image analysis is extensively used to characterize the coatings void structure, for example, according to the spray process [Kang H-K, Bong Kange S (2004), Saravanan P, et al. (2000), Yang G, et al. (2001)], the spray conditions [Scrivani A, et al. (2008)], the spray angle [Tillmann W, et al. (2008a, b)], and the heat treatment [Siebert B, et al. (1999)].

The coating porosity is often measured using the Delesse principle [Underwood EE (1970), Russ JC, DeHoff RT (1999)]: if the porosity is randomly distributed throughout the coating, then the percentage of porous area in a coating cross section is identical to the percentage of porous volume in the entire coating. Fowler DB et al. (1990) have shown that image analysis can reproducibly detect and measure microstructural features (pores, cracks, etc.) within thermal spray coatings. They have statistically tested the reliability of these methods for specific experiments and they assume 95% confidence level. However, coatings are nonuniform in all spatial directions and the 2-D approach is not necessarily representing well the structure. Several quantitative tools allowing the quantification of complex structures exist. They are known as stereological protocols [Montavon G,

Antou G (2007)] and have been used to quantify some specific features of thermal spray coatings [Montavon G, et al. (1998), Leigh S-H, Berndt CC (1999), Antou G, et al. (2006)]. Stereological protocols of the first order aim at statistically quantifying 3-D structures from 2-D randomly oriented plane sections.

NIST was the first to develop, Object-Oriented Finite (OOF) Element Analysis of Microstructures (<http://www.ctcms.nist.gov/oof/>), a program designed to help materials scientists to calculate macroscopic properties from images of real or simulated microstructures. OOF reads an image, assigns material properties to features in the image, and conducts virtual experiments to determine the macroscopic properties of the microstructure. At the beginning two separate versions existed, one only solving elasticity problems and the other solving coupled elasticity and thermal diffusion problems. Now the current version of OOF is OOF2, which improves on OOF1 in a number of ways. OOF2 can solve a much larger variety of physics problems and can be easily extended to cover even more. This program was, for example, used to characterize and predict properties of plasma-sprayed YSZ coatings [Kulkarni A, et al. (2003), Wang Z, et al. (2003), Michlik P, Berndt CC (2006), Jadhav AD, et al. (2006)], and arc-sprayed WC-FeCSiMn coating [Tillmann W, et al. (2011)].

University of Technology of Belfort-Montbéliar (France) also developed a software package TS2C focused on

estimation of the thermal conductivity of thermally sprayed coatings [Bolot R, et al. (2005), Costil S, et al. (2007), Bolot R, et al. (2011)]. Bobzin K et al. (2012) showed that when using 3-D models, the results of the virtual testing and asymptotic homogenization methods match each other more closely compared with the conventional 2-D models. Homogenization methods are based on the assumption that a specific small part of the microstructure can be considered to be representative for the entire material. The dimensions of the representative volume element (RVE) are much smaller than those of the entire microstructure. It requires that the RVE contain a sufficient number of microstructural inhomogeneities, so its morphology is equivalent to that of the entire microstructure [Bobzin K et al. (2012)]. Figure 17.15 presents the way the 3-D representation of the RVE has been derived.

The statistical 3-D reconstruction approach has been used by Bobzin K et al. (2012) to calculate the effective properties of a typical YSZ coating in 3-D domain. The calculated (with this method) effective values of Young's module and the thermal conductivity of the coating agree with the results of micro-indentation and laser flash measurements. The definition of the distance between 2-D images (h), used to reconstruct the 3-D representation, is critical for the correctness of the calculated effective properties [Bobzin K et al. (2012)].

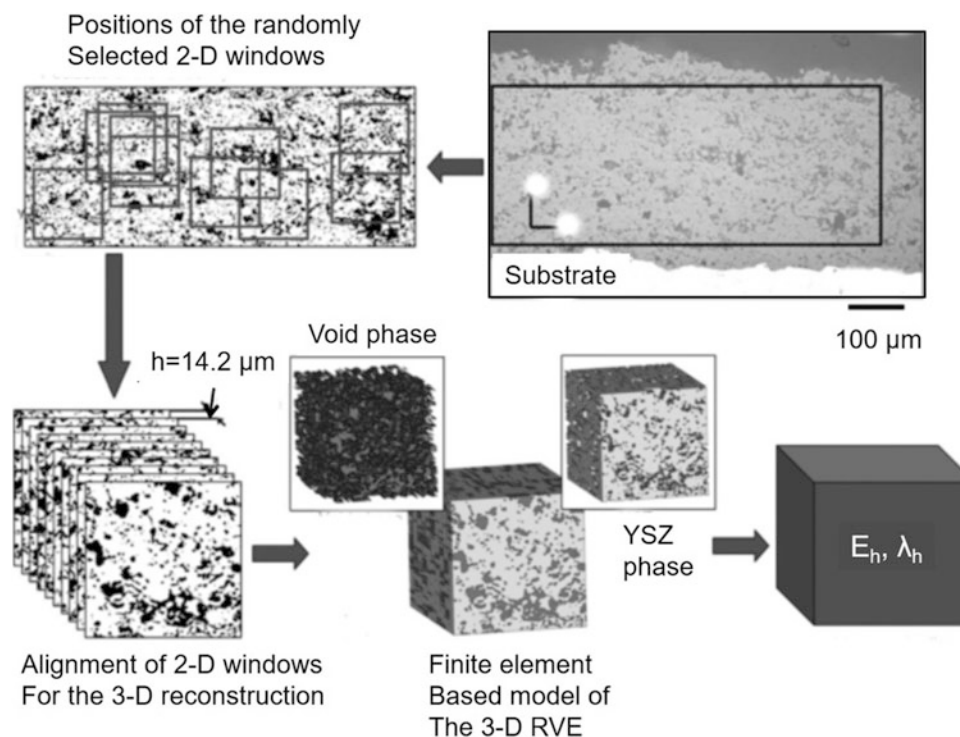


Fig. 17.15 Homogenization of thermally sprayed YSZ coatings obtained by statistical 3-D reconstruction approach [Bobzin K et al. (2012)]. (Reprinted with kind permission from Springer Science Business Media, copyright © ASM International)

17.5.7 Electrochemical Impedance Spectroscopy

The percolation of an electrolyte inside the interconnected void network allows quantifying the void fraction connected to the substrate by analyzing the chemical reaction (passivation most of the time) at the substrate/electrolyte interface. The electrochemical impedance spectroscopy (EIS) technique consists hence in measuring the impedance of the electrochemical cell. In order to access the charge transfer resistance or polarization resistance, EIS results have to be interpreted with the help of a model of the interface. To make an EIS measurement, a small amplitude signal, usually a voltage between 5 and 50 mV, is applied to a specimen over a range of frequencies of 0.001–100,000 Hz. The EIS instrument records the real (resistance) and imaginary (capacitance) components of the impedance response of the system. Depending upon the shape of the EIS spectrum, a circuit model or circuit description code and initial circuit parameters are assumed and input by the operator. The program then fits the best frequency response of the given EIS spectrum to obtain the fitting parameters. The quality of the fitting is judged by how well the fitting curve overlaps the original spectrum. By fitting the EIS data, it is possible to obtain a set of parameters, which can be correlated with the coating condition.

A typical EIS for measuring connected porosity in plasma sprayed TBCs is presented in Fig. 17.16 from Antou G et al. (2006). They have used a flat cell with a volume of 300 mL at room temperature. The gray alumina sample was used as the working electrode (exposed area of 1 cm²). A platinum mesh was used as a counter electrode, and an Ag/AgCl electrode was used as a reference. A 0.01 mol/L K₃Fe(CN)₆/K₄Fe

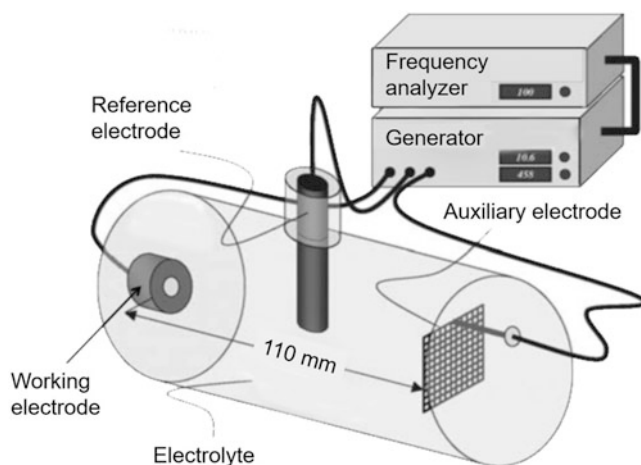


Fig. 17.16 Schematic representation of electrochemical impedance measurement system [Antou G et al. (2006)]. (Reprinted with kind permission from Springer Science Business Media, copyright © ASM International)

(CN)₆ aqueous solution was selected as electrolyte due to its highly reversible electrochemical exchange current density and its minimal interference with the system. The three-electrode system was connected to EG&G Parc Model K0235 EIS measurement system. A sinusoidal voltage perturbation of 10 mV amplitude and a frequency range of 1 mHz–100 kHz was input to the system, and the system response was recorded as a Bode plot.

The immersed coating surface behaves as the working electrode [Zhang J, Desai V (2005), Jayaraj B, et al. (2004)]. The connectivity of a pore network is related to the quantity of voids, which connects the substrate to the surrounding atmosphere.

A similar system was used by Zhang J and V Desai (2005), Jayaraj B et al. (2004), Antou G and G Montavon (2007) and Anderson PS et al. (2004) to study plasma sprayed TBCs. Bolelli G et al. (2009) have also characterized the connected porosity of high-velocity suspension flame sprayed (HVSFS) Al₂O₃ coatings. Kawakita J et al. (2003) have studied by EIS the through-porosity of Hastelloy-C High-Velocity Oxy-Fuel (HVOF) sprayed coatings by quantitatively analyzing dissolved substances derived from coated steel during immersion in HCl solution. Furthermore, Koivuluoto H et al. (2008) investigated the denseness of cold-sprayed Cu, Ni, and Zn coatings with corrosion tests to get more information about existing through-porosity (open-porosity). The corrosion tests used were open-cell potential measurement and salt spray fog test.

As previously mentioned, the test of deionized water droplet percolation through the coating indicated that the smallest void diameter into which a liquid such as water percolates through the coating void network was in the order of the micrometer. So, the EIS technique is not adapted to most of the nanometer-sized thermal spray coatings.

17.6 Adhesion–Cohesion

17.6.1 Introduction

The quality and performance of thermal spray coatings are strongly dependent on the adhesion between the coating and substrate because the debonding of coating will result in the collapse of the sprayed system. However, the prediction and control of coating adhesion are complex as it depends on:

- Spray process and operating conditions used.
- Feedstock, its particle size distribution and morphology.
- Substrate material: oxidation stage (oxide composition and thickness); roughness (peaks height in comparison with the splat mean size, and peak separation distance, characterized by the root mean square roughness $R_{\Delta q}$, that is, the root mean square average of the roughness profile

ordinates); cleanliness (removal of surface pollution and grit residue); and preheating prior to spraying at a temperature sufficient to get rid of adsorbates and condensates.

- Residual stresses: they depend on the substrate-sprayed material couple, spray conditions, and substrate mean temperature.
- Environmental conditions such as the surrounding atmosphere temperature and humidity, externally generated vibration transmitted into the specimen at the time of testing.

Moreover, the structure of thermal-sprayed coatings is different from that of bulk materials; it generally involves layered splats with a contact surface between successive layers of 15–60% of their surface, unmolten particles, globular pores, cracks. Thus, the basic bonding mechanisms between thermal spray coatings and substrate strongly depend on real contacts between successive splats as well as between individual splats and the substrate. They are classified into three major groups:

- mechanical interlocking or anchoring,
- metal-to-metal bonding (diffusion phenomenon), and,
- chemical bonding (formation of an intermetallic compound with a substrate).

The service failure mode can be described as interfacial (adhesive), cohesive, or mixed interfacial/cohesive [Lin CK, Berndt CC (1994)]. Adhesion can be defined through fracture mechanics [Berndt CC, McPherson R (1981)] that consider the energy required to initiate or propagate cracks and evaluate the adhesion of the coating system in terms of fracture toughness [Heintze GN, McPherson R (1988)]. The experiment must establish the equilibrium condition where the elastic energy provided by an external force (as defined by the geometry of the specimen and applied load) is balanced by the propagation of a stable crack [Berndt CC, McPherson R (1981)]. Over a critical value of the strain energy release rate, G_c (stated in J/m^2) crack propagation occurs and thus failure.

17.6.2 Simple Tensile Adhesion Test

The tensile adhesion test (TAT) is used as a routine quality control tool for thermal spray coatings. The TAT arrangement is illustrated in Fig. 17.17a after [Lin CK, Berndt CC (1994)]. In this test, the coated sample (a cylinder \varnothing 25.4 mm \times 25.4 mm long) is glued to an uncoated similar counterpart that is just grit blasted and then tested in tension in a universal testing machine. The value of the tensile load, at which the separation of the coated–uncoated parts occurs, is registered and transformed in an adhesion value “bond

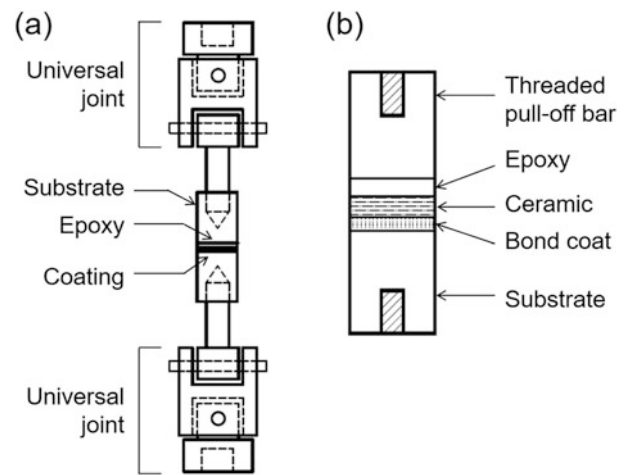


Fig. 17.17 (a) Tensile adhesion test configuration specified by ASTM C633–79 and (b) tensile adhesion test with cohesive and interfacial ruptures [Lin CK, Berndt CC (1994)]. (Reprinted with kind permission from Springer Science Business Media, copyright © ASM International)

strength, by calculating the load/area relation [Lima CRC, Guilemany JM (2007)]. Four main standards are used in industry or research laboratories [Lin CK, Berndt CC (1994)]: DIN 50160-A (Germany), AFNOR NF A91–202–79 (France), JIS H8666–80 (Japan), and ASTM C633–01 (2008) (USA) [17.A1]. These standards differ in their specimen geometry (e.g., cylinder diameter: 25.2 mm for ASTM against 40 mm for DIN and cylinder length 25.4 mm for ASTM and 50 mm for DIN), test methodology, and failure analysis [Lin CK, Berndt CC (1994)].

The failure region indicates the type and characteristic of the failure, according to Fig. 17.17b, that shows a simple coating system. The failure modes of a coating under TAT conditions are:

- interfacial failure, which occurs along the coating/substrate interface,
- cohesive failure within the coating, and,
- mixed-mode failure, which is a combination of the first two modes.

If the coating is a duplex system, as in a TBC, the coating cohesive failure could be located within the bond coat, within the ceramic top-coating or at the bond coat/ceramic interface. Some failures may occur in a combined way, starting in a region and then expanding to other ones [Lima CRC, Guilemany JM (2007)].

TAT measurement, whatever maybe the standard used, presents some shortcomings the most important of which is glue diffusion within the coating, which can artificially improve the apparent tensile resistance value [Wigren J, Täng K (2007)]. It appears that the tensile strength achieved

on a thermal sprayed coating is very dependent on the penetration of the epoxy and the pressure being used during curing. They showed that the tensile strength of a Ni-5Al/Alumina system can vary between 15 and 60 MPa. Such variations in the tensile resistance of the coating are not observed in cases where the coating is dense enough to prevent epoxy penetration (such as WC/Co). The alignment of test fixtures is also very important because it can create nonuniformly distributed stress or stress singularities within the coated sample, such that the failure is not only controlled by the magnitude of the applied tensile force. That is why, as shown in Fig. 15.17a, universal joints are used to center the TAT arrangement.

Han W, et al. (1993a, b) used finite-element analysis to study the stress distribution along the coating/substrate interface; they found that the stress distribution was nonuniform and the average adhesion strength underestimated. A modified specimen, 50% longer than the standard size, was proposed so that a uniform stress can be obtained along the interface. In their tests, they found that the determined mean tensile strength with the elongated specimen was 21% higher than that determined with the ASTM C633-79 standard specimen. So, they concluded [Han W, et al. (1993a, b)] that elongated specimens provide more accurate estimates of bond strength than ASTM C633-79 standard specimens.

TAT has been used intensively for many applications, for example, to investigate the effect of grit blasting [Bialucki P, Kozerski S (2006), Amada S, Hirose T (1998), Staia MH, et al. (2000)], substrate preheating prior to spraying [Pershin V, et al. (2003)], coating thickness [Krishnamurthy N, et al. (2009)], spray angle [Bahbou MF, et al. (2004)], sprayed particle size distribution, and morphologies [Li C-J, Wang Y-Y (2002)].

17.6.3 Other Types of Tensile Tests

Different tests have been defined [Leigh SH, Berndt CC (1994), Rickerby DS (1988), Du H, et al. (2005)] and few examples are given below.

The modified configuration of the TAT, called single bar (SB) method, according to Leigh SH, Berndt CC (1994) has been designed for self-alignment and to accommodate flat and wide thermal sprayed-coated specimens, see Fig. 17.18, with sizes up to $152 \times 152 \times 152$ mm. The specimen is positioned between two plates that are 178×178 mm wide. The bottom plate has a 25.4 mm diameter hole at the center, through which the glued pull-off bar passes and provides tensile stress to the specimen [Leigh SH, Berndt CC (1994)]. This bottom plate and the universal joints at the

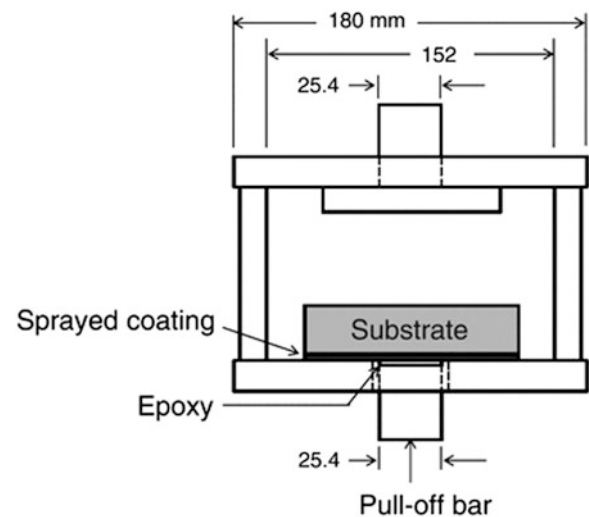


Fig. 17.18 Schematic of TAT assembly for single bar (SB) method [Leigh SH, Berndt CC (1994)]. (Reprinted with kind permission from Springer Science Business Media, copyright © ASM International)

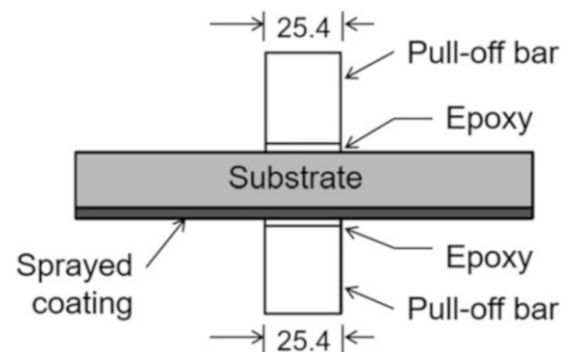


Fig. 17.19 Schematic of TAT assembly for double bar (DB) method [Leigh SH, Berndt CC (1994)]. (Reprinted with kind permission from Springer Science Business, copyright © ASM International)

top and bottom of the fixture result in a self-aligning TAT system. Several tests can be performed on each flat substrate, since the pull-off bar can be repositioned for each TAT.

Another modified TAT, called double bar (DB) method, is shown in Fig. 17.19 from [Leigh SH, Berndt CC (1994)]. This method does not require a special testing fixture except two pull-off bars and two universal joints, which are attached to both sides of the flat specimen. As for SB, several tests can be performed on each flat substrate, since the pull-off bar can be repositioned for each TAT, the problem being to maintain the alignment between the two bars.

For coatings with a strong adhesion (> 60 MPa), such as those obtained with D-gun or high-power HVOF, the adhesions are measured according to the pull-off method [Rickerby DS (1988)] with the application of a force normal

to the coating–substrate interface. A schematic diagram of one of these tests is presented in Fig. 17.20 from [Du H, et al. (2005)]. The substrate comprises two parts with conical shapes: one female and one male made of the same material as that of the used substrate. The surface of joined both parts is continuous, and grit blasted to anchor the sprayed coating. Du H, et al. (2005) have sprayed WC–Co powder using a D-gun spray system, onto stainless steel substrate; the tester was also made of stainless steel. They found adhesions values ranging between 120 and 150 MPa, depending on the spray conditions.

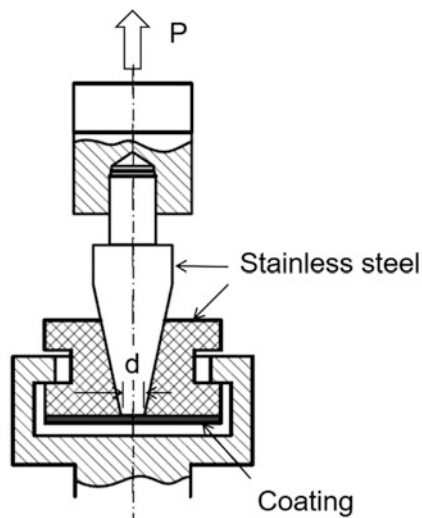


Fig. 17.20 Schematic diagram of the direct pull-off test [Du H, et al. (2005)]. (Reprinted with kind permission from Elsevier)

17.6.4 Shear Stress

In many cases shearing plays a key role in coating peeling off. The principle of a shear stress test is very simple, as shown in Fig. 17.21a. The coating is deposited onto either plane (Fig. 17.21a) or cylindrical (Fig. 17.21b) substrate and a force parallel to the coating is applied at its extremity as shown schematically in Fig. 17.21a, b. While the shear test piece is rather complex to prepare, it needs no adhesive agent. Moreover, the adhesion strength can be measured using specimens, which are cut out from the products [Era H, et al. (1998)].

The main disadvantage of this shear test is a possible stress concentration [Era H, et al. (1998)] at the corner of the protruded step of a test piece, indicated by a dotted arrow in Fig. 17.21a. It results in a lower value than the true shear strength. That is why Era H, et al. (1998) proposed a shear test piece with a semicircular notch at the corner of a protruded step. Calculations and measurements have demonstrated that the reduction of the stress concentration in a notched test piece (radius over 0.3 mm) is effective for a coating that has a Young's modulus equal or larger than that of substrate. The sprayed specimen (Cr_3C_2 cermet coating on mild steel) was cut using a precision machining tool into conventional shear test pieces assuming that no damage occurs to the coating by this machining. Figure 17.21c shows the shear test jig they used and Fig. 17.21d shows the appearance of the shear test. The shear test jig was precisely made of sintered WC–Co cermet. The clearance between the punch and die was measured to be about 20 μm , corresponding to the interface zone between coating

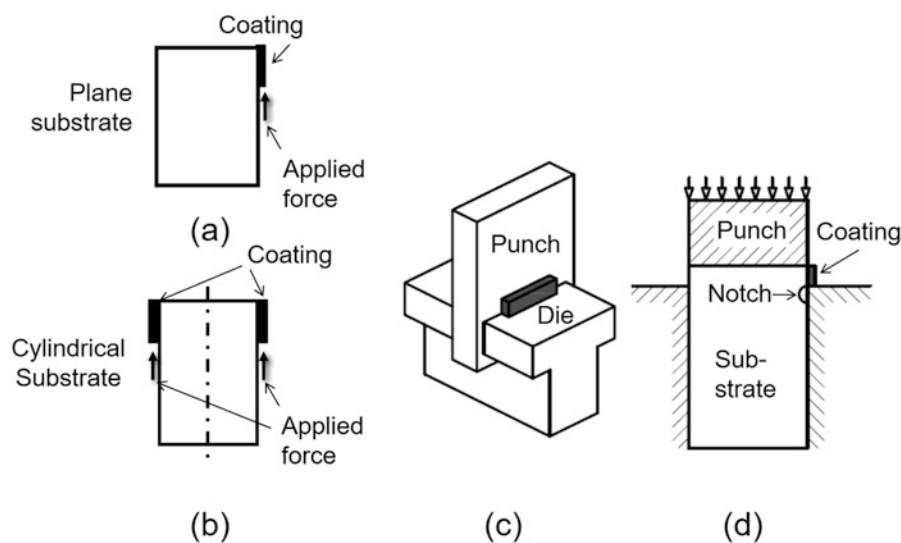


Fig. 17.21 Schematic illustration of shear test: (a) Plane substrate, (b) cylindrical substrate (c) shear test jig, and (d) schematic illustration of shear test [Era H, et al. (1998)]. (Reprinted with kind permission from Elsevier)

and roughened substrate. The critical shear stress, τ_c is calculated by

$$\tau_c = \frac{F}{wl} \quad (17.17)$$

where F is the force applied, l is the length of the coating, and w is the coating thickness – 20 μm .

17.6.5 Fracture Mechanics Approach

The fracture mechanics approach consists in establishing the equilibrium condition where the elastic energy provided by an external force (as defined by the geometry of the specimen and the applied load) is balanced by the propagation of a “stable” crack [Lin CK, Berndt CC (1994)]. One form of this energy-balance criterion derives the strain energy release rate, G (in J/m^2) defined as:

$$G = \frac{\partial(W_e - U)}{\partial A} \quad (17.18)$$

where W_e is the work done by external forces (J), U is the elastic energy stored in the system (J), and A is the crack surface area (m^2). It is convenient to write G as:

$$G = \frac{P^2}{2w} \frac{dC}{da_x} \quad (17.19)$$

where P is the force required to extend a crack (N), a_x is the crack length (m), w is the coating thickness (m), and C is the compliance, which is the reverse of the slope of the curve load displacement (m/N). The critical value G_{ic} corresponds to the coating adhesion limit. The strain energy release rate can be related to the fracture toughness, characterizing the interface, K (stated in $\text{N}/\text{m}^{3/2}$), by

$$K = \frac{\sqrt{E' \times G}}{1 - \nu^2} \quad (17.20)$$

where E' is the elastic modulus (MPa), and ν is the Poisson's ratio. The toughness represents the ability of a material to deform plastically and absorb energy in the process before fracture occurs.

The TAT can be analyzed according to the fracture mechanics concepts, where the specimen configuration for the TAT geometry is considered as a circumferentially cracked bar (Fig. 17.22). The average fracture strength can be converted into fracture toughness [Lin CK, Berndt CC (1994)] by using Eq. 17.21.

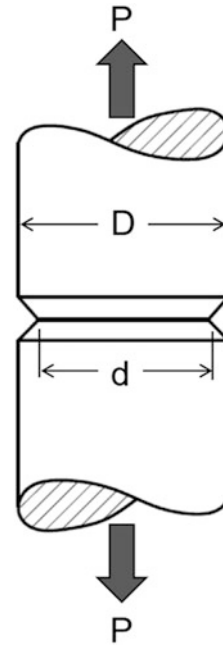


Fig. 17.22 Tensile adhesion test specimen of a circumferentially cracked bar for K_{Ic} testing [Lin CK, Berndt CC (1994)]. (Reprinted with kind permission from Springer Science Business Media copyright © ASM International)

$$K_{ic} = P \left[-1.27 + 1.72 \left(\frac{D}{d} \right) \right] D^{-1.5} \quad \left(0.4 \leq \frac{d}{D} \leq 0.9 \right) \quad (17.21)$$

where K_{ic} is the critical fracture toughness ($\text{N}/\text{m}^{1.5}$), P is the fracture force (N), D the outside diameter of the bar (m), and d is the inside diameter in the circumferentially notched bar (m) (see Fig. 17.22). The average reduced-area ratios range between 0.74 and 0.86. This reduction in area corresponds to a reduced failure stress of about 80%, which correlates reasonably well with the underestimation factor of approximately 83% found by Han W, et al. (1993a, b).

For HVOF-sprayed coatings, the tensile adhesion test is widely used. However, the edge of the substrate is heavily deformed and rounded due to the high impact energy of the sprayed particles. This deformation causes a large scatter of the adhesion test results [Watanabe M, et al. (2008)]. To avoid that a pre-crack was formed at the interface of a conventional tensile adhesion test specimen, the coating was sprayed onto the cylindrical substrate used in the ASTM C633-79 test. Before spraying, a carbon layer was placed along the substrate edge with 3 mm width from the edge in order to introduce “a weak bonded region” at the interface as indicated with the black rings in Fig. 17.23. A pencil of 2B grade was used to place the carbon layer. The

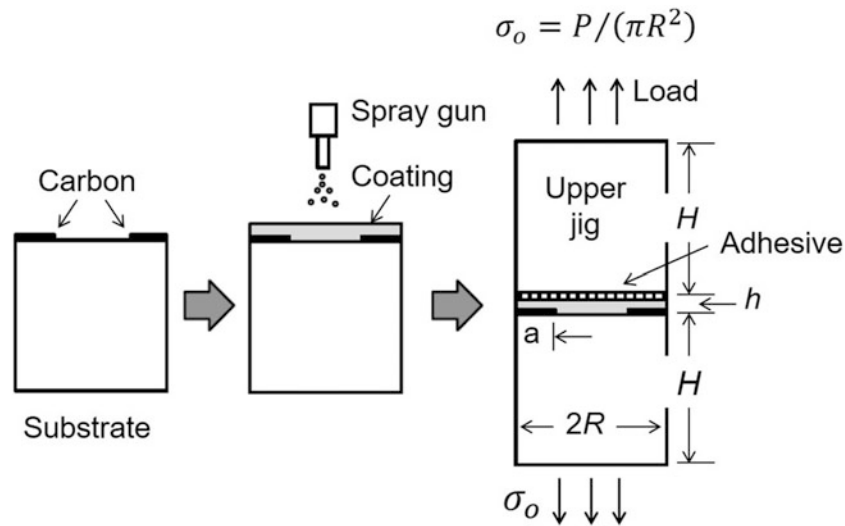


Fig. 17.23 Procedure of sample preparation for the modified adhesion test and schematic of a sample configuration [Watanabe M, et al. (2008)]. (Reprinted with kind permission from Elsevier)

substrate was set in a lathe-turning machine and rotated. The sharpened pencil was touched on the surface by the precise position controller in order to achieve a uniform carbon layer. This system was used to determine the interfacial toughness, according to the fracture mechanics concepts.

According to Eq. (17.19), the strain energy release rate corresponds to crack opening. Clyne TW and SC Gill (1996) have shown, however, that the analysis of interfacial debonding is complicated by the fact that the stress field at the crack tip may not represent conditions of pure crack opening (mode I). “Depending on the toughness of the interface and of the two media on either side,” crack propagation may continue within the interface, rather than seeking a mode I path in some other direction, even though the interfacial path is heavily “mixed mode” (i.e., has a substantial shear component at the crack tip) [Clyne TW and SC Gill (1996)]. The so-called phase angle, ϕ , is related to the crack-tip stress-intensity factors, K_I (see Eq. 17.22), for mode I and mode II loading by:

$$\phi = \tan^{-1} \left(\frac{K_{II}}{K_I} \right) \quad (17.22)$$

so that $\phi \sim 0$ represents pure opening conditions (mode I) and $\phi \sim 90$ represents pure shear (mode II). The critical value of critical strain energy release rate G_{ic} rises as a shear component is introduced, since this will encourage dissipation of energy at and immediately behind the crack tip as a result of frictional rubbing between asperities. It is expected that roughening of the substrate surface will give rise to a more substantial increase in interfacial toughness if there is a large shear component to the crack-tip driving force. As the dependence of G_{ic} on ϕ is significant, especially over 45° , the interfacial fracture energy values should always be quoted

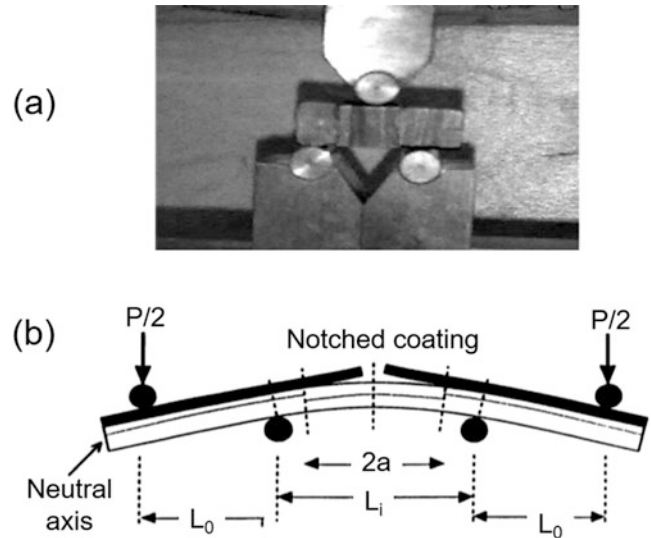


Fig. 17.24 Loading arrangement and specimen geometry used to measure coating adhesion (a) three-point adhesion test [Rammo NN et al. (2009)] and (b) four-point adhesion test [Lin CK, Berndt CC (1994)]. (Reprinted with kind permission from Springer Science Business Media, copyright © ASM International)

together with ϕ , which values vary widely between different test procedures and are also affected by the presence of residual stresses. Thus, all the adhesion and toughness experiments presented afterwards should be considered with special attention in their interpretation. The same experiment should be used to compare the effect of the different spray parameters on coating adhesion and toughness. Moreover, the results obtained under the same spray conditions with two different measurements devices are not comparable.

17.6.6 Bending Toughness Measurements

“Bending tests” are carried out by either three-point measurements where a rectangular coupon is placed on two rolls and a third roll applies a load at the mid-span location as in Fig. 17.24a from [Rammo NN, et al. (2009)] or four-point measurements where four rolls are used to more homogeneously distribute stresses over the test volume, as in Fig. 17.24b from [Lin CK, Berndt CC (1994)]. During the three-point test, the upper half of the specimen is under compression, while the complementary half is under tension. With the four-point bend test, it is the reverse. This test is more currently used because it is less sensitive to the defects within coatings. However, it is a mixed mode system with ϕ comprised between 35 and 60°. The test must enable a symmetric crack to propagate from a perpendicular notch, see Fig. 17.24b, along the weakest interface of a multilayer specimen.

In principle, stable crack propagation should occur at a constant load between the two inner loading points. Théry P-Y et al. (2007) performed adhesion tests on specimens, either pre-cracked, as shown in Fig. 17.25a or not. Without preset pre-crack, a large load is needed to initiate the crack and the specimen could consequently be overloaded so that catastrophic crack propagation occurs, and the force–displacement diagram exhibited no plateau (see Fig. 17.25b), providing no reliable information on the adhesion energy. A pre-crack has been successfully realized by introducing a

1-mm large band at the center of the specimens that were not grit blasted prior to spraying [Théry P-Y et al. (2007)]. Under these conditions, a stable crack propagation occurs, with the force–displacement diagram exhibiting a plateau after the peak (see Fig. 17.25c) providing reliable adhesion measurements. The length of the pre-crack might be sufficient to make the critical strain energy release rate, G_{ic} , be independent of it [Clyne TW, Gill SC (1996)].

AE is often used to follow crack propagation [Ma XQ, Cho S, Takemoto M (2001b)]. The distribution of AE responses combined with the analysis of crack source parameters is useful for determining the failure modes and the damage progression [Ma XQ, Cho S, Takemoto M (2001b)].

This method can also be used to determine the coating toughness. For that the critical strain energy release rate G_{ic} (see Eq. 17.19) must be calculated either from simple equilibrium equation, assuming an elastic behavior, or using more complex expressions such as those deduced from Euler–Bernoulli beam theory [Bradai MA, et al. (2008), Li H, Khor KA, Cheanga P (2002)]. In order to determine G_{ic} , both the applied load and the displacement of the loading points are continuously monitored and recorded. The specimen is loaded until both cracks have propagated out to the supporting points. The strain is monitored, and any cracking detected by AE so that the strain to fracture (STF) is determined. Unfortunately, the STF parameter is dependent on the residual stress. For example, Howard and Clyne, as cited by

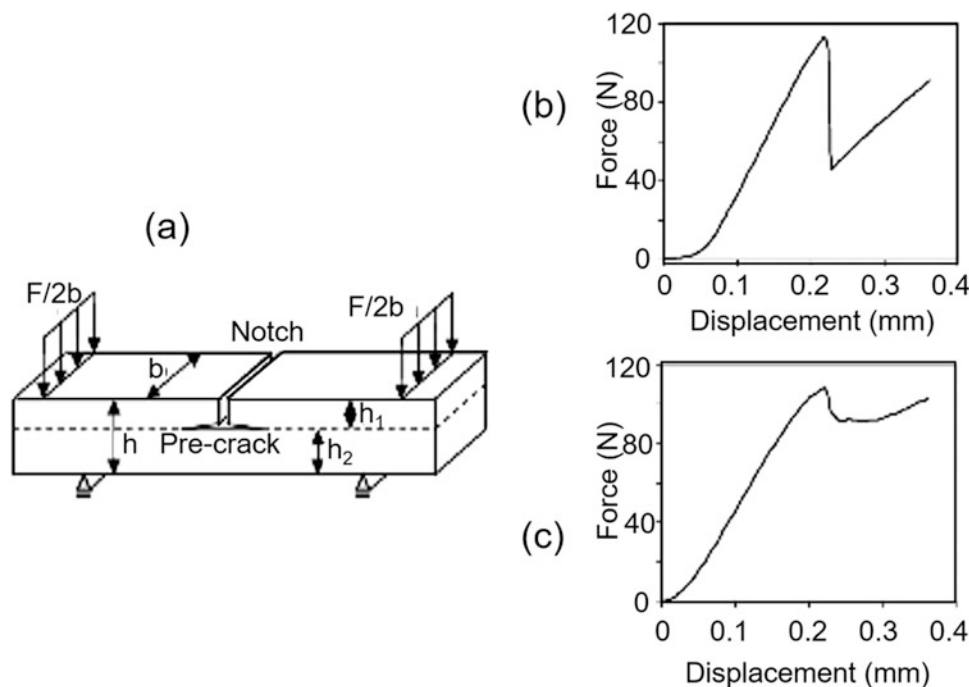


Fig. 17.25 (a) Four-point bending specimen with symmetrical interfacial cracks; (b) force–displacement diagrams recorded during the adhesion test, without any pre-crack; and (c) with an efficient pre-crack [Théry P-Y et al. (2007)]. (Reprinted with kind permission from Elsevier)

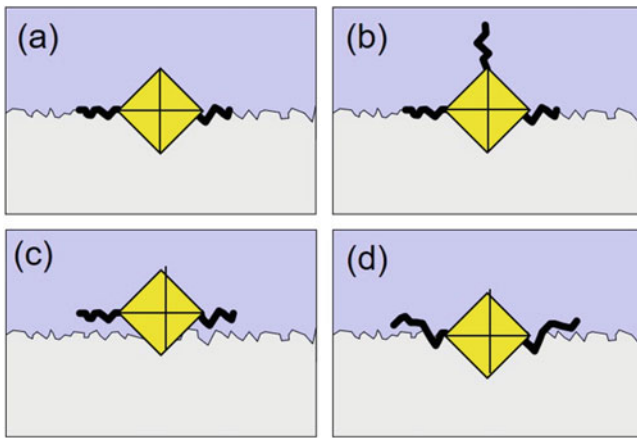


Fig. 17.26 Schematic aspect of the crack generated by interfacial indentation: (a) accepted test, (b) multiple cracks, (c) misalignment, and (d) deviated cracks [Montavon G (2004)]. (Reprinted with kind permission of Prof. G. Montavon)

Lin CK and CC Berndt (1994), used the bi-material notched four-point bending specimen to study the interfacial fracture toughness of vacuum plasma-sprayed titanium coatings. G_{ic} was $6.79 \pm 0.35 \text{ J/m}^2$ for coatings exhibiting residual stress and $2.98 \pm 0.19 \text{ J/m}^2$ for coatings without residual stress.

The four-point test has been used to characterize, for example, plasma-sprayed TBCs [Choi SR, et al. (2005)], 100Cr6 steel coatings thermally sprayed on a 35CrMo4 steel substrate [Bradai MA, et al. (2008)], plasma-sprayed ceramics [Westergård R, et al.(2000)], high velocity oxy-fuel-sprayed bioceramic coatings [Li H, Khor KA, Cheanga P (2002)], and detonation-sprayed MoB–CoCr alloy coatings on 2Cr13 stainless steel substrate [Heping L, et al. (2010)].

17.6.7 Indentation Toughness Measurement

Compared to the sophisticated adhesion and/or toughness measurements described above, the indentation test is simple as it consists essentially in obtaining polished cross-sections of coating and substrate and performing Vickers hardness (VH) indentation tests on the interface using different applied loads. Upon indenting the interface, a plastic deformation zone is created by sharing the combined local properties of the coating and the substrate. When the fracture toughness of this composite interface material coating is reached, a local crack occurs [Westergård R, et al. (2000), Heping L, et al. (2010)] (see Fig. 17.26a) [Montavon G (2004)]. The purpose of the interface indentation test is to give a quantitative measure of the apparent fracture toughness of the above mentioned “interface material.” Compared to most of the above tests, it does not require the use of a bonder and it may be used for a large range of coating thicknesses, provided they are over $100 \mu\text{m}$. However, the test needs to

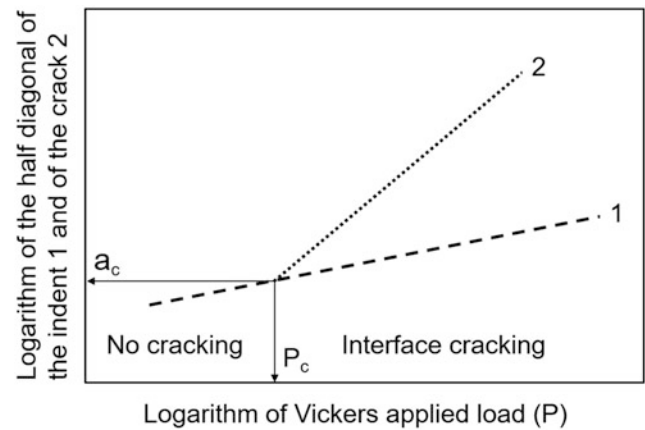


Fig. 17.27 Typical results obtained by performing the interface indentation test: curve 1: logarithm of Vickers hardness indent half diagonal length and curve 2: logarithm of the interface crack length. Below P_c and a_c no interface cracking is observed [Lesage J, et al. (2000)]. (Reprinted with kind permission from Elsevier)

be carefully performed and avoid multiple cracks (Fig. 17.26b), misalignment (Fig. 17.26c), and cracks deviation (Fig. 17.26d).

Lesage J. et al. (2000) have developed a procedure for coated materials; it consists of the following:

- Applying the Vickers indent with its diagonal coincident with the coating substrate interface.
- For each indentation test, measuring the value of the half diagonal of the indent, a_c , and the length of the crack l , both at the interface.
- Plotting these data as a function of the applied load in bi-logarithmic scale, as represented schematically in Fig. 17.27.
- Determining the coordinates of the critical point indicated in Fig. 17.27 (load P_c , half diagonal of crack length a_c), underneath which no crack is formed.

To achieve a quantitative measure of the apparent fracture toughness, the mechanical properties, strength, and elasticity of the interface materials must be known. Neglecting the effect of residual stresses, according to Lesage J, et al. (2000) the apparent interface fracture toughness K_{ca} may be defined as

$$K_{ca} = 0.015 \frac{P_c}{a_c^{3/2}} \left(\frac{E'}{H} \right)_i^{1/2} \quad (17.23)$$

The quantity $(E/H)_i$ may be expressed as follows:

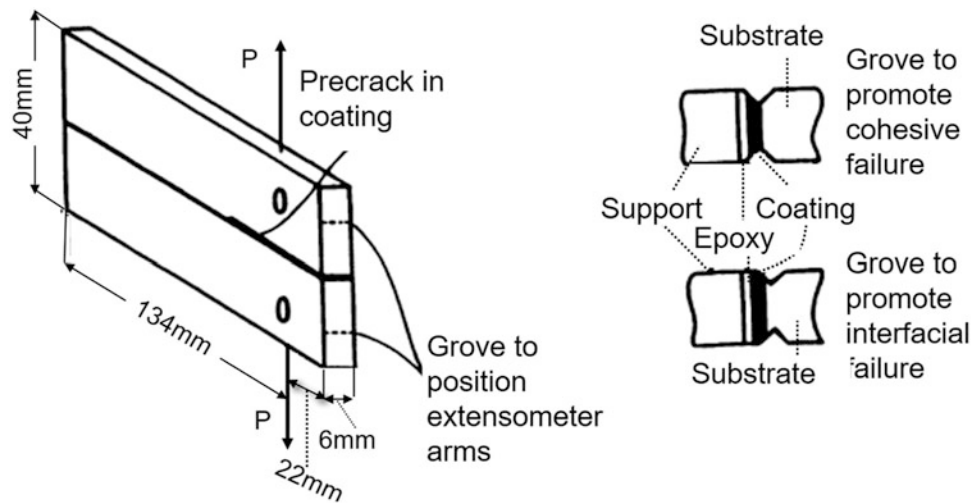


Fig. 17.28 Double cantilever beam specimens used for adhesion measurement. Detail shows the grooving procedure to promote either interfacial or cohesive failure [Lin CK, Berndt CC (1994)]. (Reprinted with kind permission from Springer Science Business Media, copyright © ASM International)

$$\left(\frac{E'}{H}\right)_i^{1/2} = \left[\frac{\left(\frac{E'}{H}\right)_s^{1/2}}{1 + \left(\frac{H_s}{H_c}\right)^{1/2}} + \frac{\left(\frac{E'}{H}\right)_c^{1/2}}{1 + \left(\frac{H_c}{H_s}\right)^{1/2}} \right] \quad (17.24)$$

where H is the Vickers hardness and E' the Young's modulus. The subscripts i , S , and C stand for interface, substrate, and coating, respectively.

This method was used, for example, to characterize the effect of thermal treatment on the adhesion of thermal-sprayed NiCr coatings [Lesage J, et al. (2000)], the adhesion of plasma-sprayed cermet $\text{Cr}_3\text{C}_2/\text{Ni}-\text{Cr}$ coatings [Hivart P, Crampon J (2007), Marcano Z, et al. (2008)], and that of NiCr- Cr_3C_2 VPS-sprayed coatings [Marot G, et al. (2008)].

17.6.8 Other Methods

17.6.8.1 Double Cantilever Beam Test

In the simple double cantilever beam (DCB) test on coatings (Fig. 17.28), a tension force is applied to the specimen assembly and displacement is measured by an extensometer placed on the arms [Lin CK, Berndt CC (1994)]. When cracking initiates (decreasing load with increasing extension), the DCB is unloaded. Several loading/unloading sequences are performed until the specimen completely fails, at which point the morphology can be examined by optical microscopy and SEM. Of course, the fracture toughness of the adhesive must be greater than that of the coating. As illustrated in Fig. 17.28, it is possible to promote either cohesive or interfacial failure. In this test, both fracture modes occur and the ϕ angle is between 0° and 50° .

Expression of the fracture toughness can be found in the paper of Lin CK, Berndt CC (1994).

17.6.8.2 Double Torsion Test

The double torsion test [Lin CK, Berndt CC (1994)] has been applied to thermally sprayed coatings. The prime advantage of this test is that the crack length need not be measured, because cracking occurs at a constant strain energy release rate or stress-intensity factor.

17.6.8.3 Scratch Test

The scratch test is mostly used to characterize thin, hard coatings (for example, TiN and TiC). In this test, a loaded Rockwell C diamond stylus (see Sect. 17.7.1.1) is drawn across the coating surface under either constant or gradually increasing load. Often the AE is also monitored during the scratching procedure to determine precisely the critical load, P_c , at which failure takes place [Lin CK, Berndt CC (1994)]. Erickson LC et al. (1998) have compared scratch test with other tests and Xie Y and Hawthorne HM (2001) have modeled it. For example, Ma XQ et al. (2008) have used this technique to characterize ultrafine-structured alloy HVOF sprayed using a liquid suspension/slurry containing small alloy powders. In their test, 0.2 mm tip radius Rockwell diamond indenter tip was drawn across the coating with a loading rate of 300 N/min, start load of 0.9 N, and end load of 150 N. Using optical microscopy examinations, the critical loads were measured. Sundararajan G et al. (2010) used this test to get an estimate of the critical load (P_c) at which cracks started appearing at the base of the scratch formed on the cold-sprayed coating surface. Scratch tests were performed on polished and un-etched top surfaces of Cu, Ag, Zn, and SS 316 L coatings with different heat treatments.

17.6.8.4 Laser Shock

(a) Coating Adhesion

Based on the work of Bolis C et al. (2002), laser adhesion test (LASAT), which is a laser shock method, has been used to characterize the interfacial resistance of thermal-sprayed coatings. The pulsed laser was focused on the substrate side on a few mm² surfaces, permitting to run different tests on the same sample. Irradiating the surface of a substrate with a high-power laser generated a very intense pressure pulse propagating as a shock wave [Barradas S et al. (2005)]. This shock wave propagated and reflected in the material, creating release waves, the crossing of which led to tensile stresses. Depending on the laser source, the shock pressure can reach few tens GPa during a few ns. To determine the adhesion threshold, shocks were applied to samples with different levels of the incident laser power flux. The debonding limit, that is, when exceeding the interface resistance, was determined from systematic metallographic observations of cross-sections of all the laser-shocked specimens. Below and above the laser shock adhesion threshold, two types of velocity profiles of the coating surface were respectively obtained [Barradas S, et al. (2002)].

- The first type of velocity signal was for a laser power flux of 18 GW/cm², that is, below the adhesion threshold. The corresponding curve showed two peaks in the velocity amplitude, which corresponded to the interaction of the shock wave with the coating surface. The time between two peaks was that for the shock wave to propagate through the whole coated substrate material and go back. Therefore, the wave could go through the interface, which was the sign there was no interface damage.
- When increasing the power flux, beyond a certain value the distance between two velocity peaks was shorter and the time between the two peaks corresponded to the time necessary for the wave to cross two times the coating only. This signal was typical of de-bonding at the interface as the shock wave reflects on the void, which was created at the first interaction with the interface.

Barradas S et al. (2005) used an Nd: YAG laser delivering 10-ns Gaussian pulses focused on a 2-mm-diameter spot at the surface of the substrate with a wide range of laser power densities (5–100 GW/cm²). Laser interferometry allowed measuring the substrate top surface velocity to calibrate LASAT testing numerical simulations in order to calculate the corresponding traction at interface. For the first tests, the tensile stresses in the tested sample were determined using “SHYLAC” finite element code, which allowed 1D simulation only. It corresponded to assuming that the laser beam had a top-hat shape and not a Gaussian one. The first experiments [Barradas S et al. (2005)] on cold-sprayed Cu

onto Al showed that Cu–Cu interlamellar strength was about of the same order as that of Cu–Al coating–substrate adhesion and demonstrated the feasibility of the LASAT testing as a powerful tool for the measuring of adhesion, including in local zones. Rolland G et al. (2011) showed that the laser test was reproducible provided that a black overlay was deposited onto the surface prior to testing to achieve a good and constant absorption of the laser pulse. The optimization of the laser test consisted in determining the maximum laser energy without any surface melting. This requirement came from the fact that the laser absorption was not stable as a function of surface temperature and dramatically increased with melting. Rolland G et al. (2011) carried out finite element calculations using Zebulon® in two steps: that is, thermal calculations then mechanical calculations. The thermal step consisted in applying a thermal flow on the laser-irradiated zone. The laser power profile was modeled with a spherical approximation [Jeandin M et al. (2010)] with which the minimum laser energy needed to melt the surface was calculated. This power profile was used to involve the defocusing effect of the laser, which evolved from a top hat profile to a Gaussian profile.

LASAT has been used to evaluate the feasibility of metallization of thermoplastic polyamide 66 (PA66) using cold spray of aluminum powder [Giraud D, et al. (2012)]. The need of careful interpretation of LASAT when applied to this kind of deposits was highlighted. However, the potential of the test was demonstrated and criteria for future use established.

Guipont has studied the characterization with LASAT of porous ceramic coatings (YSZ and HA) plasma sprayed or deposited by a physical process on metal substrates [Guipont V (2013)]. He showed that, when the laser power corresponding to the adhesion level was reached, a white spot appeared in the ceramic coating at the opposite of the laser impact. This signature of the cracked surface that can be detected with eyes is very convenient.

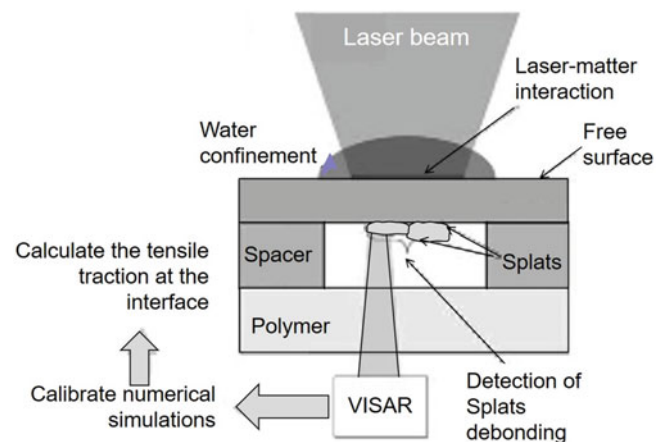


Fig. 17.29 Schematic illustration of LASAT testing setup for splats [Guetta S, et al. (2009)]. (Reprinted with kind permission from Springer Science Business Media, copyright © ASM International)

(b) Splat Adhesion

In cold spray, particle adhesion onto the substrate is influenced by particle impact velocity. Guetta S et al. (2009) developed an original experimental setup (Fig. 17.29) to discriminate the particles as a function of the levels of impact velocity to investigate the influence of this parameter on the resulting splat adhesion. The sample, the top of which surface showed splats, is placed in front of a polymer plane. The upstream laser shock results in the debonding of splats, which are collected at the polymer surface [Guetta S, et al. (2009)]. For splats, laser interferometry (VISAR in Fig. 17.29) resulted in measuring the substrate top surface velocity. This was used to calibrate LASAT testing numerical simulations before the corresponding traction at interface was calculated. Because splat debonding highly depended on traction at the interface, modifying the laser beam intensity decreased the latter. When the traction was low enough, splats no longer debonded. The level of adhesion was therefore reached. Mechanical adhesion resulted from both solid material jetting, which kept the particle in the substrate and molten material jetting, which overlaid the particle and improved adhesion. TEM observation, simulation, and LASAT experiments allowed correlating nanoscale phenomena to macroscopic parameters such as impact velocity [Christoulis DK, et al. (2010)].

17.7 Mechanical Properties

Mechanical properties of materials including hardness, adhesion, Young's modulus, toughness, and residual stress are very important for materials and coatings in service conditions. Some tests of these properties are summarized in [17.M1–17.M4].

17.7.1 Hardness and Indentation Test

17.7.1.1 Hardness

Hardness is generally not considered as an intrinsic property of a material or a coating and its value depends on the testing method used [Chandler H (ed) (2004)] as well as, for coatings, on the direction where the test is performed: at coating surface, orthogonal to splats, or at a cross-section parallel to splats. In the latter case, the coating must be imbedded in resin, which is not necessarily the case for surface measurements. Cross-sections are generally polished, whereas it is not necessarily the case for surfaces. However, on nonpolished rough surfaces, the dispersion of results is more important and thus polishing is recommended. For thin coatings, the substrate may influence the results. It is, however, generally accepted that for coatings thicker than 250 μm the substrate is no more a problem. As previously underlined,

hardness measurements must be statistical and thus can be performed only with multiple readings, at least 10–15.

The principle of the method to measure hardness is the “depth of penetration” (in general for nano-hardness) or the “width of print” (microhardness or hardness) approach left by an indenter applied with a given load, P (between 0.1 mN and tens of N) during a given time (usually a few tens of seconds both for loading and unloading). The load used for nano-hardness measurement, $P < 0.05$ N, microhardness $0.05 < P < 5$ –10 N, and hardness > 10 N.

Wigren J and K Tång (2007) have pointed out that microhardness is generally performed as per ASTM E384 [17.M7]. A first general misconception is the number of indentations. It is easily shown that 10 indentations are by far too few. A second issue is the metallographic preparation of the specimen before measurement. A preparation routine that tends to smear the coating (i.e., the use of SiC paper) can lead to an underestimation of the microhardness by about 100 Vickers.

When measuring the depth of penetration, a motorized vertical carriage supplies a loading force (from 0.1 mN to kN). The depth of indentation is measured for nano-hardness with a 3-plate capacitance sensor (from 0.1 nm to few μm) and for microhardness with a traditional capacitance sensor (from 0.05 to 250 μm).

For microhardness and hardness measurements, the diameter or diagonals (from about 5 μm to 0.5 mm) of the indents are measured with a digital optical microscope. However, here again to read prints that can be only a few micrometers long, the surface preparation also plays a non-negligible role [Riggs W (2004)]. It is also important to keep a certain distance, depending on the indenter of the indenter used, between the measurement location and the interface coating–substrate or bond coat.

A comparison of hardness testers is given in [17.M5]. For coating nano-, microhardness, and hardness measurements, four types of indenters are used:

- **Berkovitch indenter** is used for nano-hardness measurements. It is a three-sided pyramid, which is geometrically self-similar and has an excellent penetration. It has a very flat profile and a tip radius of about 150 nm, a total included angle of 142.3° and a semi-apex angle of 65.03° . The Berkovich tip has the same projected area to depth ratio as Vickers indenter. For example, Dey A et al. (2009) used this method to characterize hydroxyapatite coatings. It is also possible to use a cone of semi apical angle 30° , which penetration depth is higher than that of the Berkovich indenter.
- **Vickers indenter**. This standard indenter uses a square-based diamond pyramid with an angle between opposite faces of 136° (see Fig. 17.30). Sometimes, this test is called diamond pyramid hardness (DPH). The hardness is calculated by

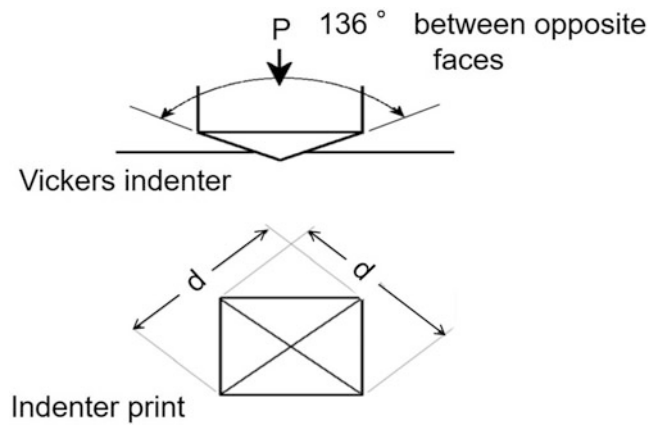


Fig. 17.30 Schematic of a Vickers indenter tip and of its print on the tested coating

$$HV = \frac{2P \sin \alpha}{L^2} \text{ (MPa)} \quad (17.25)$$

where P is the applied load (N), L is the average length of diagonals (m), and α is the angle between opposite faces of diamond (136°). The measurement is acceptable only if the length difference between both diagonals (see Fig. 17.30 representing the indenter print) is less than 5% and if the print is at least half a diagonal length apart from any side of the coating and for measurements on cross-sections if the distance from interface or top is larger than 1.5 times the diagonal length.

In principle, because the impressions made by the pyramid indenter are geometrically similar whatever their size, HV should be independent of the load. However, localized microstructural variations decrease when the applied load increases. This is due to the particular structure of the sprayed coatings that involve splats more or less in good contacts, voids, unmolten particles, the indenter with a higher load being in contact with more splats, voids, and giving a response less and less localized. Thus, when the load increases, the dispersion of results diminishes. If curves representing the minimum and maximum values measured for different loads are plotted, they would look as those schematically presented in Fig. 17.31.

It should be stressed that when hardness measurement is presented it is meaningless unless the load at which measurement has been made is given as well as the measurement dispersion: for example, $600 \pm 60 \text{ MPa HV}_5$. This is illustrated in Fig. 17.32 for titania (TiO_2) coatings HVOF sprayed on low-carbon steel substrates using a DJ 2700 HVOF torch by [Lima RS, Marple BR (2003)]. Hardness measurements on the surface and cross-section of the titania

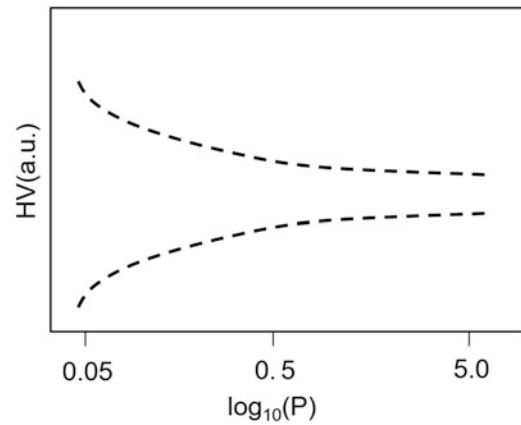


Fig. 17.31 Schematic variation of distributions of maximum and minimum of the Vickers hardness of a thermal sprayed coating for different loads

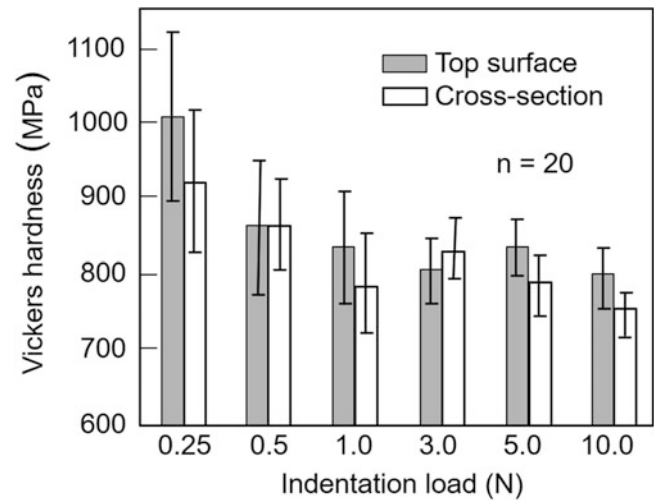


Fig. 17.32 Vickers hardness on the top surface and cross section of HVOF titania coatings for different indentation loads [Lima RS, Kucuk A, Berndt CC (2002)]. (Reprinted with kind permission from Springer Science Business, copyright © ASM International)

coating are noted to decreased from <900 to 1000 Vickers at an indentation load of 0.25 N, to <750–800 Vickers with the increase of the indentation load to 10 N, for both the top surface and cross-section. At lower loads, the indentation diagonal sizes were quite small indicating that only a small region of the coating was being sampled. For example, at an indentation load of 0.25 N, the indentation diagonal length was approximately $7 \mu\text{m}$. This minimized the extent of defects, such as coarse pores, splat boundaries, and micro-cracking, enclosed within the indentation zone. As the indentation load increased, so will the volume of coating be being analyzed. At an indentation load of 10 N, the indentation diagonal length was approximately $50 \mu\text{m}$. As a consequence, porosity, splat boundaries, and micro-cracking played a significant role on hardness, lowering its value. As

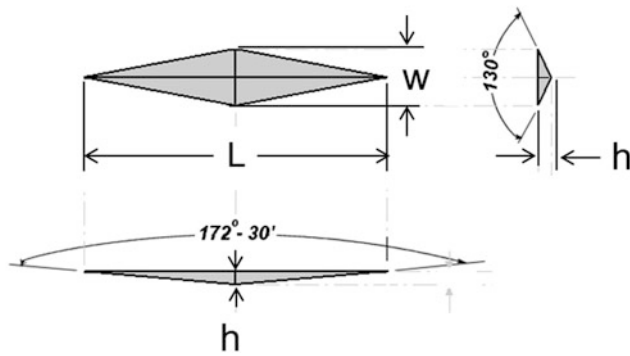


Fig. 17.33 Knoop hardness prints

mentioned earlier, the dispersion of the hardness values decreased with the increase of the indentation load. Hardness measurements made on the cross section of the coating were generally lower than those made on the surface for the coating for the same indentation load [Lima RS, Marple BR (2003)].

For very brittle materials, where only a small indentation may be made for testing purposes, Knoop indenter is often used. The geometry of this indenter is an extended pyramid with a length to width ratio of 7:1 and with face angles of $72^{\circ}30'$ for the long edge and 130° for the short edge, respectively (see Fig. 17.33). The depth of the indentation can be approximated as $1/30$ of the long dimension. The Knoop hardness HK or KHN is then given by the formula:

$$HK = \frac{P}{c_f L^2} \text{ (MPa)} \quad (17.26)$$

where L is the length of indentation along its long axis and, c_f correction factor related to the shape of the indenter, ideally 0.070279. For measurements close to the interface or the top for coatings cross-sections, the distance must be higher than 0.35 times the length of the longer diagonal. Often Knoop is preferred to measure hardness of ceramic materials because of the longer print of the long diagonal compared to that of the Vickers indenter under the same load. For example, Lima RS, et al. (2002) have measured the Knoop hardness of plasma-sprayed nanostructured partially stabilized zirconia coatings. ASTM tests for Knoop and Vickers harnesses are given in [17.M6–17.M9].

Rockwell C indenter is a diamond cone with an angle of 120° . The test consists in measuring the additional depth to which an indenter is forced by a heavy load beyond the depth of a previously applied light load. The light load eliminates backlash in the load train: the indenter breaks through slight surface roughness and crush particles of foreign matter [Chandler H (ed) (2004)]. Compared to the two previous

techniques, Rockwell C technique is faster due to its minimal surface preparation and its ease of use.

17.7.1.2 Indentation

Upon penetration of the indenter into the material, under a load, P , elastic and plastic deformation phenomena occur resulting in a print which is linked to the indenter geometry and the applied load. For example, a spherical indenter with low loads results generally in elastic deformation, while a sharp indenters gives rise to plastic deformation even with very low loads. The penetration depth, h , depends on the geometry of the indenter and the load. The curve $P(h)$ shown in Fig. 17.34a is obtained by first increasing progressively the load (loading step) and then by reducing it to zero (unloading step). When the maximum load, P_{\max} , is reached the maximum depth, h_{\max} , is obtained. The unloading curve is different from the loading one (see Fig. 17.34a) because of the plastic deformation induced by the load. Figure 17.34b illustrates the different states induced by the loading and unloading steps. The depth h_{\max} results from the sum of the contact depth h_p and displacement of the material surface along the contact perimeter as shown in Fig. 17.34c and d for a rounded-cone [Bucaille JL, et al. (2002)] and a sharp-cone indenter. Once the indenter is removed, only the elastic component is recovered, leaving a residual deformation h_r (see Fig. 17.34d). It is worth noting that the length of the Vickers indenter diagonal, observed after unloading, is that corresponding to the residual deformation. This is different for the Knoop print: upon unloading elastic deformation reduces the length of the shorter diagonal as well as its depth, while the elastic recovery of the longer diagonal is much less. It gives the possibility to determine the Young's modulus [Marshall DB, et al. (1982)].

Instrumented indentation method reveals much more information about a thermal spray coating than conventional Vickers or Knoop microhardness methods. It gives information about mechanical properties of the coating such as elastic modulus, elastic/plastic work of indentation, and creep or cyclic behavior [CSM Instruments (2010)]. Thanks to its force–displacement recording capability, the instrumented indentation method is able to sense when an indentation is performed on a void: the depth suddenly increases without the corresponding increase in force (Fig. 17.35). The most significant advantage is probably the automation of measurements. For example, this efficient cyclic indentation method allows automatic increase of maximum load on each subsequent cycle. Dataset of indentation depth and hardness or elastic modulus is obtained within 10 or 20 min depending on the number of cycles [CSM Instruments (2010)]. When the coating hardness increases, the loading and unloading curves are shifted to the left as the indenter penetrates less for the same load.

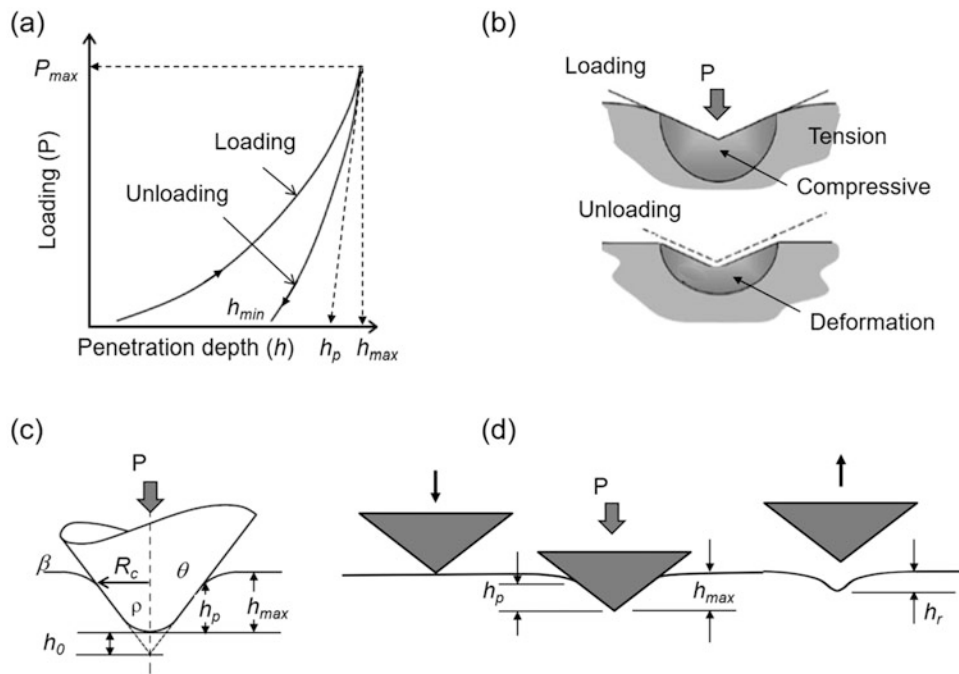


Fig. 17.34 (a) Characteristic curves $P(h)$ during loading and unloading, P being the load, and h the indenter penetration depth, (b) different states induced by loading and unloading steps, and (c) geometrical parameters for a rounded cone indenter under load and (d) definitions of h_{max} , h_p and h_r [Bucaille JL, et al. (2002)]. (Reprinted with kind permission from Springer Science Business Media)

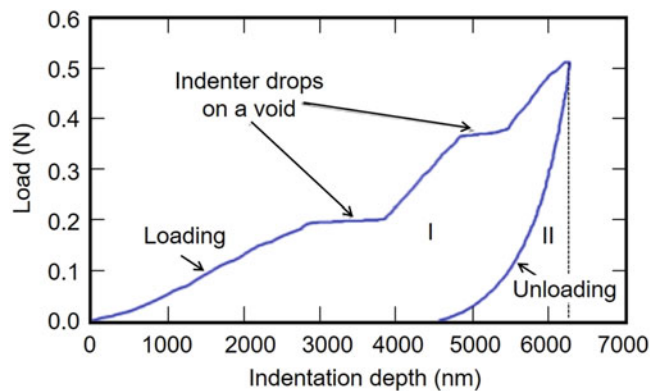


Fig. 17.35 Loading–unloading indentation curve presenting two “indenter drops” due to indentation on voids or other defects, Areas I and II represent respectively plastic deformation and elastic recovery [CSM Instruments (2010)]. (Reprinted with kind permission of CSM Instruments application bulletin)

The area between the loading and unloading curve represents the energy dissipated in the coating due to plastic deformation, and the area under the unloading curve represents the elastic energy for deformation. The normal load, P , and the depth of indentation, h , are measured during the indenter penetration [CSM Instruments (2010)]. The zero-point, defined as $P = 0$ and $h = 0$, is determined by a change in the force signal as the indenter approaches the test

surface. When the indenter is withdrawn the hardness, H can be calculated for the conical indenter by

$$H = \frac{P}{\pi R_c^2} \text{ (MPa)} \quad (17.27)$$

The hardness can also be calculated from the depth of the indenter, h_p in Fig. 17.36 (plastic component of the coating deformation only) or from h_{max} (corresponding to both plastic and elastic components) defining the Universal Hardness, HU [Musil J, et al. (2002)], which is lower than H . For example, with a Vickers indenter one has Leigh S-H, Berndt CC (1999):

$$H = \frac{L_{max}}{(26.43 h_p)^2} \quad \text{and} \quad HU = \frac{L_{max}}{(26.43 h_{max})^2} \quad (17.28)$$

Musil J et al. (2002) have shown that the area between the loading/unloading curve and the value of, h decrease with increasing hardness H , effective Young’s modulus $E^* = E' / (1 - \nu^2)$ and universal hardness HU, where E' and ν are the Young’s modulus and the Poisson ratio, respectively. While there is no simple relation between the mechanical response of the coating and H or E alone, this response is strongly dependent on the ratio H/E . More details will be given about indentation in sections related to Young’s modulus and toughness measurements.

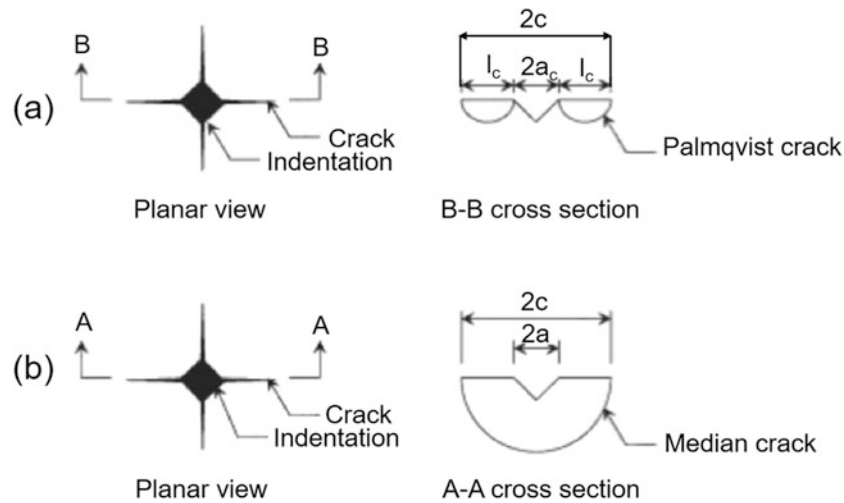


Fig. 17.36 Planar and cross-sectional views of (a) the Palmqvist model and (b) median crack model [Meacham BE, et al. (2006)]. (Reprinted with kind permission from Elsevier)

17.7.2 Young's Modulus

The elastic constants of thermal spray coatings are strongly dependent on microstructures (depending upon the real contacts between layered splats, cracks, and porosities), which are sensitive to the material processing condition. For example, Leigh S-H, Berndt CC (1999) assumed that the voids within the deposit were ellipsoidal in shape. The structure of the deposit was considered to be transversely isotropic with respect to the spray direction, which required five independent elastic constants of a stiffness tensor. Solid mechanics models containing ellipsoid-shaped voids were applied to obtain the five independent elastic constants of the deposits. The calculated elastic constants were compared to the experimentally determined values. The predicted Young's modulus values from the theoretical calculations were comparable to the experimental values. However, the thin voids and micro-cracks contributed only to a small part of the total porosity; but they had the major influence on the decrease of Young's moduli by small elastic openings and partial closings of their faces. The inter-splat thin voids led to the decrease of Young's module E_3 in the spraying direction, while the intra-splat micro cracks led to the decrease of Young's module E' in the directions orthogonal to the spray direction [Landa M, et al. (2003)]. A few ASTM tests for Young's modulus are given in 17.M10–17.M13. Experimental values of the Young's modulus can be obtained from the following measurements:

17.7.2.1 Indentation

As already pointed out in Sect. 17.7.1.2, the loading/unloading curves of Berkovitch or conical indenters are related to the ratio H/E and different ways are used to determine the Young's modulus. Roy M et al. (2006) working

with a Berkovitch indenter have used the following expression

$$\frac{1}{E_r} = \frac{(1 - \nu^2)}{E'} + \frac{(1 - \nu_i^2)}{E'_i} \quad (17.29)$$

with

$$E_r = \frac{0.89 \times S}{\sqrt{A}}$$

where S is the slope of the initial part of the unloading curve (see Fig. 17.34a), A is the contact area between the indenter and the substrate, E' and E'_i are the Young's modulus, and ν and ν_i are the Poisson ratio of the coating and the indenter, respectively.

Ma D et al. (2009) have used the same approach to investigate a set of approximate relationships between H/E' and W_e/W for different types of Berkovitch tip geometries with different degree of bluntness. W_e and W are the elastic work and total work corresponding to the areas under the unloading and loading curves recorded in an indentation test.

Feng C, Kang BS (2006) (2008) have used a spherical transparent indenter that can directly measure the indentation-induced out-of-plane deformation as well as the indented surface. Coupling with a multiple partial unloading testing procedure, material's Young's modulus was determined.

Wallace JS, Ilavsky J (1998) have used a spherical indenter to measure the elastic constant: Hertzian indentation. They found that planar defects, which contributed only insignificantly to the porosity of the material, had a very strong effect on the elastic modulus. It has been further

shown that there are periodic variations in the elastic modulus throughout the thickness that are correlated with the spray parameters of the initial deposit.

17.7.2.2 Four-Points Bending

The setup used for the four-point bending test is that presented in Fig. 17.24b with the coating placed in tension. All the expressions (see, for example, [Wallace JS, Ilavsky J (1998), Kucuk A, et al. (2000a), Beghini M, et al. (2001a, b) and Podrezov YN, et al. (1999)]) relate the coating Young's modulus, E'_c , to that of the substrate, E'_s , the respective thicknesses of substrate and coating, the relative beam deformation.

Musalek R, et al. (2010) have used different types of loadings: loading up to stepwise increasing loads, with full unloading, loading up to the maximum load, with full unloading, and loading up to stepwise increasing loads, with partial unloading. This allowed observing the coating behavior at different load levels and hysteresis of the stress-strain curves. Coating secant modulus was separated from the total stiffness [Harok V, Neufuss K (2001)]. Bare substrates were tested to assess their elastic limits. The maximum load applied was then selected accordingly.

17.7.2.3 Knoop Hardness

The elastic modulus of coatings can be determined via Knoop microhardness tests. As already emphasized, the elastic modulus is determined by measuring the major and minor diagonals of a Knoop indenter, respectively [Lima RS, et al. (2001a, b)].

17.7.2.4 Ultrasound Propagation

Landa M, et al. (2003) have studied the dependence of the velocity of the longitudinal ultrasound waves on uniaxial pressure for three types of plasma-sprayed ceramics in two directions. The measurement consisted in recording the AE activity (count rate dN/dt) as AE is an important tool for detecting the irreversible changes in brittle materials. The Young's modulus determination requires the knowledge of the coating thickness, including during the pressure application. Acoustic emission was monitored to find the maximum pressure, which did not cause any detectable damage. The instantaneous elastic stiffness c_{33} and c_{11} , calculated from the measured ultrasound velocities, grew with increasing pressure between 0 and 300 MPa in different materials and in different directions 1.4 up to 4.7 times [Landa M, et al. (2003)]. These results were explained by elastic closing of the inter-splat thin voids and intra-splat micro cracks under pressure. The loading and unloading curves slightly differed, which was explained by relative displacements of the faces of thin voids and micro-cracks oblique to the compression axes, leading to the appearance of friction forces.

17.7.3 Toughness

Among the different mechanical methods that can be used to measure coating toughness, the Palmqvist fracture toughness is popular because no specialized test specimens are necessary and small laboratory samples can be easily tested. Depending on the load applied on a Vickers indenter [Meacham BE, et al. (2006)], either Palmqvist cracks appear for a low load regime, while median cracks show up for high load regime. When increasing loads, Palmqvist cracks form first followed by median cracks. Both types of cracks are represented in Fig. 17.36 from Meacham BE, et al. (2006). Unlike the median crack model, also called halfpenny model, Palmqvist cracks tend to be only as deep as the indenter penetration and are independent of each other.

The critical indentation and crack-related dimensions are the indentation half-diagonal length, a_c , the radial surface crack length, c , and the Palmqvist surface crack length, l_c (Fig. 17.37) [Emiliani ML (1993)]. Equations to determine fracture toughness take the following general form for half-penny (Eq. 17.30) and Palmqvist (Eq. 17.31) shaped cracks [Emiliani ML (1993)].

$$K_c = k \frac{P}{a_c c^{1/2}} \quad (17.30)$$

$$K_c = k(E/HV)^{2/5} \frac{P}{a_c l_c^{1/2}} \quad (17.31)$$

where according to [Emiliani ML (1993)], k is a constant determined typically between 0.001 and 0.5, P is the applied indenter load (N), HV is the Vickers microhardness (GPa), E is the elastic modulus (GPa), and a_c , c , l_c are the indentation and crack-related dimensions (m) respectively that of indenter a and that of Palmqvist, as shown in Fig. 17.36. However, it must be kept in mind that cracks must have a minimum length, depending on the test used. The AE recorded during macro-indentation shows three distinct stages [Emiliani ML (1993)]. The onset of the second stage marked the critical indentation size, for the specific-analyzed coating where radial cracks begin to form. The last stage was associated with the continuation of all mechanisms of accommodation as the indenter descends further into the coating, and therefore changes significantly with load [Faisal NH, et al. (2009)].

Vickers indentation with Palmqvist cracks is extensively used for ceramic coatings, see, for example, [Xie XY, et al. (2010), Richard CS, et al. (1995) and Berka L, Murafa N (2004)]; cermet coatings, see, for example, [Faisal NH, et al. (2009), Lima MM, et al. (2003a, b) (2004), Chivavibul P, et al. (2010) and Prudenziati M, et al. (2010)]. It is also used for certain metal coatings as, for example, those manufactured by PTA with gas-atomized powder and wire

arc with cored wire, both with a nominal composition of <25% Cr, <5% Mn, <10% Mo, <10% W, <5% B, <5% C, and < 5% Si, the balance being Fe [Meacham BE, et al. (2006)]. A few ASTM standards for toughness measurements are presented in [17.M14–17.M19].

17.7.4 Residual Stress

The paper of Clyne TW, Gill SC (1996) presents an overview of residual stresses associated with thermally sprayed coatings together with the corresponding measurements.

17.7.4.1 X-Ray Diffraction

A very popular method for direct measurement of residual stresses is the monitoring of the shift of selected XRD peaks [Bunker G (2010), 17.M20]. The method is applicable only to materials with well-defined crystal structures. It becomes difficult, as a result of peak broadening, when the grain size is very fine or if unpredictable variations in composition are likely to occur. The lattice strain is obtained from the shift of hkl peak (where h , k , and l stand for Miller indices of the investigated lattice plane), when compared with that for a corresponding unstrained specimen. The drawbacks of the method are the following:

- The limited penetration depth (10–50 μm) of X-rays through most coating materials depending on the source wavelength and coating material.

- The penetration depth is usually about that of the surface roughness of as-sprayed coatings.

To overcome the penetration problem, successive layer-removal can be performed but it changes the stress distribution, if not inducing deformation or damage in the underlying material [Clyne TW, Gill SC (1996)].

Although the lattice strain, and hence stress, in a selected in-plane (x) direction can in principle be estimated via the Bragg's equation from a single measurement, it is more accurate to examine the variation in peak shift as a function of φ , the angle between the normal to the coating surface (y direction) and the normal to the diffracting planes (which lies in the x - y plane) [Clyne TW, Gill SC (1996)]. The stress can then be obtained from

$$\sigma_x = \left(\frac{E}{1 + \nu} \right)_{hkl} \frac{1}{d_0} \left(\frac{\partial d}{\partial \sin^2 \varphi} \right) \quad (17.32)$$

where d is the measured inter-planar spacing and d_0 is the value for an unstrained sample. The Young's modulus, E , and Poisson's ratio, ν , for the hkl planes must be accurately known. In general, they are obtained by experimental measurements, using a sample with a known stress state [Ma XQ, et al. (2001a, b)]. As shown in Fig. 17.37, the lattice strain is obtained from the shift of one hkl peak, when compared with that for a corresponding unstrained specimen.

For coatings with different components such as, for example, WC–Co coating, the diffraction peaks of the dominant

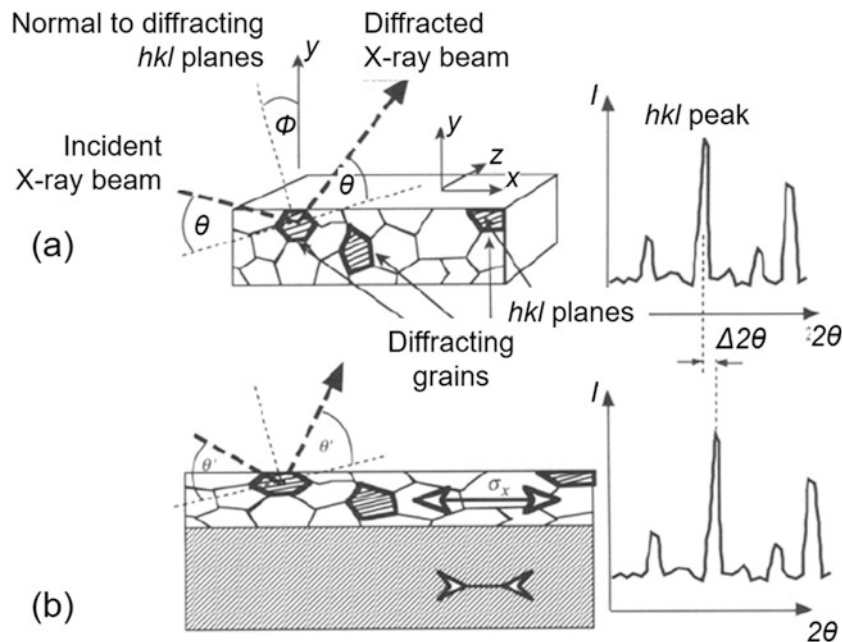


Fig. 17.37 Scheme of the XRD technique for the measurement of residual stresses (a) coating detached from its substrate (un-strained specimen) and (b) coating with its substrate (strained specimen) [Clyne TW, Gill SC (1996)]. (Reprinted with kind permission from Springer Science Business Media, copyright © ASM International)

phase are used [Santana YY et al. (2008), Taha-al ZY, et al. (2009)].

17.7.4.2 Neutron Diffraction

Compared to low-energy X-rays, the main advantage of working with neutrons is the possibility to analyze greater depths, that is, higher coating thicknesses. Neutrons have the following advantage over X-ray photons: for wavelengths comparable to the atomic spacing, their penetration into engineering materials is in the range of several millimeters, due to their interaction only with nuclei instead of electrons [17.M21].

For example, Lyphout C et al. (2008) used a monochromatic neutron beam of a cross-section of $0.6 \times 0.6 \text{ mm}^2$, in a spatially resolved mode, to determine the residual stress distribution within HVOF-sprayed Inconel 718 Coatings. The Bragg's peaks (220) and (111) for Ni-alloy were measured to $2\theta = 86^\circ$ and 47° , using a wavelength, λ , of 0.147 and 0.165 nm, respectively. From the obtained diffracted peaks, they used Bragg's law (Eq. 17.4) with the corresponding lattice strain (Eq. 17.30) defined as a function of the "stress-free" lattice parameter d_0 .

$$\varepsilon_{hkl} = \frac{(d_{hkl} - d_0)}{d_0} \quad (17.33)$$

where d_{hkl} is the lattice spacing and ε_{hkl} is the lattice strain. Measurements were performed only in radial and axial directions, by scanning the sample from the top to the bottom, using, respectively, the reflection and transmission modes. Sampath S et al. (2004) have also used neutrons to measure the residual stress distribution within Ni-5 wt.% Al bond coats sprayed by different spray techniques.

17.7.4.3 Material Removal

There are two basic methods involving material removal: either a hole is drilled in the specimen or layers are removed by polishing.

(a) Layer Removal Method

This method was adapted to coatings by Greving DJ et al. (1994a, b); it is based on the concept that removing a layer from the surface of a plate or beam with residual stresses releases a force and moment acting on the remaining piece. It is presumed that the remaining piece is large enough and the layer removed small enough so that the change in strain through the thickness of the remaining piece is linear. A strain rosette (gage) on the remaining piece records the change in strain on the surface opposite the face where the layer was removed. The stresses in the layer removed and the change in stresses of the remaining piece can be calculated from force and moment equilibrium, the linear strain change assumption, the strain rosette readings, and the stress-strain

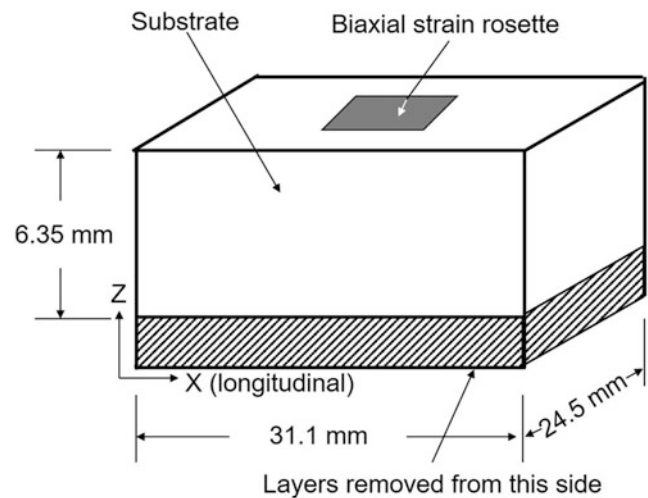


Fig. 17.38 Residual stress specimen ready for layer removal [Greving DJ et al. (1994b)]. (Reprinted with kind permission from Springer Science Business Media, copyright © ASM International)

properties of the material [Greving DJ et al. (1994a, b)]. To calculate the residual stress after removal of one layer, one must know the substrate dimensions, the coating thickness before starting removal, its new thickness after removal, the substrate and coating, Young's modulus, and Poisson ratios. A typical specimen for layer removal is presented in Fig. 17.38. The method was tested for different metal, cermet, or ceramic coatings plasma or HVOF sprayed, with and without bond-coats and with substrate grit blasting [Greving DJ et al. (1994a, b), Pejryd L, et al. (1995), Lima CRC, et al. (2006)].

(b) Hole Drilling Method

The hole drilling strain gage technique [Rendler NJ, Vigness I (1966), Richard CS, et al. (1996) and Schajer GS (1988)] is a semi-destructive method for the determination of residual stresses in the superficial layers of a solid body. The technique simply involves the removal of stressed material by drilling a small hole (about 2–4 mm diameter) on the surface of the body followed by measurement of the relaxation strains occurring around the hole by means of an extensimetric rosette [Valente T, et al. (2005)]. Residual stresses are then calculated from the measured deformations by means of an analytical model based on the solution of the problem of the loaded wide plate with hole [Rendler NJ, Vigness I (1966), Richard CS, et al. (1996) and Schajer GS (1988), Valente T, et al. (2005)].

In the case of nonuniform through thickness stresses, the test must be divided into several small depth increments, and the produced relaxation must be determined for every single incremental step [Valente T, et al. (2005)]. Results may be affected by various errors [Schajer GS, Altus E (1996)] such as alignment [Wang H-P (1979)]. The drilling in brittle

ceramics with diamond drills requires an adapted cooling [Balykov AV (2006)].

17.7.4.4 Bending

A rather powerful and nondestructive residual stress measurement technique is the in-situ curvature method, where the curvature of a thin plate sample is continuously monitored during the deposition process [Clyne TW, Gill SC (1996), Kuroda S, et al. (1988) (2001), Gill SC, Clyne TW (1994)]. Kuroda S, et al. (1988) were the first to describe such a continuous measurement procedure during thermal spraying. They used lightly contacting knife-edges and recorded the changing curvature during spraying. Later, Bolelli G et al. (2008) used this method to determine the peening action and residual stresses in HVOF spraying of 316 L. Gill SC, Clyne TW (1994) then further developed this technique and made two advances.

- First, a noncontacting method of curvature measurement was employed with simple video recording, eliminating interference with free bending of the specimen, and allowing the study of a wide range of substrate temperatures.
- Second, a numerical model was developed that allowed the curvature history to be predicted from thermomechanical boundary conditions and material property including the quenching stress [Clyne TW, Gill SC (1996)].

The main advantage of this technique is that various stress contributions can be separately evaluated, especially the quenching stress, which, up to now, cannot be modeled without many assumptions. However, the use of a thin plate with macroscopic curvature generates very different experimental conditions compared to most industrially relevant applications. The latter involves rather thick, medium- or large-sized components like paper or steelmaking rolls, petrochemical industry ball valves, turbine shafts, train axles [Bolelli G et al. (2008)]. The main problems of this technique are the different substrate stiffness that can alter the stress distribution, compared to a real application, and the average deposition temperature and thermal history of the system that can vary significantly with the substrate heat capacity and torch spray pattern. For example, in the experiment of Hugot F et al. (2007), a metallic beam ($110 \times 15 \times 2$ mm) was fixed on a water-cooled rotating cylinder (Fig. 17.39a). The tangential velocity could be varied between 0.2 and 1.8 m/s, the torch being moved up and down at velocities ranging between 2 and 30 cm/s. The metallic plate was supported onto thin edge knives and held in position by two springs (Fig. 17.39c). The central deflection was measured with a LD-500-5 gauge transducer, the precision of which was 1 μm (Fig. 17.39c). The macroscopic preheating temperature was measured on sample back side by K-type thermocouple

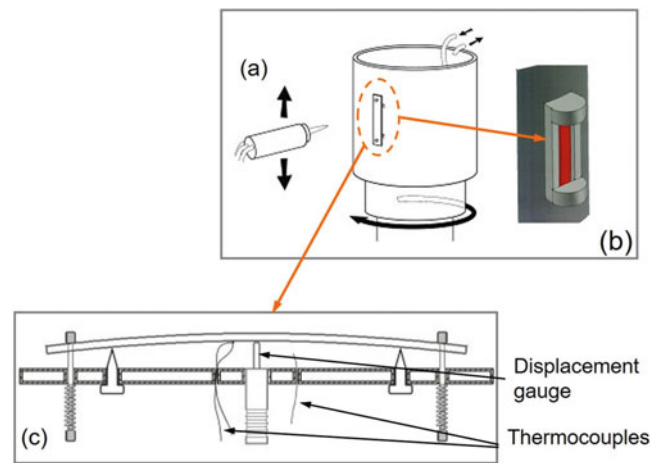


Fig. 17.39 (a) Scheme of the experimental stress evaluation device based on beam deflection measurement, (b) mask protecting the beam from excessive heating, and (c) cross-section of the metallic sample and its measurement device [Hugot F et al. (2007)]. (Reprinted with kind permission from Elsevier)

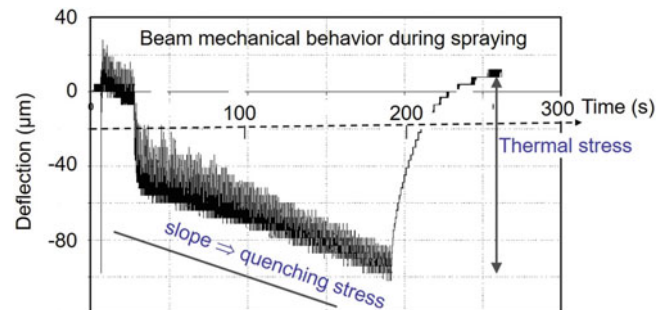


Fig. 17.40 Example of the evolution of the signal measured by the beam displacement gauge (see Fig. 15.40c) during plasma spraying of YSZ on grit-blasted substrate preheated at 200 °C during the first 250 s

(chromel–alumel). This measurement was performed 1 cm ahead of the displacement measurement (Fig. 15.39c). In order to protect the sensors from too high temperatures, a mask was fixed around the substrate (Fig. 17.39b). Two liquid CO₂ atomizing nozzles were positioned around the rotating cylinder, at 90° and 135° from the plasma torch respectively in order to control the substrate mean temperature. A typical signal obtained is presented in Fig. 17.40 for YSZ coating deposited on a grit-blasted stainless-steel substrate. The first 250 s corresponds to the preheating of the substrate up to 200 °C and a beginning of relaxation of the compressive stress induced by grit blasting can be observed. Then, during spraying (about 155 s) the slope of the beam deflection increases linearly (the slope corresponds to the quenching stress). At last, when the plasma jet and particle feeding are stopped, as well as the liquid CO₂ atomization, the coated beam cools down to room temperature in about 700 s. The corresponding gauge signal represents the stress due to the mismatch between substrate and coating expansion coefficients.

Stokes J, Looney L (2008) have listed all the analytical expressions related to quenching and expansion mismatch stress, often used when measuring them, and compared them with the predictions of finite elements model.

17.8 Thermal Properties

The thermal properties of coatings are of primary importance for engineering. The linear expansion coefficient, α_L (K^{-1}) of the coating plays a key role in the residual stress developed in the coating due to differences of expansion coefficients of coating and that of the substrate. In coating service conditions, the service temperature must be such that the stress generated by the expansion mismatch is below that generating the failure of the coating–substrate interface. The removal of the heat flux imparted to coating during service conditions depends strongly upon its thermal conductivity, κ_c (W/m K), which value also controls the temperature gradient generated within coating. Coatings are extensively used as thermal barriers in turbines, automotive engines, and their thermal conductivity, or thermal diffusivity in transient conditions, control their performances. Thermal diffusivity, a (m^2/s), is linked to the thermal conductivity κ_c , specific heat at constant pressure, c_p (J/K kg), and mass density, ρ (kg/m^3), by the expression:

$$a = \kappa_c / \rho c_p \quad (17.34)$$

In the following measurements of the density, thermal expansion coefficient and thermal diffusivity, measurements of the thermal conductivity are also presented. The section ends up with a review of measurements of thermal shock resistance of coatings.

17.8.1 Mass Density

The mass density of the coating, ρ_{300} , at room temperature (300 K) is mostly determined by Archimedean porosimetry [Andreola F, et al. (2000)] (see Sect. 17.5.1. and Eq. 17.8). To obtain its value at temperature T , the expansion coefficient, α_L must be known. If it is linear and isentropic, that is, the same value in all three directions, $\rho(T)$, T being expressed in Kelvin, is given by the following expression:

$$\rho(T) = \frac{\rho_{300}}{1 + 3\alpha_L(T - 300)} \quad (17.35)$$

In most coatings, however, the linear expansion coefficient of coatings with lamellar structure is not the same in the all three directions since α_L in the spray direction, perpendicular to the surface of the substrate, is different from the linear expansion coefficient in the directions parallel to the

substrate. In most measurement systems of expansion coefficients, the sample length required is a few millimeters. Such a length is easy to cut within the coating, but unfortunately, in most cases the coating thickness is a few hundreds of micrometers and samples in that direction are not suitable for the measurement.

17.8.2 Coefficient of Thermal Expansion

Different techniques include mechanical dilatometers, optical imaging and interference systems, X-ray diffraction methods, and electrical pulse heating techniques are used. For details, see the paper of James JD, et al. (2001); see also the ASTM standards [17.T1, 17.T2]. For thermal-sprayed coatings, the mechanical dilatometry is mostly used. The quantity that must be determined is

$$\alpha_L = \frac{1}{L} \frac{dL}{dT} \text{ or sometimes } \alpha_{L_0} = \frac{1}{L_0} \frac{dL}{dT} \quad (17.36)$$

In the first expression L is the sample length at temperature T , while in the second the measurement is carried out at room temperature. An alternative means of quantifying the sample expansion is in terms of the fractional increase in volume with temperature:

$$\alpha_v = \frac{1}{V} \left(\frac{dV}{dT} \right)_p \quad (17.37)$$

If the three linear expansion coefficients α_L are the same: $\alpha_v = 3\alpha_L$.

Thermal expansion measurements can also provide information about deviate from linearity, which happens when phase transformation or oxidation occurs and when stresses relax [Ilavsky J, Berndt CC (1998)]. To avoid the oxidation phenomena the dilatometer furnace must be maintained under controlled atmosphere when studying metals, alloys, or cermets.

17.8.3 Thermal Conductivity and Thermal Diffusivity

Thermal conductivity, κ_c , depends on three mechanisms [Pawlowski L (1995), Wang H, Dinwiddie RB (2004)]:

- Electronic conduction, κ_e , which is the main mechanisms for materials having free electrons (metals and alloys). In general, κ_e varies linearly with temperature at low temperatures and is not temperature dependent at higher temperatures.

- Lattice conduction (phonon conduction), κ_{ph} , which is the main mechanism for materials without free electrons, such as ceramics. At low temperatures, it depends exponentially upon temperature and the scattering of phonons by geometrical defects. At higher temperatures, the “Umklapp process” occurs and κ_{ph} varies as the reverse of temperature.
- Photon conduction, κ_{ph} , is important in optically absorbing dielectric materials (emission, absorption, and re-emission phenomena). κ_{ph} is proportional to T^3 . At high temperatures photons contribute to the conduction through pores, the thermal conductivity of the air or gas contained in the pores being low (~ 0.026 W/m K).

The thermal conductivity of thermal-sprayed coatings depends strongly on the coating structure, defects, porosity, real contacts between layered splats, and oxide impurity for metals or alloys, which are linked to the spraying process. For example, the low thermal conductivity of YPSZ plasma-sprayed coatings (about 1–2 W/m K) is due to the material but also to the poor contacts between layered splats that reduce phonons propagation. The sintering of coatings at high-temperature service conditions increases the thermal conductivity or diffusivity of the coating by improving the contacts between layered splats [Cernuschi Fet al. (2005), Gitzhofer F, et al. (1986)]. The results of Chi W, et al. (2006) also pointed out the important role of interlamellar porosity in both room temperature and temperature-dependent thermal conductivity. The modeling of thermal conductivity can be achieved using a finite element-based approach coupled with SEM image analysis of the coating microstructure for both through-thickness and in-plane directions for a single image [Kulkarni A, et al. (2003), Tan Y, et al. (2006)].

Most thermal conductivity measurements are performed through thermal diffusivity measurement, which implies measuring the mass density (see Sect. 17.8.1) and the specific heat at constant pressure (see Sect. 17.8.4) to calculate thermal conductivity according to Eq. 17.34. See ASTM references [17.T3, 17.T8]. Baba T, Ono A (2001) have developed an advanced laser flash system for thermal diffusivity measurements. The initial and boundary conditions for measurements are well defined and the transient temperature of the specimen is measured with a calibrated radiation thermometer, the entire curve of the measured temperature history being analyzed. A schematic representation of a Xenon flash diffusivity system used by Chi W, et al. (2006) is shown in Fig. 17.41a. Infrared (IR) detector is used for the monitoring of the temperature of the back surface of the sample (typically a small disk-shaped specimen) when heated by a short Xenon lamp pulses (pulse energy 12 J and duration 6–8 ms, over an 8 mm diameter area of the sample surface). The temperature history on its rear surface being detected by

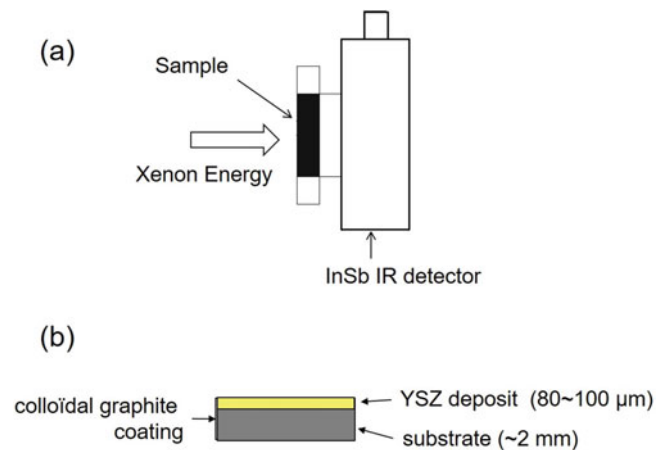


Fig. 17.41 (a) Schematic of the laser flash thermal diffusivity measurement system and (b) sample preparation using colloidal graphite painted to make surfaces opaque [Chi W, et al. (2006)]. (Reprinted with kind permission from Springer Science Business Media, copyright © ASM International)

the IR detector combined with a TV camera monitoring beam profiles. The infrared detector and the sample holder are completely shielded from the flash source by multiple shielding layers and addition of reflecting surfaces. The detector output signal is monitored from the beginning of the test and in between each shot, which assures that the following flash pulse starts only if the temperature of the sample is steady. When the material studied is translucent in the near infrared, as most oxide ceramics (for example, YPSZ), a thin layer of colloidal graphite paint is used as shown in Fig. 17.41b to make the surfaces opaque prior performing the thermal diffusivity measurement, on both the front and the rear faces of the sample.

For evaluating the thermal diffusivity, α , the simple solution proposed by Parker et al. can be used:

$$\alpha = 0.1388 \frac{L^2}{t^{1/2}} \quad (17.38)$$

where $t^{1/2}$ and L are the time corresponding to the half-maximum increase of the temperature and the sample thickness, respectively. The main advantages of this method are the simplicity and rapidity of measurement and the possibility to measure the thermal diffusivity on a wide range of materials over a wide range of temperature [Cernuschi F, et al. (2005)]. For more details about the method, see the paper of Baba T, Ono A (2001), and, for the reliability of the method, see the paper of Wang H, Dinwiddie RB (2000). The coating diffusivity can be measured with the coating detached from the substrate or with the coating attached to substrate, provided the thermal properties of the substrate are

known [He GH, et al. (2000), Rätzer-Scheibe H-J, et al. (2006)]. This technique can also be used for multilayer coatings [Jennifer SY, et al. (2001)] as well as to characterize nanometer-structured, solution plasma-sprayed, coatings. The lower thermal conductivity obtained compared to conventional coatings sprayed with micrometer-sized particles has been explained by the distribution and size of pores [Jadhav AD, et al. (2006)].

Instead of measuring the diffusivity, it is also possible to measure directly the thermal conductivity [Slifka AJ, et al. (1998)] using axial flow with hot plate according to ASTM C 177-85, or comparative cut bar, with guarded or unguarded heat flow meter method.

17.8.4 Specific Heat at Constant Pressure

The heat capacity (c_p) of coatings can be measured with a precision of about 1% [17.T9] using a wide range of calorimeters. These mostly comprise either one cell design, the adiabatic one being the simplest, or two cells where the studied sample is compared to a reference material [17.T10].

17.8.5 Thermal Shock Resistance

Thermal shock is a failure mechanism that occurs in materials, especially ceramics that exhibit a significant temperature gradient when they are subjected to a sudden change in temperature. The thermal shock resistance (TSR) describes the ability of the material (for example, a thermal barrier coating) to resist to rapid temperature variations without failure. Most methods used to characterize TSR involve heating the material to high temperature and then quenching it using water, oil, or air as cooling medium. The result depends both on the heating conditions: steady state flow, transient heating by convection, radiation, and the temperature drop. Quench tests generally must be repeated and in that

case the number of cycles necessary to cause a defined damage or weight loss can be used as a measure of the thermal shock resistance [Aksel C, Warren PD (2003)]. According to Hasselman DPH (1970), for steady heat flow and an infinite slab symmetrically heated or cooled, the TSR parameter is defined as

$$\text{TSR} = \frac{\sigma_f (1 - \nu)}{\alpha_L E'} \quad (17.39)$$

where σ_f is the fracture stress, ν the Poisson ratio, E' the Young's modulus, and α_L the mean expansion coefficient. Four more shock resistance parameters can be defined [Bolcavage A, et al. (2004)]. TSR of coatings is measured with the whole system: coating, bond coat, and substrate. It is thus important to keep in mind that the thermal shock must be adapted to the resistance of all components. For example, if the YPSZ topcoat can sustain temperatures up to 1200 °C and in some cases for relatively short periods 1300–1400 °C (military engines), it is not the case of the bond-coat and substrate superalloys. If possible, characterization means must reproduce service conditions, which is not always the case. Again, for a thermal barrier coating three tests are commonly used: Jet Engine Thermal Shock (JETS), Furnace Cycle Test (FCT), and Fluidized Bed Reactor (FBR) [Bolcavage A, et al. (2004)]:

- With the JETS the flame of a burner rig heats the coating surface, while the opposite side of the substrate is air cooled. It creates a thermal gradient of several hundred degrees Celsius across the TBC. The front surface temperature can reach 1400 °C and can initiate sintering. This test mainly stresses the ceramic layer and bond coat interface thermo-mechanically. Bond coat oxidation is rather low in this case. This test is reasonably quick and typically results are available within 2 days for a 2000-cycle test [Bolcavage A, et al. (2004)]. Figure 17.42a represents schematically the JETS process.

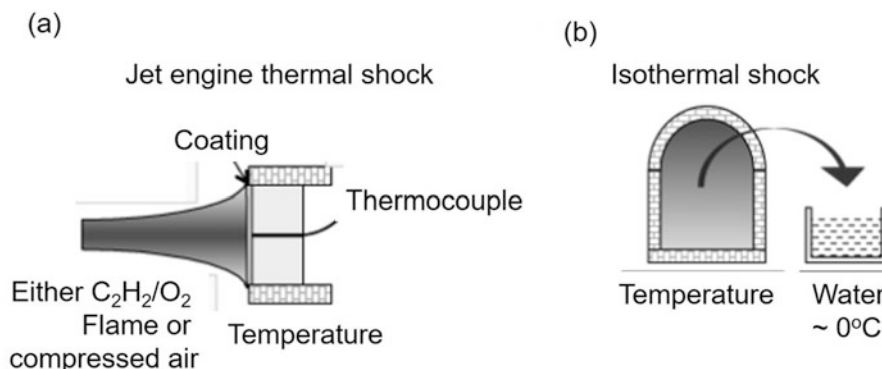


Fig. 17.42 Scheme of two thermal shock setups: (a) engine thermal shocks (JETS) heating with a burner rig and cooling with air jet and (b) furnace cycle test (FCT) using furnace heating and water soaking cooling [Montavon G (2004)]. (Reprinted with kind permission from Prof. G. Montavon)

- In the FCT test, the TBC system is oxidized and cycled in a furnace between room temperature and temperatures ranging from 1100 to 1200 °C. Thermal gradients across the TBC are moderate during the heat-up phase and significant during the cool-down phase. The sample is exposed for a long time to elevated temperatures, which leads to significant bond coat oxidation. The TBC temperature during soaking is too low to cause pronounced sintering in the ceramic. Figure 17.42b represents schematically the FCT process.
- FBR test consists of a standard fluidized bed furnace using alumina. It is typically operated at 1000 °C. Test samples are transported via a pneumatic system into a cooling zone in which compressed air is directed onto the TBC surface.

According to [Bolcavage A, et al. (2004)]: The JETS test provides performance-ranking data on the ceramic itself thanks to the high thermal gradients within the ceramic layer. The FCT reflects the actual engine condition because it also degrades the bond coat through severe oxidation, though it does not really address TBC degradation in the ceramic layer, which typically initiate above 1300 °C. The FBR used as a quality control tool as the standard 1000-cycle TCF test, does not discriminate differences well enough to provide quantitative data for a performance ranking. ASTM references for thermal shock testing are given in [15.T11–15.T15].

Other means used to measure TSR of thermally sprayed coatings include laser irradiation [Qi ZM, et al. (1988)] and infrared irradiation [Richard CS, et al. (1995)]. To increase the thermal gradient after heating, samples can be quenched in iced water instead of air jets [Irisawa T, Matsumoto H (2006)]. Nusair Khan A, Lu J (2003) have compared TBCs delamination when quenched using water or forced air jets:

- In both cases samples delamination starts from their extreme edges.
- In the case of the water-quenched samples, the thickness of the topcoat was only half of its original value, after 220 cycles, whereas in the case of the forced air-quenched samples, the spallation was only confined to the edges and the thickness of the topcoat remained the same even after 1000 cycles.
- In both cases more thermally grown oxide (TGO) was observed at the edges compared with the central portion of the samples.

To obtain more information than those resulting from visual inspection after a given number of cycles, AE can be used [Robin P, et al. (2010), Bolcavage A, et al. (2004)]. As a crack is initiated and propagates through a material,

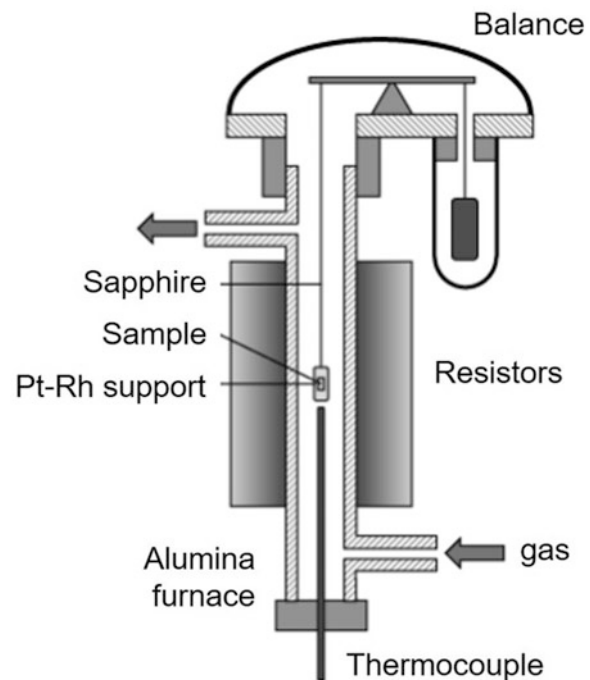


Fig. 17.43 Principle of a thermogravimetric balance [Montavon G (2004)]. (Reprinted with kind permission from Prof. G.Montavon)

measurable characteristics of the AEs from this event reveal details about the microstructure [Andrews DJ, Taylor JAT (2000)]. It is to be noted that a continuous AE signal corresponds to plastic deformation mechanisms, while burst-type AE results from micro-cracking in brittle materials, fracture of hard inclusions in alloys, and phase transformations. Such measurements allow determining when first cracks propagation occurs and the different fracture modes [Ma XQ, Takemoto M (2001)].

17.8.6 Thermal Analysis

Thermal analysis (TA) is a measure of physical property of a substance as a function of temperature [Sorai M, Gakkai NN (2004), Speyer R (1993)]. One of their main advantages is that they require rather small samples. For more details about these techniques, the reader can see the books of Sorai M, Gakkai NN (2004) or Speyer R (1993). In the following, a few examples are presented of these techniques used in the thermal spraying area to characterize phase changes in powders or coatings, reactions at high temperatures and oxidation. TA techniques mainly used for characterizations of sprayed coatings or sprayed powders include:

Thermogravimetry (TG): In which the mass of a sample is recorded, in a controlled atmosphere or air (see Fig. 17.43), as a function of temperature. On the one hand, mass is lost if the substance contains a volatile fraction and TG

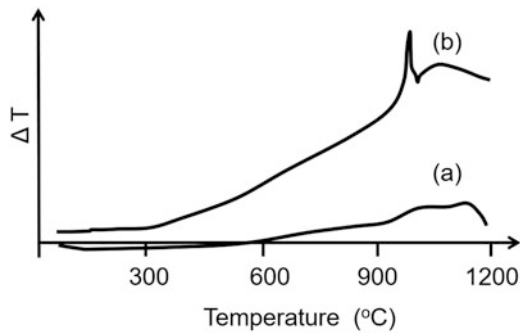


Fig. 17.44 DTA obtained from (a) initial mullite powder and (b) as-sprayed mullite coating at substrate temperature of 300 °C [Salimijazi H, et al. (2012)]. (Reprinted with kind permission from Springer Science Business Media, copyright © ASM International)

measurement can be coupled with a device permitting the analysis of volatile products, and on the other, mass is gained with oxidation.

Differential scanning calorimetry (DSC): The difference in the heat flow absorbed by the test sample is compared with the heat flow absorbed by a reference material, as a function of the temperature. Experiments are performed in a controlled atmosphere. DSC provides information about thermal changes that do not involve a change in sample mass such as phase changes or changes in chemical composition. It also allows checking the material purity through changes in heat of fusion and melting point and studying sample oxidation in oxidizing atmospheres.

Differential thermal analysis (DTA): In which the temperature difference between a substance and a reference material is measured as a function of temperature, both materials being subjected to the same programmed temperature profile. Experiments are performed in a controlled atmosphere. The reference material is a known substance, generally inactive thermally within the temperature range of interest.

17.8.6.1 Phase Changes

Salimijazi H, et al. (2012) have compared plasma-sprayed coatings made with commercially available mullite powder particles and a mixture of mechanically alloyed alumina and silica powder particles. DTA was used to study the phase transformations in the coatings. Figure 17.44 represents the DTA curves obtained for mullite initial powder and the as-sprayed mullite coating on stainless steel substrate, at temperature of 300 °C. Neither exothermic nor endothermic peaks were observed for the mullite powder. A peak around 980 °C could be observed in the as-sprayed structure that was attributed to the crystallization of amorphous aluminum silicate.

Garcia E et al. (2011) have air plasma sprayed with an Axial III plasma torch plain mullite, 75 vol.% mullite–

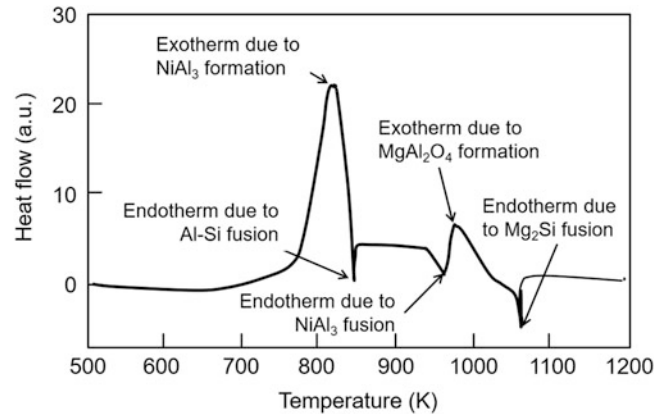


Fig. 17.45 DTA scan of granulated SiO₂/Ni/Al–Si–Mg particles heated to 1273 K with heating rate of 0.17 K/s in argon atmosphere [Ozdemir I, et al. (2005)]. (Reprinted with kind permission from Springer Science Business Media, copyright © ASM International)

25 vol.% Y–ZrO₂, and 50 vol.% mullite–50 vol.% Y–ZrO₂ powders. DTA of as-sprayed plain mullite coatings showed no endothermic or exothermic event, supporting the fact that as-sprayed coating was fully crystallized, which was not the case with the two other powders. The authors stated that mullite crystallization was hindered in the composites during the spray process. Liu X, Ding C (2002) studied phase changes of plasma-sprayed wollastonite (CaSiO₃) coatings. The DTA curves showed that the wollastonite powder had no chemical reactivity from room temperature to 1000 °C, whereas an obvious exothermic reaction occurred in the wollastonite coatings at about 882 °C. Crystalline wollastonite, glassy phase, and tridymite (SiO₂) were observed in the coating. Tridymite (SiO₂) likely reacted with other compounds such as CaO and glassy phase to form crystalline wollastonite when the coating was heated at about 882 °C.

17.8.6.2 Reactive Thermal Spraying

Reactive thermal spraying (RTS) in which thermodynamically stable compounds are formed by in-process reactions, has attracted considerable attention leading to the wide availability of in-situ synthesized composite coatings. Ozdemir I et al. (2005) have HVOF sprayed a composite powder of SiO₂/Ni/Al–Si–Mg onto an aluminum substrate. To identify the reactions which were taking place in flight, they heated the same materials in a DTA over the temperature range of 298–1273 K under argon atmosphere with a heating rate of 0.17 K/s. Figure 17.45 presents the DTA curve.

Deevi SC, et al. (1997) have studied the reactive spraying of nickel aluminide when nickel and aluminum powders were plasma sprayed onto carbon steel substrates. To illustrate the exothermic reaction between nickel and aluminum, a mixture of nickel and aluminum in a 1:1 atomic ratio was heated in a

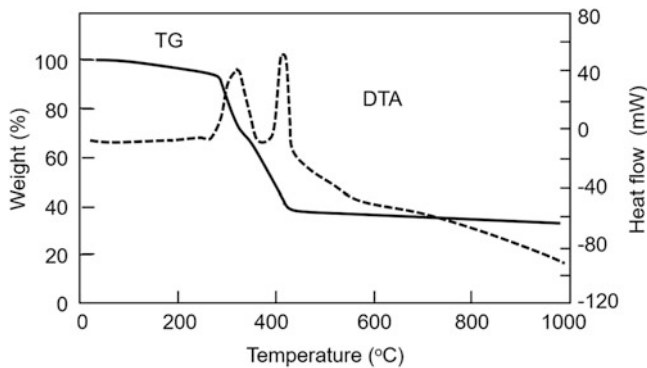


Fig. 17.46 Thermal gravimetric–differential thermal analysis curves of dried MgO–Y₂O₃ precursor at a heating rate of 10 °C/min [Wang J, et al. (2010)]. (Reprinted with kind permission from Springer Science Business Media, copyright © ASM International)

DTA unit under argon atmosphere. Wang J, et al. (2010) have synthesized by a sol–gel combustion process MgO–Y₂O₃-nanostructured composite powder (volume ratio of 50:50) with crystal sizes in the 10–20 nm ranges. The powder was used for plasma spraying. The formation process was studied by TG-DTA of the 200 °C dried MgOY₂O₃ powder precursor as a function of temperature at a heating rate of 10 °C/min. As illustrated in Fig. 17.46, the sample weight decreased continuously with the increasing of temperature up to 1000 °C, with a total weight loss of about 67%. Two exothermic peaks observed at 326 and 419 °C were ascribed to the pyrolysis of the precursor (see the DTA curve). The TG curve showed that after 600 °C, the pyrolysis process was completed.

Ravi BG et al. (2008) studied the RF precursor plasma spray (RF-PPS) synthesis process. It starts with liquid inorganic precursors and directly produces ceramic coatings as yttrium aluminum garnet (YAG). The sols used were either regular or reverse ones [Ravi BG et al. (2008)]. To gain a better insight in the process, thermal analysis (DTA-TG curves) was performed on the coatings. The TG plots showed that the as-sprayed coatings had substantial amount of volatile matter. However, subsonic-sprayed coatings lost less weight than the supersonic-sprayed coatings, probably due to the relatively longer residence times of particles in subsonic spraying allowing for the improved pyrolysis of the sols.

17.8.6.3 Oxidation Resistance

Guilemany JM, et al. (2009) have explored transition metal aluminide in HVOF-sprayed coatings of two different aluminide (FeAl and NbAl₃) feedstock powders in terms of resistance to oxidation and mechanical behavior. They have studied the heat flow and mass gain-temperature dependence for the as-sprayed coatings during the oxidation test in DTA–TGA equipment. The oxidation analysis revealed that despite the high melting point of NbAl₃, it suffers from intergranular

disintegration at moderate temperatures. The high level of oxidation and coating defects that facilitated oxygen diffusion inwards and Al depletion in the as-sprayed coating itself favored this phenomenon. Fan X, Ishigaki T (2001) used induction plasma spray processing to produce freestanding parts of Mo₅Si₃-B composite and MoSi₂ materials. Oxidation resistance of the specimens was evaluated through the TG tests. The specimen temperature was increased at 20 °C/min to the preset temperature, 1210 °C, and held for 24 h, during which time the mass changes and temperature of the specimens were continuously recorded. The performance of Mo₅Si₃-B composites at high temperature was found to depend strongly on the composite boron content, for example, at boron contents greater than 1 wt.%; composites demonstrated encouraging oxidation resistance in the high-temperature environment.

17.9 Wear Resistance

Wear is generally classified into six distinguishable types [Pawlowski L (1995)] as described below according to Craig BD (2005) and Chattopadhyay R (2001). Information about standard terminology relating to wear and erosion can be found in 17.W1.

The wear volume, V_w , defined by the following equation, characterizes wear [Chattopadhyay R (2001)]:

$$V_w = K_w \frac{F_N}{H} \times d_w \quad (17.40)$$

where d_w is the sliding distance, F_N is the applied normal force, H is the hardness or yield stress of the softer surface, and K_w is the wear coefficient. The depth of wear δ_w is expressed as

$$\delta_w = K_w \frac{F_N}{H} \cdot \frac{d_w}{A_w} \quad (17.41)$$

where A_w is the area of contact, $V = \delta_w A_w$

The wear coefficient K_w depends on the wear mode, materials and lubrication system used, type of motion, stress distribution. Chattopadhyay R (2001)] has summarized typical values of K_w .

For adhesion wear the following equation is used:

$$\frac{V_w}{d_w} = K_{adh} \frac{F_N}{H} \quad (17.42)$$

where $K_{adh} = K_w/3$.

In erosive wear, the volume loss is given by

$$V_w = \frac{1}{2} \frac{mv^2}{H} f(\alpha) \quad (17.43)$$

where H is the hardness or yield strength of the surface material, $\frac{1}{2} mv^2$ is the kinetic energy of the impacting particles, and $f(\alpha)$ is a function of the impingement angle α , which plays a key role in the erosion. For brittle materials, V_w increases with higher angles, while it is the reverse for ductile materials.

It must be underlined that any kind of wear produced with the adapted testing machine is often measured with the use of optical methods giving the wear track profile as well as the debris distribution.

17.9.1 Abrasive Wears

Abrasive wear occurs when a solid surface experiences the displacement or removal of material as a result of a forceful interaction with another hard surface. Both free-flowing particles and abrasive attached to the counter body cause wear. Two types of abrasive wear are defined based on the degree of stress in the component surface or the number of components involved. In the two-body abrasion, under low stress conditions, abrasive particles (asperities or hard particles) sliding against the component surface cause scratches, but the stress induced does not cause fragmentation of abrasives. Three-body or high stress abrasion occurs when the abrasive particles are forced between two mating surfaces leading to loss of materials from both component surfaces [Chattopadhyay R (2001)]. A few abrasive tests proposed by ASTM are given in 17.W2–17.W5.

For the abrasive wear tests, in laboratories two main tests are performed [Kennedy DM, Hashmi MSJ (1998),

Bolelli G, et al. (2006), Cockeram BV, Wilson WL (2001), Wielage B, et al. (1999) Schmidt G, Steinhäuser S (1996)]:

- The pin-shaped material rotates on an abrasive disk, or an abrasive cloth, or paper mounted on a flat disk. The debris can be blown out with a gas jet to determine if their presence improves or not the wear resistance.
- Free or loose abrasive is interposed in between the two surfaces pressed against each other. One is in sliding or rotating motion while the other is stationary.

Many results are described in the literature and a few of them illustrated in the following references [Gawne DT, et al. (2001), Li C-J, et al. (2011), Rainforth WM (2004), Kim HJ, et al. (1994), Tillmann W, et al. (2008a, b), He D-Y, et al. (2008) and Magnani M, et al. (2009)], tests being performed at room or high temperature, depending on the coating application.

17.9.2 Adhesive Wears

Adhesive wear occurs between two surfaces in relative motion because of the inherent roughness of material surfaces. It is also called sliding wear [17.W6]. In adhesive wear, the peaks on the adjacent surfaces that do come into contact plastically deform under pressure and form atomic bonds at the interface and in some cases this is considered solid-phase welding. As the relative motion between the surfaces continues, the shear stress at the bonded contact point increases until the shear strength limit of one of the materials is reached and the contact point is broken, bringing with it a piece of the opposing surface. The broken material can then either be released as debris or remain bonded to the other material's surface [Craig BD (2005) and

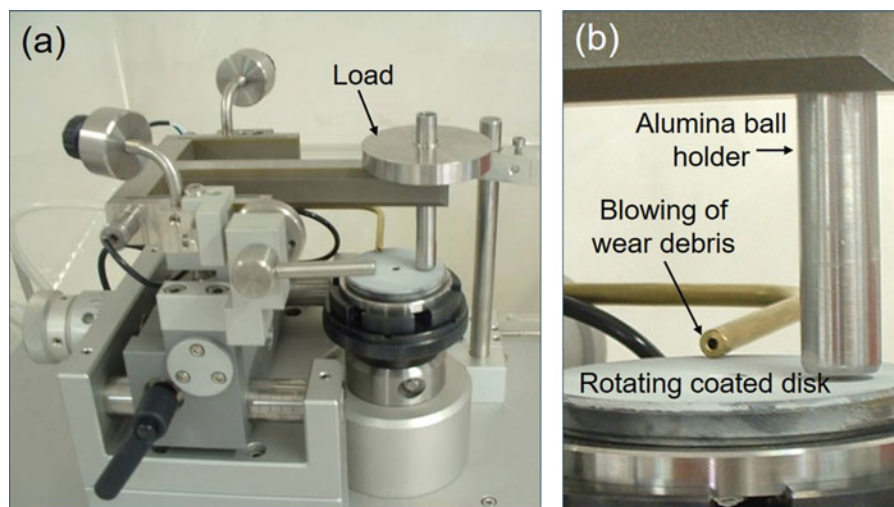


Fig. 17.47 Pin-on disk test with a rotating coated disk, 6 mm diameter ball made of sintered alumina (a) general view and (b) detailed view

Chattopadhyay R (2001)]. The most used tests are Chattopadhyay R (2001), Kennedy DM, Hashmi MSJ (1998), Bolelli G, et al. (2006), Cockeram BV, Wilson WL (2001), Wielage B, et al. (1999) and Schmidt G, Steinhäuser S (1996):

- The pin-on-disk [17.W7, 17.W8] where a pin specimen, with an extremity either flat or spherical, is tightly pressed against a flat circular-coated disk with a specified load. During the test either the pin or the disk rotates, see Fig. 17.47, and the sliding path forms a circle on the rotating disk surface. The debris can be blown out with a gas jet to determine if their presence improves or not the wear resistance. It is also possible to have the disk vertical and the pin horizontal to entrain the debris by gravity or achieve tests with lubrication.
- The pin-on-plate where the coated plate reciprocates at 50–300 cycles per minute.
- The pin or block-on-ring where the coated sample slides on the edge of a disk or a ring mounted vertically. This test reproduces the type of motion found in engine cam or internal combustion systems.

Few equipment can work at high temperatures to test the evolution of the wear. This is for example the case of the experiment of Yin B, et al. (2010) who studied the sliding wear behavior of HVOF-sprayed $\text{Cr}_3\text{C}_2\text{-NiCr/CeO}_2$ composite coatings at temperatures up to 800 °C. Friction and wear tests were carried out in a ball-on-disk contact configuration using an SRV (sliding, reciprocating, and vibrating) friction and wear tester.

Many results are described in the literature and a few of them illustrated in the following references [Fernandez JE, et al. (1995), Liu Y, Wang HM (2010), Tiana W, et al. (2009), Lin JF, et al. (1996), Yanga Q, et al. (2006) and Guilemany JM, et al. (2001)].

The extreme form of adhesive wear is galling that involves excessive friction between the two surfaces, resulting in localized solid-phase welding, and subsequent spalling of the mated parts [Chattopadhyay R (2001)]. This process causes significant damage to the surface of one or both

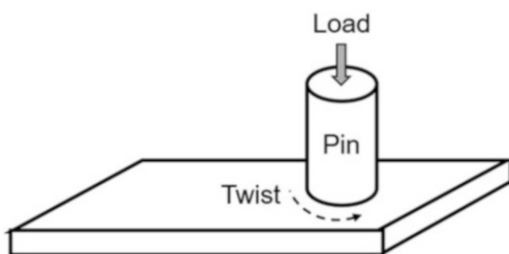


Fig. 17.48 Principle of galling test setup [Chattopadhyay R (2001)]. (Reprinted with kind permission from ASM International)

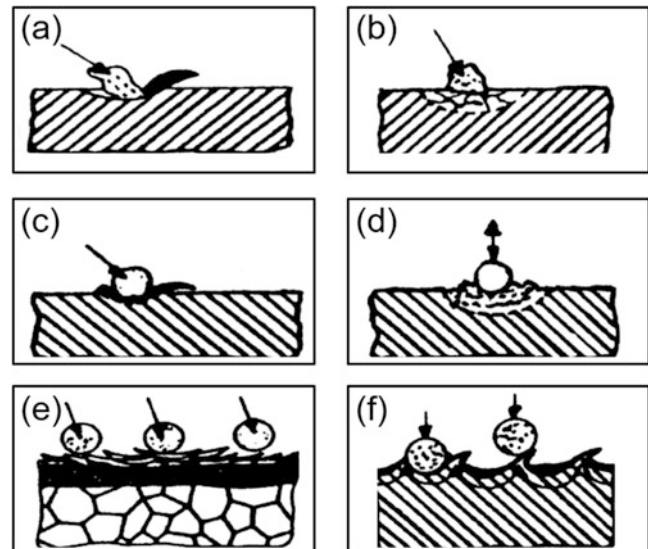


Fig. 17.49 Erosive wear due to particle impact: (a) microcutting and microploughing; (b) surface cracking; (c) extrusion of material at the exit end of the impact crater; (d) surface and subsurface fatigue cracks; (e) formation of thin platelets due to extrusion and forging; and (f) formation of platelets by a backward extrusion process [Stewart S, et al. (2005)]. (Reprinted with kind permission from Elsevier)

materials. The typical test is shown in Fig. 17.48: the pin specimen, gradually load, against a rotating counter plate material. The load at which the pin tends to gall onto the plate is the galling load [Wielage B, et al. (1999)]. The ASTM test is referenced [17.W8].

17.9.3 Erosive Wear

Erosive wear is the continuous deterioration of a material by fluid carrying solid particles [17.W6]. When the fluid is traveling in a direction that is normal to the surface of the material, it can be considered as impact wear. The repeated impact by particles that are very small relative to the size of the material being impacted, results in erosive wear. Whatever may be the size of impacting particles, they can cause deformation to the material being impacted that can result in the ejection of particles from the material's surface or the formation of near-surface cracks that under repeated impact can cause pieces of the surface to fracture. Figure 17.49 from Kennedy DM, Hashmi MSJ (1998) summarizes the different phenomena implied in erosive wear. One conventional test is described in 17.W10.

Cavitation wear, occurring during liquid impingement by the collapse of bubbles on the coating solid surface, is also considered as erosive wear. The deformation of solids by the impact of liquid occurs because of the interaction of stress waves generated by the collapsing bubbles with the surface.

For dry erosion wear, the test mostly used consists of repeated impact erosion by a flow of 50 μm mean diameter

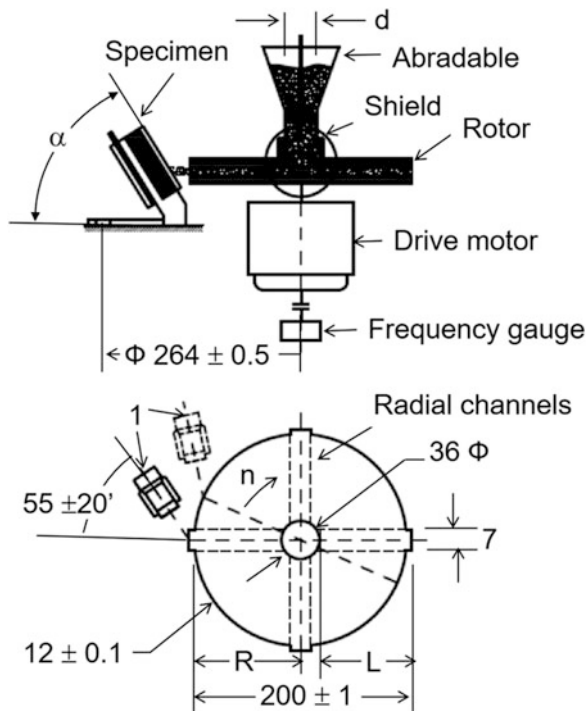


Fig. 17.50 Impact erosive wear tester for materials in abrasant particles jet [Kulu P, Pihl T (2002)]. (Reprinted with kind permission from Springer Science Business Media, copyright © ASM International)

angular alumina particles exiting a tungsten–carbide nozzle (50 mm in length and 1.5 mm in internal diameter) with a mean velocity of 30 m/s. Crushed silica with grain size below 0.1 mm is also used for erosion tests. As for grit blasting the nozzle wears and must be replaced as soon as its internal diameter has increased by 10%. Blasting time is generally 10 min and the nozzle axis must be kept orthogonally to coating. When dividing erosion rate (mg/min) by the abrasive flow rate (g/min) one obtains the average erosion rate after dividing the result by the specimen mass density. The averaged erosion rate is thus expressed in mm^3/g .

To characterize the impact erosion in severe but cold conditions, Kulu P, Pihl T (2002) have developed an impact erosion wear tester (Fig. 17.50), based on centrifugal force. It produces a stream of abrading-quartz sand with abrasive particle size of 0.1–0.3 mm and abrasive hardness 1100–1200 HV. The velocity of abrasive particles is 80 m/s. It can also use abrasives of different hardness (from 120 to 2000 HV) such as limestone, glass, iron oxide, quartz, and corundum. The measurements of weight loss allow for the calculations for weight and volume losses as a measure for wear rate; that is, the loss of mass or volume per 1 kg of abrading material in mg/kg and mm^3/kg , respectively. The impact angle, α , can be varied easily, see Fig. 17.50.

In liquid cavitation erosion, tensile stresses are generated during liquid impingement by the collapse of bubbles on a solid surface. It results in solid deformation because of the

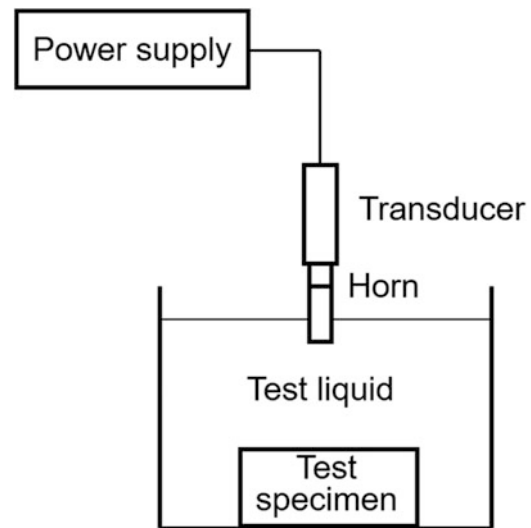


Fig. 17.51 Cavitation erosion test [Chattopadhyay R (2001)]. (Reprinted with kind permission from ASM International)

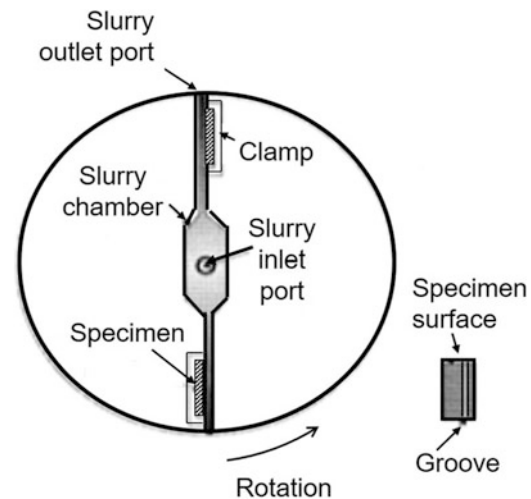


Fig. 17.52 Schematic of the Coriolis erosion tester [Clark HMI, et al. (1999)]. (Reprinted with kind permission from Elsevier)

interaction of stress waves generated by the collapsing bubbles. Two ASTM tests are referenced in [17.W11, 17.W12]. According to Chattopadhyay R (2001), a simple testing method of cavitation is that developed by Shal'nev and represented in Fig. 17.51. The material to be tested is exposed to sound waves, produced by a magnetostriction vibrator with a nickel pipe 20 mm in internal diameter, oscillation frequency of 8000 Hz, and amplitude of 0.066 mm.

Liquid erosion with slurry, generally an alumina slurry, combines high abrasive conditions with cavitation. For example, the test rig [Clark HMI, et al. (1999)] showed in Fig. 17.52 uses a steel wheel, which rotates against a flat-coated specimen in slurry containing sharp alumina particles, subjecting the samples to combined impact erosion. The extent of erosion depends on the composition, size, and shape of the eroding particles, their velocity and angle of

impact, and the composition and microstructure of the surface being eroded. The method utilizes the combination of centrifugal and Coriolis accelerations in a revolving rotor to pass slurry rapidly across a test surface such that the solid particles are forced against the surface, producing wear during their passage. The device allows using flat plate specimens and rotation speeds up to 7000 rpm, resulting in very short wear test times of 1 or 2 min. For example, a wear scar formed in a ductile material during a Coriolis erosion test

shows a progressive increase in depth with distance from the rotation center of the device.

Different examples of erosive wear for coatings sprayed with various processes are given in the following references [Ji G-C, et al. (2007), Dallaire S (2001), Shivamurthy RC, et al. (2010), Hejwowski T, et al. (2000), Hejwowski T (2009) Mann BS, Arya V (2001) Prasad Sahu S, et al. (2010)].

17.9.4 Surface Fatigue

Surface fatigue wear not only results in material loss from the surface, but it can also reduce the working life of the engineering component. It is the process leading to progressive localized permanent structural change in a material subjected to fluctuating stresses and strains. The cumulative effects of progressive changes in service conditions may result in cracks and/or complete fracture after a certain number of cycles. For coatings, for example, it happens in contact with a rolling motion. Fatigue is discussed according to two categories based on the number of cycles to failure. In high-cycle fatigue situations, materials performance is commonly characterized by an $S-N$ curve, also known as a Wöhler curve. In this test constant cyclic stress amplitude S is applied to a specimen and the number of loading cycles N until the specimen fails is determined. It results in a graph of the magnitude of a cyclic stress (S) against the logarithmic scale of cycles to failure (N), see Fig. 17.53. The coupon with its coating manifests variation in its number of cycles to failure, and the $S-N$ curve should more properly be an $S-N-P$ curve capturing the probability of failure after a given number of cycles of a certain stress. Probability distributions that

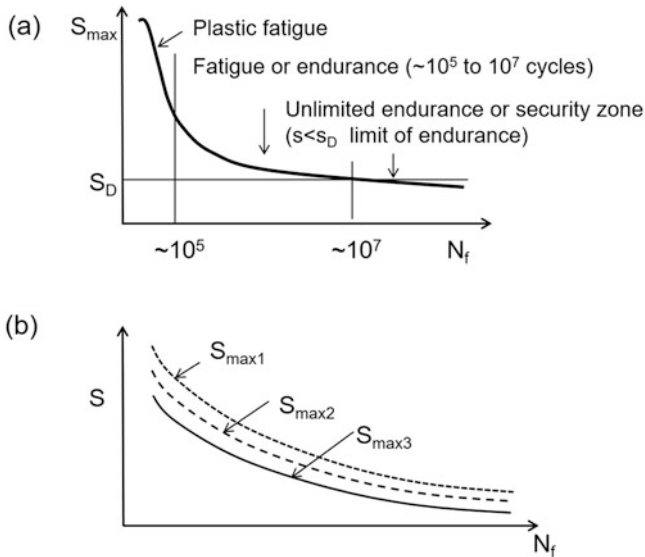


Fig. 17.53 $S-N$ diagram plots: nominal stress amplitude S versus cycles to failure N : (a) $S - N$ curve for fatigue and (b) evolution of the $S-N$ curve for different S_{max} [Chattopadhyay R (2001)]. (Reprinted with kind permission from ASM International)

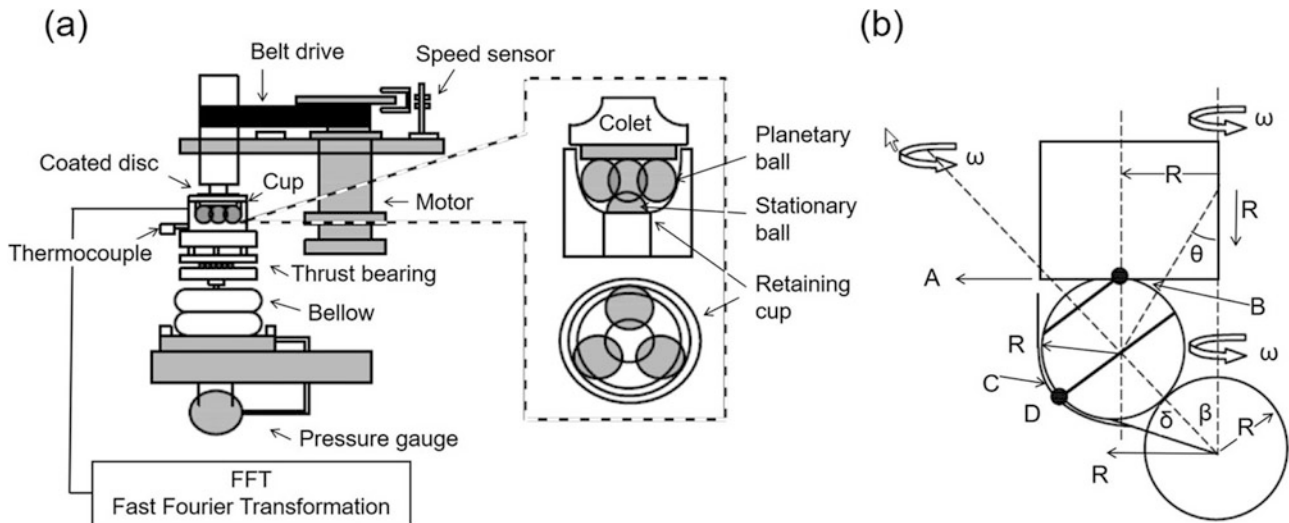


Fig. 17.54 (a) Schematic of the modified four-ball machine (b) schematics of ball and disk kinematics in cup assembly: $R_i = 7.75$ mm, $R_p = 6.35$ mm, $\theta = 36.83^\circ$, $\beta = 37.61^\circ$, $\delta = 31.16^\circ$, $\omega = 4000 \pm 10$ rpm

[Ahmed R, Hadfield M (2002)]. (Reprinted with kind permission from Elsevier)

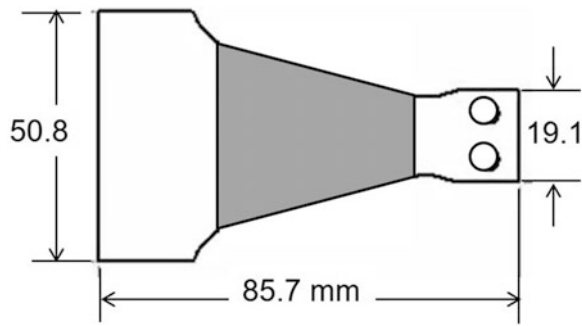


Fig. 17.55 Bending fatigue strength specimen. The gray region corresponds to the coated area. Dimensions are in mm [McGrann RTR, et al. (1998)]. (Reprinted with kind permission from Springer Science Business Media, copyright © ASM International)

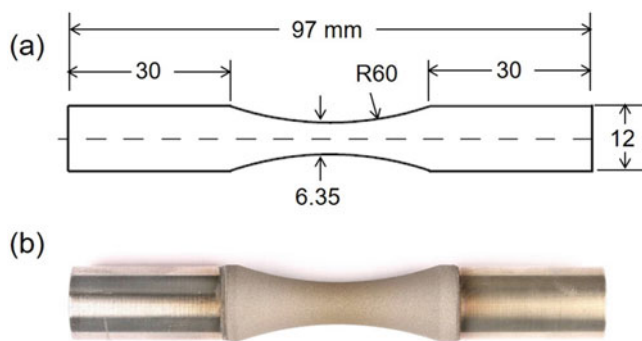


Fig. 17.56 Axial fatigue specimens. All the dimensions are in mm. (a) Drawing and (b) as WC-CoCr sprayed [Agüero A, et al. (2011)]. (Reprinted with kind permission from Springer Science Business Media, copyright © ASM International)

are common in data analysis and in design against fatigue include lognormal distribution, Weibull distribution and others. High-cycle fatigue occurs under low stress S_{\max} and fracture occurs at $N = 10,000$ cycles or greater ($N \geq 10^4$).

Low-cycle fatigue is represented by the $E-N$ curves ($E = \text{strain} = E_p + E_e$, E_p being the plastic strain and E_e the elastic one) and failure occurs below 10,000 cycles ($N < 10^4$). To improve the fatigue resistance, compressive residual stresses can be introduced in the surface by, for example, shot peening to increase fatigue life. On the contrary, tensile stress decreases the fatigue resistance. Of course, fatigue life, as well as the behavior during cyclic loading, varies widely with the material or coating considered. Extreme high or low temperatures can decrease fatigue strength as well as environmental conditions resulting in erosion, corrosion, or gas-phase embrittlement.

Various means are used to characterize coating's fatigue:

Cyclic fatigue and fracture mechanisms [17.W13], thermomechanical fatigue testing [17.W14], cyclic fatigue, and fracture mechanisms [17.W15–17.W17].

For highly loaded machine elements such as roller bearings and gears, subjected to a combined rolling/sliding

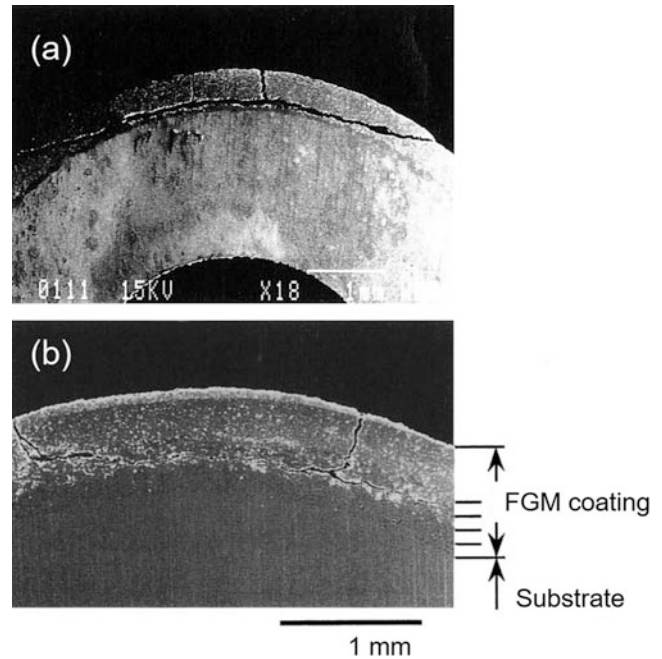


Fig. 17.57 (a) SEM micrographs showing interface delamination cracking for non-FGM coating subjected to six thermal fatigue cycles and (b) corresponding micrographs showing interface delamination cracking for FGM coating subjected to 10 thermal fatigue cycles, where laser power was 34 W. [Zhou YC, Hashida T (2002)]. (Reprinted with kind permission from Elsevier)

motion, extensive tests have to be performed [Stewart S, et al. (2005)]. Stewart S, et al. (2005) have proposed a modified version of the standard four-ball machine, where steel discs 31 mm in diameter were fabricated, coated, and then HIPed. A number of modifications to the four-ball machine were thus necessary in order to maintain the correct rolling/sliding kinematics. Figure 17.54a, b presents the details of the setup. Test results revealed that performance of the coating was dependent on the microstructural changes due to post-treatment. Ahmed R, Hadfield M (2002) have used a similar setup to study different coatings, but in this case the substrate material was either 440-C, M-50 bearing steel, or mild steel in the shape of rolling element ball or cone.

Zhang XC, et al. (2009a) have used the rolling contact testing machine developed by Yanshan University in China to the Rolling Contact Fatigue (RCF) resistance and failure mechanisms of plasma-sprayed CrC–NiCr cermet coatings.

Much less sophisticated tests are those based on Young's modulus measurement at increasing deformation of up to 0.3% [Kovarik O, et al. (2005) (2008)]. For example, Kovarik O, et al. (2005) have loaded the fatigue samples in reversible bend (as a cantilever beam) at room temperature in a special computer-controlled electromagnetic testing device. An alternating electromagnetic field induced by a pair of coils was used to deflect the free end of the specimen, which was equipped by a yoke. Other authors [McGrann RTR, et al. (1998), Sansoucy E, et al.

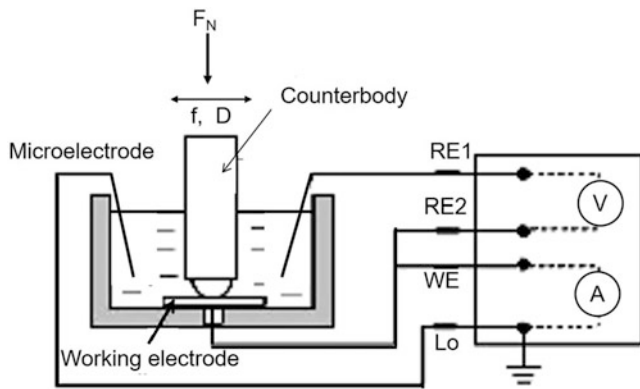


Fig. 17.58 Experimental setup combining a bidirectional sliding test immersed in an electrolyte and electrochemical noise measurements [Basak AK, et al. (2006)]. (Reprinted with kind permission from Elsevier)

(2007)] used specimens supported in the same manner as a cantilevered beam at one end and that were subjected to an alternating force at the other. The fatigue test specimen shown in Fig. 17.55 includes a triangular shape intended to produce a constant stress along the length of the test section.

Other authors [Ibrahim A, et al. (2007), Ibrahim A, Berndt CC (2007)] have used rotating-beam fatigue testing machines, where test specimens are coated bars (12.7 mm in diameter). The fatigue experiments were conducted at room temperature under a rotating beam and stress ratio of $R = -1$ configuration at a load frequency of 50 Hz. The maximum load P_{\max} generating a tensile stress, considered positive, is equal to the minimum load P_{\min} generating a compressive stress, considered negative. The stress ratio corresponds to the ratio of the minimum stress to the maximum one during one cycle of loading in a fatigue test.

Fatigue resistance has also been tested with a torsional setup [Yan L, et al. (2003)].

For the axial fatigue strength test, a sinusoidal load of 20 Hz with load ratio of $R = -1$, at room temperature (23 ± 2 °C), and $35 \pm 3\%$ humidity was applied by Agüero A, et al. (2011). Experimental tests considered as fatigue strength the specimen fracture or 5×10^6 load cycles. The test was performed on two MTS computer-controlled servo-hydraulic axial fatigue-testing machines, according to the ASTM E466 standard. Figure 17.56 presents the test sample dimensions and a picture of the coated fatigue specimen.

At last thermal fatigue resistance, generally of TBCs, is tested with furnaces and/or laser [Scrivani A, et al. (2007), Giolli C, et al. (2009), Zhu D, et al. (2004), Zhou YC, Hashida T (2002)]. For example, Scrivani A, et al. (2007) have tested thick (1.8 mm) plasma-sprayed TBCs by introducing them in a furnace, heating them up to 1150 °C in 5 min, letting them stabilize at 1150 °C during 45 min, followed by a 10-min forced

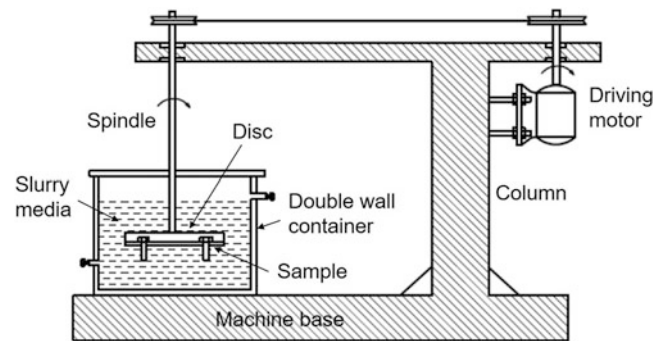


Fig. 17.59 A schematic representation of the slurry wear tester [Prasad BK (2000)]. (Reprinted with kind permission from Elsevier)

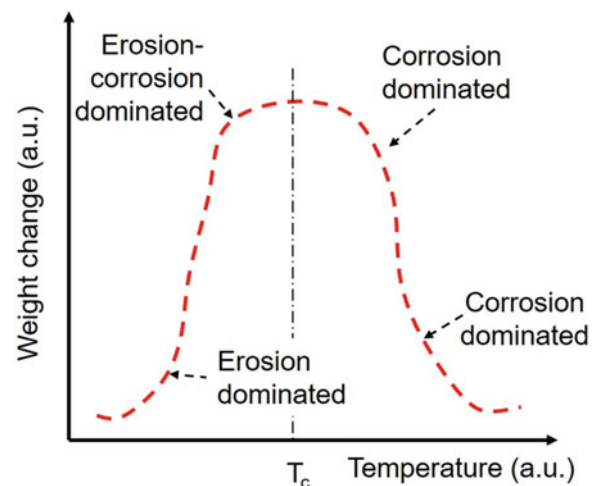


Fig. 17.60 Scheme of corrosion-erosion wear at high temperature [Chattopadhyay R (2001)]. (Reprinted with kind permission from ASM International)

air cooling. Failures occurred after 305–455 cycles, depending on the spray conditions. When looking at the limits of the TBC the thermal fatigue resistance increases with amount of porosity in the topcoat. Following the thermal cycling tests, the compressive in-plane stress increases in the TBC systems and it is less a function of the porosity level of topcoat. [Robin P, et al. (2010)] also observed the modification of the stress distribution. In their setup coatings were heated by radiating lamps and acoustic emission allowed following cracks formation during the heating and cooling stages. The bond coat or the Functional Gradient Material (FGM) play an important role in the coating resistance to thermal fatigue [Zhou YC, Hashida T (2002)]. SEM micrographs given in Fig. 17.57a, show interface delamination along the boundary between PSZ/NiCrAlY (75/25 wt. %) and PSZ/NiCrAlY (50/50 wt. %) for “non-FGM” coating subjected to six thermal fatigue cycles, where the exposed time for every cycle was 70 s and the highest temperature on coating and substrate was 1200 and 600 °C, respectively. The Corresponding micrographs given in Fig. 17.57b obtained

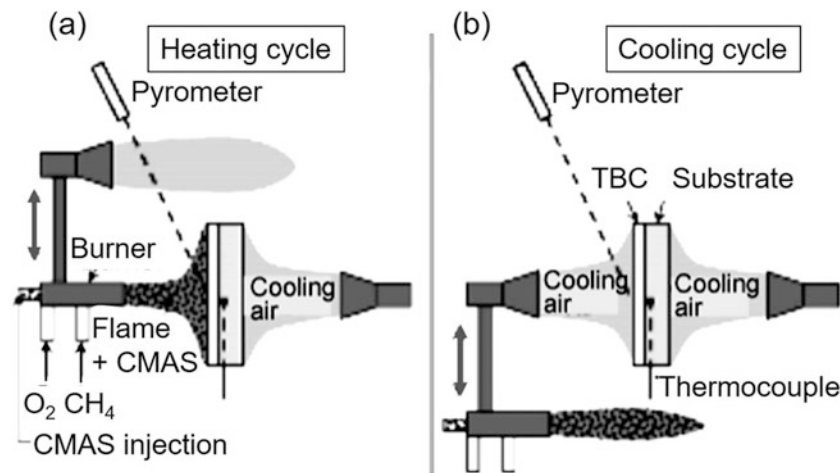


Fig. 17.61 Schematic diagram of thermal-gradient cyclic testing of TBCs with CMAS injection during (a) heating and (b) cooling cycles [Drexler JM, et al. (2010)]. (Reprinted with kind permission from Elsevier)

with FGM coating subjected to 10 thermal fatigue cycles tests conducted under the simulated advanced gas turbine blade thermal cycling conditions, show higher thermal fatigue resistance compared to non-FGM coating system.

17.9.5 Corrosive Wears

Corrosive wears occur when the effects of corrosion and wear are combined, resulting in a more rapid degradation of the material's surface [17.W18, 17.W19]. A surface that is corroded or oxidized may be mechanically weakened and more likely to wear at an increased rate. Furthermore, corrosion products including oxide particles that are dislodged from the material's surface can subsequently act as abrasive particles. Stress corrosion failure results from the combined effects of stress and corrosion. At high temperatures reactions with oxygen, carbon, nitrogen, sulfur, or flux (chemical cleaning agent) result in the formation of oxidized, carburized, nitride, sulfurized, or slag layer on the surface. Temperature and time are the key factors controlling the rate and severity of high temperature corrosive attack [Chattopadhyay R (2001)].

Three types of tests are mainly used:

Sliding and corrosive test is quite similar to the pin on disk test presented in Fig. 17.47, but a container allows performing the test with lubricant or corrosive solution [Zhang T, Li DY (2001)] or both [Liu R, Li DY (1999)]. For example, 10% H₂SO₄ added to the lubricant with the volume ratio of H₂SO₄ to oil approximately equal to 1:4. It is also possible to perform simultaneously fretting wear test with an electrochemical noise (EN) measurement system, the whole system being in an electrochemical cell, as schematically shown in Fig. 17.58 [Basak AK, et al. (2006)]. Two personal computers control the systems and acquire potential, current, and friction force data. The flat samples are covered with an electrical insulating cover prior

to fretting tests leaving an area of 1 cm² exposed to the electrolyte. Corundum balls (Ceratec, The Netherlands) with a diameter of 10 mm, a hardness of 2000 HVN, and a surface roughness $R_a < 0.02 \mu\text{m}$, are used as counter body. Corundum was selected for its high wear resistance, high chemical inertness, and high electrical resistance. Fretting–corrosion experiments are performed at room temperature with a reciprocating ball-on-flat contact configuration. The flat sample is immersed in the Hank's solution for 90 min before starting up experiments in order to reach a stable potential and a low background current.

Pre-weighed samples 15 mm in diameter are fixed on a disk attached with an electric motor. The disk is isolated from the samples by painting appropriately and putting a nonconducting adhesive in between. A schematic representation of the slurry-wear test apparatus is shown in Fig. 17.59 from Prasad BK (2000). Samples are rotated at ambient temperature at a given velocity and the travel distance varies in the range of 15–500 km. Changing the content of the solid sand particles (size 212–300 μm) from 0 to 60 wt.% in the liquid electrolyte modifies the slurry composition. The electrolyte comprises 4 g sodium chloride plus 5 cc concentrated sulphuric acid dissolved in 10 L of water and has a pH of 1.98 highly acidic in nature. Addition of 20, 40, and 60 wt.% sand to the electrolyte changed the pH of the slurry mixture of liquid plus sand to 3.64, 6.85, and 7.12, respectively. Wear rate are computed by weight loss technique. Zhang D-W, Lei TC (2003) conducted a similar experiment.

In high-temperature erosion–corrosion heated fluids containing solid particles lead to material removal from the surface by a specific wear process [Stack MM, et al. (1993)]. The evolution of the weight change of the sample is represented in Fig. 17.60 [Chattopadhyay R (2001)].

Four different behaviors can be observed [Chattopadhyay R (2001), Higuera Hidalgo V, et al. (2001)]:

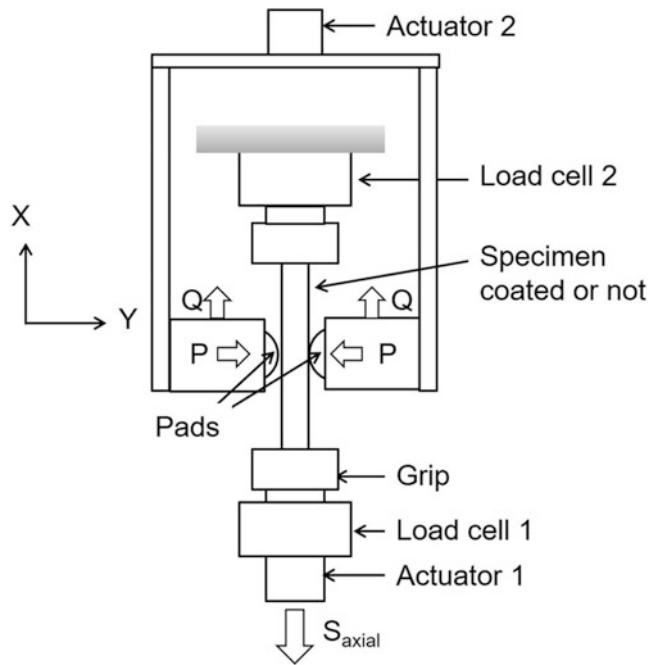


Fig. 17.62 Fretting test apparatus with a servo-hydraulic uniaxial test frame and an additional servo-hydraulic actuator [Lee H, et al. (2005)]. (Reprinted with kind permission from Springer Science Business Media)

- At low temperature, the material loss is essentially due to erosion.
- Beyond a certain temperature the rate of oxidation increases drastically with temperature. For a temperature in the mid-range, both erosion and oxide scale formation rates remain similar and the wear is erosion–corrosion dominated.
- With the further temperature increase the loss of oxide dominates and over a certain critical temperature, chipping of brittle scale is the main mechanism.
- Above the critical temperature, T_c , the overall weight change from corrosion process tends to zero.

For high temperature tests, for example to reproduce the erosion of fly ash in coal-fired boiler, fly ashes are introduced in a 210 kW laboratory combustion unit using methane as fuel (this type of combustion reproduces well that of coal). Ashes are continuously injected into the combustion chamber by means of a helicoidally feeder [Higuera Hidalgo V, et al. (2001)]. Garcia JR, et al. V (2007) have conducted a similar experiment to study the erosive–corrosive wear of Ni–Cr coatings in boilers atmosphere the high temperatures being provided by a burner using methane as fuel. During erosion wear tests, ashes retrieved from a 900 MW power plant were injected continuously into the combustion chamber by means of a helicoidally feeder, which pumped the ash into a mixing chamber where the

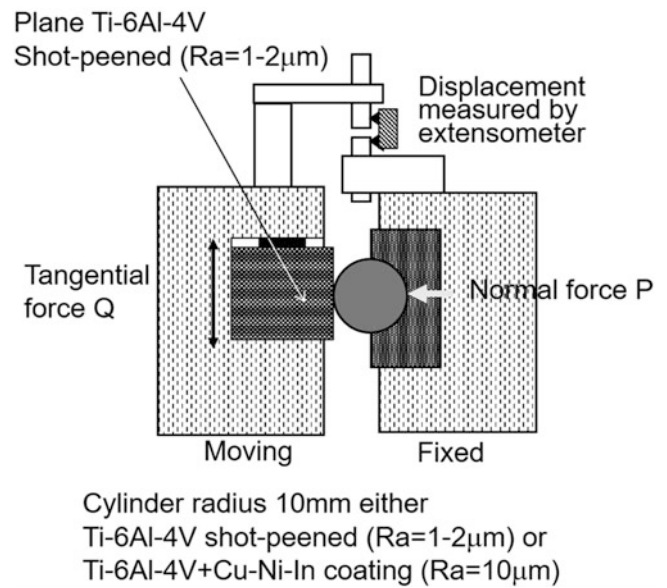


Fig. 17.63 Schematic drawing of fretting-wear rig with a tension-compression hydraulic machine [Fridrici V, et al. (2003)]. (Reprinted with kind permission from Elsevier)

ash was fluidized with air before being incorporated into the chamber. This device allows reproducing, at the laboratory scale, the same operating conditions, which exist in the areas of post-combustion gases in industrial coal-fired power plants.

Degradation of thermal barrier coatings (TBCs) in gas-turbine engines by molten calcium–magnesium–aluminosilicate (CMAS) glassy deposits is becoming a pressing issue, as engines are required to operate under increasingly harsh conditions. Drexler JM, et al. (2010) developed a new thermal-cycling test for the evaluation of TBC performance, where a thermal gradient was applied across the TBC, with simultaneous injection of CMAS. The conditions simulated in this new test are closer to actual conditions in engine, as compared to the conventional furnace test without thermal gradient. In a typical test, an equilibrated natural gas/oxygen flame heats the front of the TBC, while compressed air cools the backside (Fig. 17.61a). The front temperature (T_{sur}) is monitored using a long-wavelength (9.6–11.5 μm) pyrometer, and the substrate temperature (TTC) is monitored by a thermocouple (1 mm diameter) placed inside a hole (1.1 mm diameter, 15 mm long) drilled radially into the substrate. The bond coat temperature (T_{sub}) at the ceramic/metal interface is estimated from T_{sur} and TTC. The CMAS suspension is sprayed axially through the gas burner. The heating cycle lasts 5 min. During the cooling cycle (2 min) the cooling air nozzle is brought in front of the TBC (Fig. 17.61b), and the process is repeated.

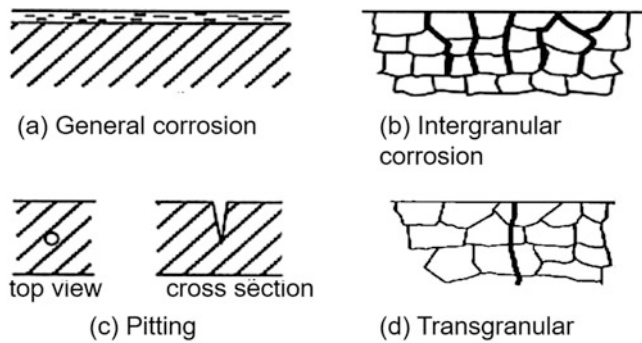


Fig. 17.64 Different types of corrosion: (a) general corrosion, (b) intergranular corrosion, (c) pitting, and (d) transgranular corrosion

17.9.6 Fretting

Fretting wear occurs when surfaces, in intimate contact with each other, are subject to a small amplitude relative motion that is cyclic in nature, such as vibration. Fretting wear is normally accompanied by the corrosion or oxidization of the debris and worn surface. If the debris become embedded in the surface of the softer metal, the wear rate may be reduced, but if the debris remain free at the interface between the two materials, the wear rate may be increased. Fatigue cracks also have a tendency to form in the region of wear. ASTM standards are presented in [17.W20–17.W22].

Figure 17.62 shows schematic of a dual actuator fretting test apparatus used by Lee H, et al. (2005) (2007). It allows conducting fretting tests with any prescribed value of relative displacement at an applied cyclic stress to the specimen. The setup comprises a servo-hydraulic uniaxial test frame and an additional servo-hydraulic actuator (actuator 2 in Fig. 17.62), which is directly connected to the fretting fixture so that independent cyclic movement of the fretting fixture is possible under a given contact load. During fretting the specimen is fatigued at a given stress level thanks to actuator 1. The tangential force, Q , depends on the difference between two load cells located at the bottom and top of the specimen. Fretting fixture can be independently controlled in either load or displacement-controlled mode through the actuator 2. The contact load, P , is applied through lateral springs and measured by a pressure gauge.

Another device used by Fridrici V, et al. (2003) is presented in Fig. 17.63. A tension-compression hydraulic machine is used to impose the displacement between the plane and the cylinder. For preselected cycle numbers during a fretting test, the displacement δ , the normal force P , and the tangential force Q are recorded. This enables to plot the fretting loop Q – δ for the preselected cycles.

Other fretting tests have been developed. They involve dove-tail geometry [Gean MC, Farris TN (2009)], the temperature of which can be monitored; a tension-compression hydraulic machine [Xu G-Z, et al. (2002)] where the coated flat specimen

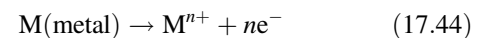
is stationary and the 52,100 steel ball is vibrated with small reciprocating amplitude; flat-on-flat wear tester designed to simulate the vibrating condition and positioned inside a furnace to obtain an operating condition of 500 °C [Koiprasert H, et al. (2004)]; and a device in which the fluctuating loading is supplied by a variable crank system [Majzooobi GH, et al. (2010)].

17.10 Corrosion Resistance

17.10.1 General Remarks

In corrosion process materials loss occurs through electro-chemical or chemical reaction with the surrounding medium. At high temperatures corrosion reactions are oxidation, carburization, nitriding, halogen erosion, sulfidation, and molten-salt corrosion [Chattopadhyay R (2001)], coatings being mainly concerned by the former and the latter.

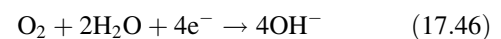
The dissolution of metallic elements by the formation of ions by electron loss corresponds to anodic reactions such as



where M is a metal, M^{n+} a positively charged n times ion, and e^{-} an electron. This electron loss allows the metal ion to bond to other groups of atoms that are negatively charged, for example, the reaction of water or oxygen with electrons from the metal surface, known as cathodic reaction. Let us consider steel rusting where water (H_2O) and oxygen (O_2) are involved:



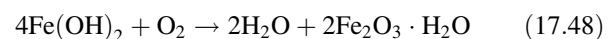
The free electrons produced react with water and oxygen:



Both reactions (17.44 and 17.45) can then be written as the global reaction:



As O_2 dissolves rapidly in water and because there is generally an excess of it, O_2 reacts with the iron hydroxide to form the hydrated iron oxide, $2Fe_2O_3 \cdot H_2O$, often called brown rust:



It is clear from these equations that the corrosion rate is linked to electrons production, corresponding to a corrosion current flow. However, the presence of an impervious oxide

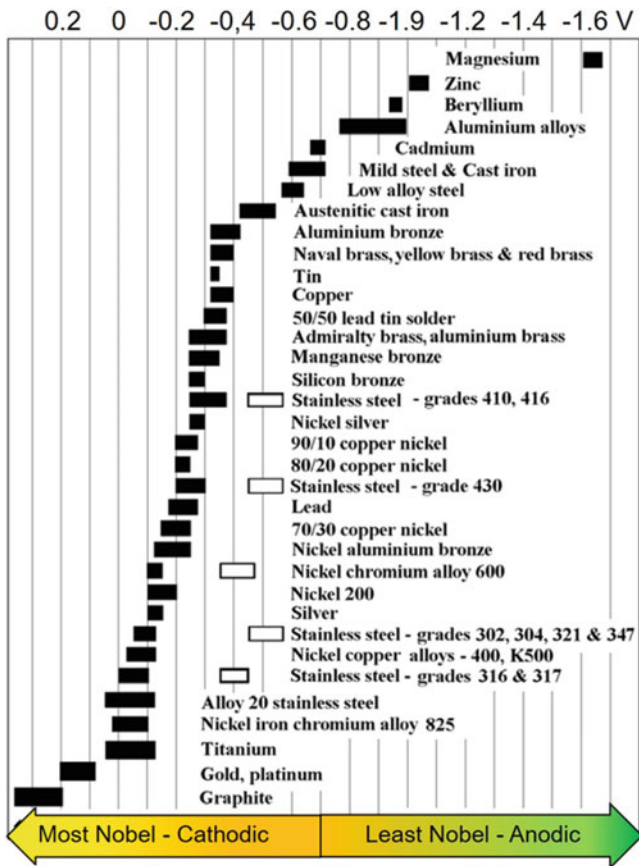


Fig. 17.65 Galvanic corrosion chart: corrosion potentials in flowing sea water at ambient temperature. The more Noble materials at the left side tend to be cathodic and hence protected; those at the right are less noble and tend to be anodic and hence corroded in a galvanic couple [Atlas Steel Technical Note No. 7]. (Reprinted with kind permission from Elsevier)

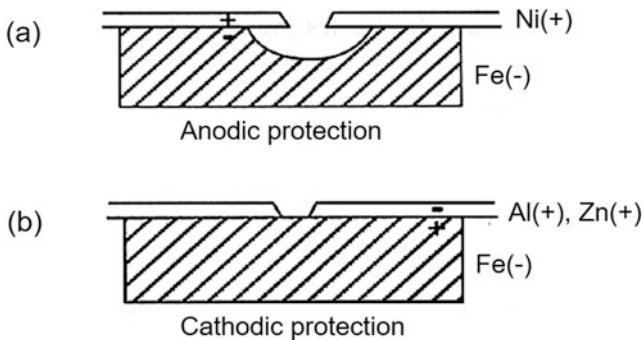


Fig. 17.66 Examples of protective coatings: (a) anodic (no discontinuity allowed in the coating) and (b) cathodic (discontinuity allowed in the coating, resulting in almost no corrosion of iron)

layer can inhibit the corrosion and the metal is said passivated.

Corrosion rate equation [Chattopadhyay R (2001)] is expressed by

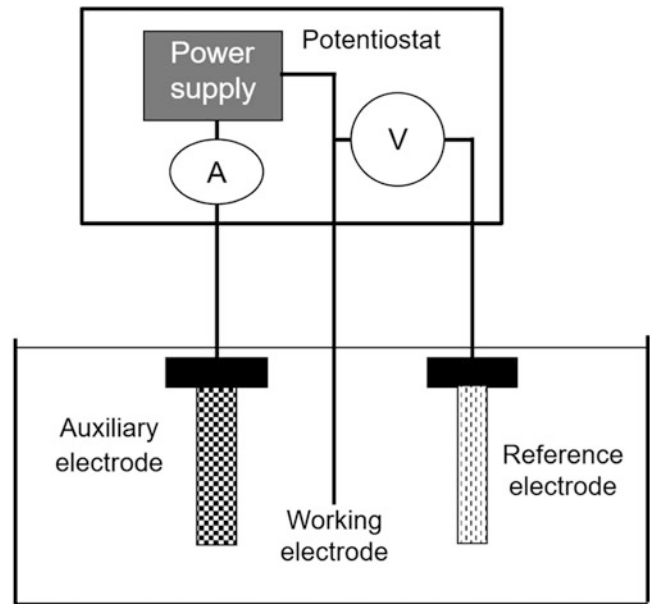


Fig. 17.67 Three-electrode cell used in the electrochemical experiments [Souza VAD, Neville A (2006)]. (Reprinted with kind permission from Springer Science Business Media, copyright © ASM International)

$$C_T = C_0 (\Delta G^*/RT) \tag{17.49}$$

where C_T is the corrosion rate at temperature $T(K)$, generally expressed in mm/year or mpy, C_0 is the rate at 0 (K), R is the ideal or universal gas constant, and ΔG^* is the activation energy of the corrosion reaction. This equation is transformed in logarithmic form, the energy terms are considered as potentials and rates as currents, resulting in a relationship between corrosion current, I_c , and measured potential, E , of the specimen:

$$E - E_c = \beta \frac{\log I}{\log I_c} \tag{17.50}$$

where E measured potential of the specimen when current flows, E_c corrosion potential (no current flowing), I impressed current, I_c corrosion current (no external current), and β a constant. This equation is used to characterize corrosion by electrochemical measurements, as described later.

The different types of corrosive attack, especially for coatings, are the following:

General corrosion, corresponding to about 30% of failure, where the average rate of corrosion on the surface is uniform as illustrated in Fig. 17.64a.

Localized corrosion, about 70% of failures, comprise of the following:

Galvanic corrosion occurring when two dissimilar metals are in contact with each other in a conductive solution (electrolyte), the more anodic metal being corroded, while the more cathodic one is unaffected. The anodic metal corrodes

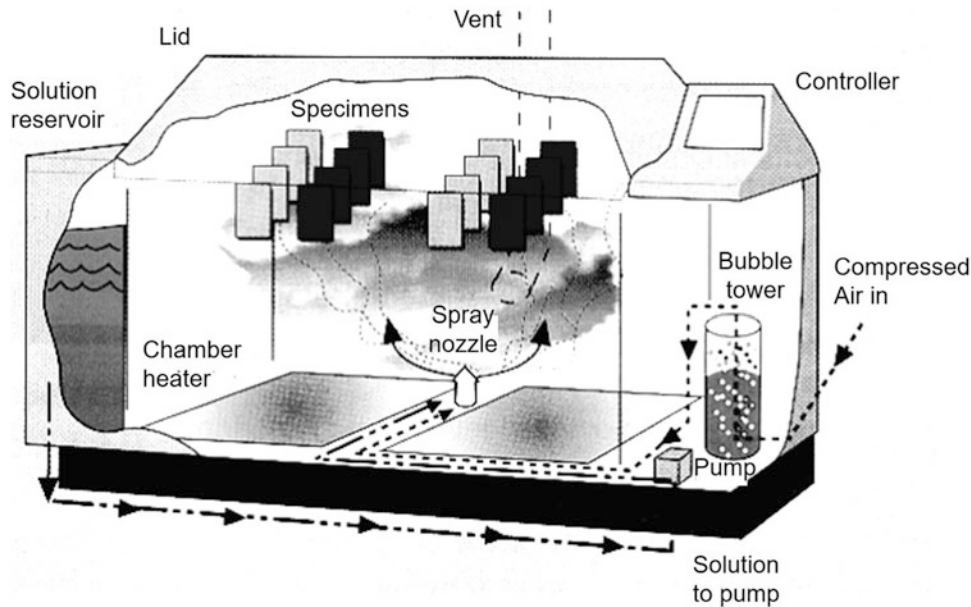


Fig. 17.68 Typical climatic enclosure [Montavon G (2004)]. (Reprinted with kind permission from Prof. G. Montavon)

faster because ions from the metal migrate from anode to cathode. There are three conditions that must exist for galvanic corrosion to occur. First there must be two electrochemically dissimilar metals present. Second, there must be an electrically conductive path between the two metals. And third, there must be a conductive path for the metal ions to move from the more anodic metal to the more cathodic metal. If any one of these three conditions do not exist, galvanic corrosion will not occur. The galvanic or electrochemical series ranks metals according to their potential, generally measured with respect to the Standard Calomel Electrode (SCE). Metals can be arranged in a galvanic series representing the potential they develop in a given electrolyte against a standard reference electrode. The relative position of two metals on such a series gives a good indication of which metal is more likely to corrode more quickly. However, other factors such as water aeration and flow rate can influence the process markedly. The results are often viewed as a galvanic corrosion chart or galvanic corrosion (Fig. 17.65).

This chart says that the “anodic” or “less noble” metals at the negative end of the series, such as magnesium, zinc, and aluminum, are more likely to be attacked than those at the “cathodic” or “noble” end of the series such as gold and graphite. For example, zinc has a negative potential higher than that of iron and it will behave as a cathode relatively to it, while nickel which negative potential is lower than that of iron will behave as an anode relatively to it. The electrolyte, ionic-conducting fluid bridging both metals, plays a key role, as well as the relative surface contact area, the smaller the anodic to cathodic area ratio is the more severe is the anodic metal corrosion. This is very important, for example, to protect low

carbon iron from atmospheric corrosion by a coating either anodic (nickel coating) or cathodic (aluminum or zinc). In the first case no discontinuity in the coating can be tolerated, while it has relatively a low importance with cathodic coating, as illustrated in Fig. 17.66. By imposing a voltage between both metals, the current direction can be changed.

Intergranular corrosion, illustrated in Fig. 17.64b, occurring when a chemical element is depleted during the coating or bulk material manufacturing, for example during heat treatment.

Pitting is a localized corrosion characterized by depression or pit formation on the surface as illustrated in Fig. 17.64c. It occurs, for example, when stainless steel is corroded by chloride-containing solutions. The pit cavities act as stress raisers.

Trans-granular corrosion is mainly due to high static tensile stress in the presence of a corrosive environment. It can be intergranular but also trans-granular when cracking occurs, as illustrated in Fig. 17.64d. Of course, the coating material and its microstructure play an important role.

17.10.2 Corrosion Characterization

For terminology and acronyms related to corruptions, see [17.C1].

17.10.2.1 Electrochemical Measurements

ASM 13A book [ASM International (2003)] and the following ASTM references [17.C2–17.C13] give a detailed description of the electrochemical techniques.

In direct current (DC) method potentiodynamic polarization is used. The coating is insulated by epoxy cold resin mounting, except a surface of about 1 cm^2 , which is exposed to a liquid electrolyte and the system is allowed to reach a near-electrochemical equilibrium. The equilibrium corroding potential, E_c , is measured relatively to a reference electrode because the absolute potential of the coating sample relatively to the electrolyte is not accessible. The value of either the anodic or cathodic current at E_c , called the corrosion current, I_c , would allow calculating the corrosion rate of the metal, but unfortunately it cannot be measured directly. Thus, additional electrodes are immersed in the solution, and all of them are connected to a device called a potentiostat that allows changing the potential of the metal sample in a controlled manner and measure the current as a function of the potential. Figure 17.67 from [Souza VAD, Neville A (2006)] presents an oversimplified scheme of the three electrodes electrochemical experiment. When the potential of a metal sample in solution is forced away from E_c , it is referred to as polarizing the sample. The response (current) of the sample is measured as it is polarized. The computer controlled potentiostat shift the potential of the working electrode (the specimen) relative to the reference electrode (often saturated calomel electrode) at a predetermined rate (a few mV/min) to potentials more positive than the free corrosion potential (E_c). The current density in the external circuit between the Pt auxiliary electrode and the coating (working electrode) is measured as a function of applied potential until a given current density is reached and then the potential drops at the same rate as on the forward curve. The response is used to develop a model of the sample's corrosion behavior. Various authors achieved similar measurements for cermets or metals either thermal sprayed [Guilemany JM, et al. (2005), Shrestha S, et al. (2001) Ishikawa Y, et al. (2005) Gobinda CS, Khan TI (2010) Paul S, Yadav K (2010) Barletta M, et al. (2010) Luiz de Assis S, et al. (2006)] or cold sprayed [Wang H-R, et al. (2008)].

AC methods are based on the fact that in presence of an electrolyte, the corroding system is equivalent to an electrical circuit comprising a resistive/capacitive (RC) parallel circuit. It is called electrochemical impedance spectroscopy (EIS). The response of the circuit (computer-driven ac impedance device) to frequencies varying from very low frequencies (10^{-2} Hz) to very high ones (10^5 Hz) allows determining the different elements of the coating equivalent electrical circuit [Wang H-R, et al. (2008)].

17.10.2.2 Fog and Salt-Spray Test

The corrosion tester is a box; for details, see [17.C14], where a corrosive solution is atomized by humidified compressed air. Air humidification is achieved by passing it through a bubble tower. The box temperature can be adjusted thanks to

heaters. In the box, also called climatic enclosure, temperature, airspeed, and relative humidity are controlled. The linear shrinkage, product mass loss or gain of treated samples, is then measured. The tests are performed either continuously or in a cyclic mode: for example, x hours with the solution followed by x hours without solution. Figure 17.68 represents a typical box.

For example, the corrosion resistance of nickel-base cored wires arc-sprayed coatings was tested by this method and by electrochemical corrosion test [He D, et al. (2007)].

17.10.2.3 Molten Salt

According to Sidhu TS, et al. (2006a, b) (2007), vanadium (V), sulfur (S), and sodium (Na) are common impurities in the low-grade petroleum fuels. Molten sulfate vanadate deposits resulting from the condensation of combustion products of such fuels are extremely corrosive to high-temperature materials in the combustion systems. Further, mixture of Na_2SO_4 and V_2O_5 in the ratio of 40:60 constitutes eutectics with a low melting point of 550°C and provides a very aggressive environment for hot corrosion to occur. They have applied uniformly a layer of Na_2SO_4 -60% V_2O_5 mixture on the warm specimens. Cyclic studies were performed in molten salt for 50 cycles. Each cycle consisted of 1-h heating at 900°C in a silicon carbide tube furnace in open air atmosphere followed by 20-min cooling at room temperature. Singh H, et al. (2005) have also studied the corrosion of Ni-base superalloy by Na_2SO_4 -60% V_2O_5 mixture in a furnace at 900°C .

Guilemany JM, et al. (2008) have tested the corrosion resistance of Ni-based coatings applied on municipal solid-waste incinerators by using a blowpipe of hot air that expels air at 650°C , and propels onto the coating drops of aqueous solution 0.05 M of a eutectic mixture KCl:ZnCl (52:48 wt.%).

Li L, et al. (2010) have studied the corrosion of TBCs by CMAS (the acronym of each oxide: CaO, MgO, Al_2O_3 , and SiO_2). The CMAS powder was synthesized as tapes of 25.4 mm diameter and glued onto the top of the coating surfaces using cement 520. The infiltration process was accomplished either in a tube furnace or through a flame burner. The coating degradation simulated in this method is similar to reports from field studies of aircraft engines.

17.10.2.4 Oxidation

Matthews S, et al. (2010) have followed the oxidation of Cr_3C_2 -NiCr coatings heat treated at 900°C in still air during different numbers of days. Ye F-X, et al. (2008) performed a similar work on Cr39Ni7C cermet coatings deposited by Diamond jet spray process. For details about oxidation test, see [15.C15].

17.11 Summary and Conclusions

Sprayed coating characterization is very important. However, the needs of research laboratories, often working on relatively small samples, are not at all the same as those of industry working with real part geometry. In laboratories the interest is mostly in the characterization of coating phases, microstructure, and more recently nanostructure, unmolten particles, voids, and cracks distributions, coating–substrate interface or splat interfaces, which are parameters not directly linked to the properties desired by industry in a production scale environment. On the other hand, in the context of a production scale operation, the main interest is measurement of the part geometry after spraying and machining, coating thickness, adhesion/cohesion, hardness, stiffness, Young’s modulus, thermal conductivity, and diffusivity.

In both cases, however, the measurement will require using statistical methods that must be carefully achieved to limit the errors to human ones. The dream in production would be that all measurements could be achieved by nondestructive methods. All these measurements impact the reproducibility and reliability of thermal-sprayed coating production. Thus, the measurement uncertainty must be controlled carefully, and statistics used properly while leaving room to detect and accommodate human factor still remains important in coating quality control [Wigren J, Johansson J (2011)].

Nomenclature

Units are indicated in parentheses; when no units are indicated, the parameter is dimensionless.

Latin Alphabet

a	Thermal diffusivity (m^2/s)
a_c	Half-diagonal crack length (μm)
a_k	Crack length (m)
A	Area (m^2)
A_w	Area of contact (m^2)
B	Thickness (m)
c_f	Correction factor related to the shape of the indenter
c_p	Specific heat at constant pressure (J/K kg)
C	Compliance: ratio of the displacement to the load (m/N)
C_T	Corrosion rate at temperature T (mm/year or mpy)
d	Equivalent or inside diameter (m)
d_0	“Stress-free” lattice parameter (nm)
d_{hkl}	Distance between atomic layers with the same Miller indices (h, k, l)
d_w	Sliding distance (m)
D	Outside diameter of the bar (m)
e	Sample thickness (m)
E	Energy (J) or (eV)
E'	Young’s modulus (GPa)
E'_c	Young’s modulus of the coating (GPa)
E'_s	Young’s modulus of the substrate (GPa)
E_c	Corrosion potential (mV)

F	Force applied (N)
$f(\alpha)$	A function of the impingement angle α (—)
F_N	Applied normal force (N)
G_c	Critical value of the strain energy release rate (J/m^2)
h	Penetration depth of an indenter (μm)
H	Hardness or yield stress (MPa)
h_{max}	Penetration depth (μm)
h_p	Plastic component of penetration depth of an indenter (μm)
h_r	Residual depth of the residual deformation once the indenter is removed (μm)
HV_x	Hardness measured with a load of ‘ x ’ Newton
I	Impressed current (mA)
I_c	Corrosion current (no external current) (mA)
k	Wave vector of the incident neutron beam
K	Strain energy release rate (related to the fracture toughness) ($\text{N}/\text{m}^{3/2}$)
k_o	Wave vector of the scattered neutron beam
K_{adh}	Adhesion wear coefficient $K_{\text{adh}} = K_w/3$ (—)
K_c	Fracture toughness ($\text{N}/\text{m}^{3/2}$)
K_{ca}	Apparent interface fracture toughness ($\text{N}/\text{m}^{3/2}$)
K_w	Wear coefficient (—)
l	Length of the coating (m)
L	Length scale (m)
l_c	Palmqvist surface crack length (μm)
m	Shape parameter in Weibull distribution
p	Pressure (Pa)
P	Force required extending a crack (N)
P_c	Applied load (N) on an indenter
P_{max}	Maximum load on an indenter (N)
q	Scattering vector
q	Modulus of scattering vector
Q	Imposed gas flow (m^3/s)
S	Slope of the initial part of the unloading curve (—)
U	Elastic energy stored in the system (J)
V	Volume (m^3)
V_b	Coating bulk volume (m^3)
V_p	Open pores volume (m^3)
V_w	Wear volume (m^3)
w	Coating thickness (μm)
w_{dry}	The dried coating weight (kg)
w_{sat}	The wet coating weight (kg)
w_{wd}	Weight of water displaced (kg)
W	Total work (J)
W_e	Work done by external forces (J) or elastic work (J)
x_i	Measured value of indent, hardness, Young’s module ...

Greek Alphabet

α	Impingement angle ($^\circ$)
φ	Angle with respect to the normal to the substrate surface ($^\circ$)
ϕ	Phase angle
γ	Surface tension (J/m^2 or N/m)
η	Arithmetic mean of the sample of N events
κ	Thermal conductivity ($\text{W}/\text{m K}$)
μ	Viscosity (Pa.s)
λ	Wavelength (nm)
ν	Poisson’s ratio
θ	Angle of incidence
ρ	Mass density (kg/m^3)
σ	Standard deviation
$\rho(r)$	Scattering length density
ϕ_a	Apparent porosity (%)
τ_c	Critical shear stress (MPa)
κ_e	Electronic conduction ($\text{W}/\text{m K}$)

σ_f	Fracture stress (MPa)
ΔG^*	Activation energy of the corrosion reaction (J)
ε_{hkl}	Lattice strain (–)
α_L	Linear expansion coefficient (K^{-1})
κ_c	Thermal conductivity of the coating (W/m.K)
κ_{Ph}	Lattice conduction or phonon conduction (W/m.K)
α_V	Volumetric expansion coefficients
δ_w	Depth of wear (μm)
ρ_X	Specific mass or mass density of X (kg/m^3)
Δp	Pressure drop (Pa)

ASTM Standards

A.1: Adhesion–Cohesion

[17.A1] **ASTM C633** Revision/Edition: 01 Chg: W/REAP
Date: 00/00/08 Standard test method for adhesion or cohesion strength of thermal spray coatings

A.2: Corrosion

- [17.C1] **ASTM G193** Revision/Edition: 10B Chg: Date: 06/01/10 Standard terminology and acronyms relating to corrosion
- [17.C2] **ASTM 03.02** Revision/Edition: 10 Chg: Date: 08/00/10 Corrosion of metals; Wear and corrosion
- [17.C3] **ASTM G102** Revision/Edition: 89 Standard practice for calculation of corrosion rates and related information from electrochemical measurements
- [17.C4] **ASTM G3** Revision/Edition: 89 Standard practice for conventions applicable to electrochemical measurements in corrosion testing
- [17.C5] **BS EN ISO 17475** Revision/Edition: 06 Corrosion of metals and alloys—Electrochemical test methods—Guidelines for conducting potentiostatic and potentiodynamic polarization measurements
- [17.C6] **ASTM G5** Revision/Edition: 94 Chg: W/REAP
Date: 00/00/04 Standard reference test method for making potentiostatic and potentiodynamic anodic polarization measurements
- [15.C7] **ASTM G59** Revision/Edition: 97 Chg: W/REAP
Date: 00/00/09 Standard test method for conducting polarization resistance measurements
- [17.C8] **ASTM G61** Revision/Edition: 86 Chg: W/REAP
Date: 00/00/09 Standard test method for conducting cyclic potentiodynamic polarization measurements for localized corrosion susceptibility of iron-, nickel-, or cobalt-based alloys
- [17.C9] **ASTM G102** Revision/Edition: 89 Chg: W/REAP
Date: 00/00/10 Standard practice for calculation of corrosion rates and related information from electrochemical measurements

- [17.C10] **ASTM G106** Revision/Edition: 89 Chg: W/REAP
Date: 00/00/10 Standard practice for verification of algorithm and equipment for electrochemical impedance measurements
- [17.C11] **SEMI F77** Revision/Edition: 03 Chg: W/REAP
Date: 03/00/10 Test method for electrochemical critical pitting temperature testing of alloy surfaces used in corrosive gas systems
- [17.C12] **ASTM G150** Revision/Edition: 99 Chg: W/REAP
Date: 00/00/10 Standard test method for electrochemical critical pitting temperature testing of stainless steels
- [17.C13] **ASTM G78** Revision/Edition: 01 Chg: W/REAP
Date: 00/00/07 Standard guide for crevice corrosion testing of iron-base stainless alloys in seawater and other chloride-containing aqueous environments
- [17.C14] **ASTM B117** Revision/Edition: 09 Chg: Date: 07/01/09 Standard practice for operating salt spray (fog) apparatus
- [17.C15] **ISO DIS 21608** Revision/Edition: 10 Chg: Date: 10/29/10 Corrosion of metals and alloys—Test method for isothermal-exposure oxidation testing under high-temperature corrosion conditions for metallic materials.

A.3: Mechanical Properties

- [17.M1] **ASTM 03.01** Revision/Edition: 10 Chg: Date: 07/00/10 Metals-mechanical testing; elevated and low-temperature tests; Metallography
- [17.M2] **ASM METALS HDBK V8** Revision/Edition: 00 Chg: Date: 00/00/00 Mechanical testing and evaluation
- [17.M3] **ASTM E6** Revision/Edition: 09B Chg: Date: 05/15/09 Standard terminology relating to methods of mechanical testing
- [17.M4] **BS 7134 P4 S4.2** Revision/Edition: 90 Chg: REAF
Date: 00/00/96 Testing of engineering ceramics—thermo-mechanical properties—method for determination of thermal diffusivity by the laser flash (or heat pulse) method
- [17.M5] **ASTM A833** Revision/Edition: 08A Chg: Date: 11/01/08 Standard practice for indentation hardness of metallic materials by comparison hardness testers
- [17.M6] **ASTM C1327** Revision/Edition: 08 Chg: Date: 08/01/08 Standard test method for Vickers indentation hardness of advanced ceramics
- [17.M7] **ASTM E384** Revision/Edition: 10 Chg: W/E2 Date: 04/00/10 Standard test method for Knoop and Vickers hardness of materials
- [17.M8] **ASTM C1326** Revision/Edition: 08 Chg: W/E1
Date: 09/00/08 Standard test method for Knoop indentation hardness of advanced ceramics
- [17.M9] **ASTM C1327-08** Standard test method for Vickers indentation hardness of advanced ceramics

- [17.M10] **BS 5600 P4 S4.7** Revision/Edition: 79 Chg: Date: 00/00/79 Determination of the Young's modulus
- [17.M11] **JIS Z 2280** Revision/Edition: 93 Chg: W/REAF Date: 10/01/08 Test method for Young's modulus of metallic materials at elevated temperature
- [17.M12] **BS DD CEN/TS 1071-7** Revision/Edition: 03 Chg: Date: 10/16/03 Advanced technical ceramics—Methods of test for ceramic coatings—Part 7: Determination of hardness and Young's modulus by instrumented indentation testing
- [17.M12] **ASTM C1198** Revision/Edition: 09 Chg: Date: 11/04/09 Standard test method for dynamic Young's modulus, shear modulus and Poisson's ratio for advanced ceramics by sonic resonance
- [17.M13] **ASTM C1259** Revision/Edition: 08 Chg: W/E1 Date: 04/00/09 Standard test method for dynamic Young's modulus, shear modulus and Poisson's ratio for advanced ceramics by impulse excitation of vibration
- [17.M14] **API TR 6 AM** Revision/Edition: 2 Chg: W/REAF Date: 01/00/03 Material toughness
- [17.M15] **ASTM C1421** Revision/Edition: 09 Chg: Date: 05/01/09 Standard test methods for determination of fracture toughness of advanced ceramics at ambient temperature
- [17.M16] **BS 7448-1** Revision/Edition: 91 Chg: W/REAF Date: 03/00/07 Fracture mechanics toughness tests—Part 1: Method for determination of K_{1c}, critical CTOD and critical J values of metallic materials
- [17.M17] **BS EN ISO 12737** Revision/Edition: 06 Chg: Date: 01/12/06 Metallic materials—Determination of plane-strain fracture toughness
- [17.M18] **BS ISO 28079** Revision/Edition: 09 Chg: Date: 08/31/09 Hardmetals—Palmquist toughness test
- [17.M19] **ASTM STP381** Revision/Edition: 65 Chg: Date: 00/00/65 Fracture toughness testing and its applications
- [17.M20] **BS EN 15305** Revision/Edition: 08 Chg: W/CRGD Date: 06/30/09 Non-destructive testing—Standard test method for determining residual stress analysis by X-ray diffraction
- [17.M21] **BS DD CEN ISO/TS 21432** Revision/Edition: 06 Chg: W/REAF Date: 12/01/08 Non-destructive testing—Standard test method for determining residual stresses by neutron diffraction.
- [17.Ma2] **BS EN 13925-1** Revision/Edition: 03 Chg: W/REAF Date: 12/01/08 Non-destructive testing—X-ray diffraction from polycrystalline and amorphous materials—Part 1: General principles
- [17.Ma3] **BS EN 13925-2** Revision/Edition: 03 Chg: W/REAF Date: 12/01/08 Non-destructive testing—X-ray diffraction from polycrystalline and amorphous materials—Part 2: Procedures
- [17.Ma4] **NBS MONO 25 SEC 16** Revision/Edition: 79 Chg: Date: 10/00/79 Standard X-ray diffraction powder patterns
- [17.Ma5] **ASTM F2024** Revision/Edition: 10 Chg: REIN Date: 06/00/10 Standard practice for X-ray diffraction determination of phase content of plasma-sprayed hydroxyapatite coatings
- [17.Ma6] **BS ISO 17470** Revision/Edition: 04 Chg: W/REAF Date: 12/01/08 Microbeam analysis—electron probe microanalysis—Guidelines for qualitative point analysis by wavelength dispersive X-ray spectrometry
- [17.Ma7] **BS ISO 18516** Revision/Edition: 06 Chg: W/REAF Date: 06/01/10 Surface chemical analysis—Auger electron spectroscopy and X-ray photoelectron spectroscopy—Determination of lateral resolution
- [17.Ma8] **AS ISO 15470** Revision/Edition: 06 Chg: Date: 10/20/06 Surface chemical analysis—X-ray photoelectron spectroscopy—description of selected instrumental performance parameters
- [17.Ma9] **BS ISO 10810** Revision/Edition: 10 Chg: Date: 12/31/10 Surface chemical analysis—X-ray photoelectron spectroscopy—guidelines for analysis
- [17.Ma10] **BS ISO 15470** Revision/Edition: 05 Chg: W/REAF Date: 10/01/10 Surface chemical analysis—X-ray photoelectron spectroscopy—description of selected performance parameters

A.4: Materials Characterization

- [17.Ma1] **ASTM E204** Revision/Edition: 98 Chg: W/REAF Date: 00/00/07 Standard practices for identification of materials by infrared absorption spectroscopy, using the ASTM coded band and chemical classification index

A.5: Metallography and Image Analysis

- [17. Me1] **ASTM E1920** Revision/Edition: 03 Chg: W/REAF Date: 00/00/08 Standard guide for metallographic preparation of thermal sprayed coatings
- [17. Me2] **ASTM E3** Revision/Edition: 01 Chg: W/E1 Date: 03/00/09 Guide for metallographic preparation of metallographic specimens
- [17. Me3] **ASTM MNL46** Revision/Edition: 07 Chg: Date: 00/00/07 Metallographic and materialographic specimen preparation light microscopy, image analysis and hardness testing

A.6: Non-destructive Methods

[17.ND1] **ESDU 91027** Revision/Edition: 91 Chg: W/AA
Date: 11/01/93 Non-destructive examination—Choice of methods

A.7: Statistical Methods

[17.S1] **ASTM C1239-07** Revises ASTM C1239-06a Standard practice for reporting uniaxial strength data and estimating Weibull distribution parameters for advanced ceramics

A.8: Thermal Properties

- [17.T1] **ASTM E228** Revision/Edition: 06 Chg: W/REIN
Date: 09/01/06 Standard test method for linear thermal expansion of solid materials with a push-rod dilatometer
- [17.T2] **ASTM E289** Revision/Edition: 04 Chg: W/REAP
Date: 00/00/10 Standard test method for linear thermal expansion of rigid solids with interferometry
- [17.T3] **ASTM C177** Revision/Edition: 10 Chg: Date: 06/01/10 Standard test method for steady-state heat flux measurements and thermal transmission properties by means of the guarded-hot-plate apparatus
- [17.T4] **ASTM C201-93** (2009) Standard test method for thermal conductivity of refractories
- [17.T5] **ASTM E 1461** Revision/Edition: 07 Chg: Date: 11/01/07 Standard test method for thermal diffusivity of solids by the flash method Disk 6–12 mm diameter; 1.5–4 mm thick diffusivity 0.1–1000 m²/s
- [17.T6] **ASTM C 714** Revision/Edition: 05 Chg: W/REAP
Date: 00/00/10 Standard test method for thermal diffusivity of carbon and graphite by a thermal pulse method; 6–12 mm, 2–4 mm thick; 0.04–2.0 cm²/s
- [17.T7] **ASTM C 1470-06** Standard guide for testing the thermal properties of advanced ceramics
- [17.T8] **BS 7134 P4 S4.2** Revision/Edition: 90 Chg: REAF
Date: 00/00/96 Testing of engineering ceramics—thermo-mechanical properties—method for determination of thermal diffusivity by the laser flash (or heat pulse) method
- [17.T9] **ASTM D2766-95(2009)** Standard test method for specific heat of liquids and solids
- [17.T10] **ASTM E1269-11** Standard test method for determining specific heat capacity by differential scanning calorimetry
- [17.T11] **ASTM C1525** Revision/Edition: 04 Chg: W/REAP
Date: 00/00/09 Standard test method for determination of thermal shock resistance for advanced ceramics by water quenching

- [17.T12] **FORD FLTM BI 107-05** Revision/Edition: 09 Chg: Date: 02/03/09 Thermal shock for coating adhesion
- [17.T13] **JDQ149** Revision/Edition: 02 Chg: Date: 06/27/02 Tests for thermal shock resistance of high temperature coatings
- [17.T14] **ASTM C 1171-05** Standard test method for quantitatively measuring the effect of thermal shock and thermal cycling on refractories
- [17.T15] **ISO DIS 13123** Revision/Edition: 10 Chg: Date: 07/22/10 Metallic and other inorganic coatings—Test method of cyclic heating for thermal barrier coatings under temperature gradient.

A.9: Void Content and Network Architecture

[17.V1] **E2109-01(2007)** Standard test methods for determining area percentage porosity in thermal sprayed coatings

A.10: Wear

- [17.W1] **ASTM G40** Revision/Edition: 10A Chg: Date: 07/01/10 Standard terminology relating to wear and erosion
- [17.W2] **ASTM C704/C704M** Revision/Edition: 09 Chg: W/E1 Date: 08/00/09 Standard test method for abrasion, resistance of refractory materials at room temperature
- [17.W3] **ASTM G105** Revision/Edition: 02 Chg: W/REAP
Date: 00/00/07 Standard test method for conducting wet sand/rubber wheel abrasion test
- [17.W4] **ASTM G132** Revision/Edition: 96 Chg: W/REAP
Date: 00/00/07 Standard test method for pin abrasion testing
- [17.W5] **ASTM G65** Revision/Edition: 04 Chg: Date: 11/01/04 10 Standard test method for measuring abrasion using the dry sand/rubber wheel apparatus
- [17.W6] **ASTM MNL56** Revision/Edition: 07 Chg: Date: 00/00/07 Guide to friction, wear, and erosion testing
- [17.W7] **ASTM G99** Revision/Edition: 05 Chg: W/REAP
Date: 00/00/10 Standard test method for wear testing with a pin-on-disk apparatus
- [17.W8] **ASTM G133** Revision/Edition: 05 Chg: W/REAP
Date: 00/00/10 Standard test method for linearly reciprocating ball-on-disk sliding wear
- [17.W9] **ASTM G98** Revision/Edition: 09 Chg: Date: 10/01/09 Standard test method for galling resistance of materials
- [17.W10] **ASTM G73** Revision/Edition: 10 Chg: Date: 04/01/10 Standard test method for liquid impingement erosion using rotating apparatus

- [17.W11] **ASTM G134** Revision/Edition: 95 Chg: W/REAP Date: 00/00/06 Standard test method for erosion of solid materials by a cavitating liquid jet
- [17.W12] **ASTM G32** Revision/Edition: 09 Chg: Date: 05/01/09 Standard test method for cavitation erosion using vibratory apparatus
- [17.W13] **ASTM E1942** Revision/Edition: 98 Chg: W/REAP Date: 00/00/04 Standard guide for evaluating data acquisition systems used in cyclic fatigue and fracture mechanisms
- [17.W14] **ASTM E2368** Revision/Edition: 10 Chg: Date: 05/01/10 Standard practice for strain controlled thermomechanical fatigue testing
- [17.W15] **BS 3518-1** Revision/Edition: 93 Chg: W/REAP Date: 01/01/09 Methods of fatigue testing—Part 1: Guide to general principles
- [17.W16] **BS 3518-2** Revision/Edition: 62 Chg: W/REAP Date: 01/01/09 Methods of fatigue testing—Part 2: Rotating bending fatigue tests
- [17.W17] **BS 3518-3** Revision/Edition: 63 Chg: W/REAP Date: 01/01/09 Methods of fatigue testing—Part 3: Direct stress fatigue tests
- [17.W18] **ASTM G119** Revision/Edition: 09 Chg: Date: 07/15/09 Standard guide for determining synergism between wear and corrosion
- [17.W19] **ASTM 03.02** Revision/Edition: 10 Chg: Date: 08/00/10 Corrosion of metals; Wear and corrosion
- [17.W20] **ASTM G204** Revision/Edition: 10 Chg: Date: 04/01/10 Standard test method for damage to contacting solid surfaces under fretting conditions
- [17.W21] **ASTM STP1159** Revision/Edition: 92 Chg: Date: 00/00/92 Standardization of fretting fatigue test methods and equipment
- [17.W22] **ASTM STP1367** Revision/Edition: 00 Chg: Date: 02/00/00 Fretting fatigue: current technology and practices
- Allen, A.J., J. Ilavsky, G.G. Long, J.S. Wallace, C.C. Berndt, and H. Herman. 2001b. Micro structural characterization of yttria-stabilized zirconia plasma-sprayed deposits using multiple small-angle neutron scattering. *Acta Materialia* 49: 1661–1675.
- Amada, S., and T. Hirose. 1998. Influence of grit blasting pre-treatment on the adhesion strength of plasma sprayed coatings: Fractal analysis of roughness. *Surface and Coating Technology* 102: 132–137.
- Anderson, P.S., X. Wang, and P. Xiao. 2004. Impedance spectroscopy study of plasma sprayed and EB-PVD thermal barrier coatings. *Surface and Coating Technology* 185: 106–119.
- Andreola, F., C. Leonelli, M. Romagnoli, and P. Miselli. 2000. Techniques used to determine porosity. *American Ceramic Society Bulletin* 79 (7): 49–52.
- Andrews, D.J., and J.A.T. Taylor. 2000. Quality control of thermal barrier coatings using acoustic emission. *Journal of Thermal Spray Technology* 9 (2): 181–190.
- Antou, G., and G. Montavon. 2007. Quantifying thermal spray coating architecture by stereological protocols: Part II. Key points to be addressed. *Journal of Thermal Spray Technology* 16 (2): 168–176.
- Antou, G., G. Montavon, F. Hlawka, A. Cornet, C. Coddet, and F. Machi. 2004a. Evaluation of modifications induced on pore network and structure of partially stabilized zirconia manufactured by hybrid plasma spray process. *Surface and Coating Technology* 180–181: 627–632.
- Antou, G., G. Montavon, F. Hlawka, A. Cornet, and C. Coddet. 2004b. Characterizations of the pore-crack network architecture of thermal-sprayed coatings. *Materials Characterization* 53: 361–372.
- . 2006. Exploring thermal spray gray alumina coating pore network architecture by combining stereological protocols and impedance electrochemical spectroscopy. *Journal of Thermal Spray Technology* 15 (4): 765–772.
- ASM International. 2003. Corrosion: Fundamentals, testing, and protection. In *ASM handbook*, vol. 13A, 509–513. Materials Park: ASM International.
- . 2007. *ASM handbook: Nondestructive evaluation and quality control*, vol. 17, 9th ed. Materials Park: ASM International.
- . 2008. *ASM handbook, Materials characterization*, vol. 10, 8th ed. Materials Park: ASM International
- Asmani, M., C. Kermel, A. Leriche, and M. Ourak. 2001. Influence of porosity on Young's modulus and Poisson's ratio in alumina ceramics. *Journal of the European Ceramic Society* 21: 1081–1086.
- Atlas Steel Technical Note No. 7 "Galvanic corrosion," revised August 2010.
- Baba, T., and A. Ono. 2001. Improvement of the laser flash method to reduce uncertainty in thermal diffusivity measurements. *Measurement Science and Technology* 12: 2046–2057.
- Bacciocchini, A., J. Ilavsky, G. Montavon, A. Denoirjean, F. Ben-ettouil, S. Valette, P. Fauchais, and K. Wittmann-Teneze. 2010a. Quantification of void network architectures of suspension plasma-sprayed (SPS) yttria-stabilized zirconia (YSZ) coatings using ultra-small-angle X-ray scattering (USAXS). *Materials Science and Engineering A* 528: 91–102.
- Bacciocchini, A., G. Montavon, J. Ilavsky, A. Denoirjean, and P. Fauchais. 2010b. Porous architecture of SPS thick YSZ coatings structured at the nanometer scale (50 nm). *Journal of Thermal Spray Technology* 19 (1–2): 198–206.
- Bahbou, M.F., P. Nylén, and J. Wigren. 2004. Effect of grit blasting and spraying angle on the adhesion strength of a plasma-sprayed coating. *Journal of Thermal Spray Technology* 13 (4): 508–514.
- Balykov, A.V. 2006. Main conditions for efficient drilling of holes in brittle nonmetallic materials using diamonds drills. *Material Processing* 63 (5–6): 161–165.
- Barletta, M., G. Bolelli, B. Bonferroni, and L. Lusvardi. 2010. Wear and corrosion behavior of HVOF-sprayed WC-CoCr coatings on Al alloys. *Journal of Thermal Spray Technology* 19 (1–2): 358–367.

References

- Agüero, A., F. Camón, J. García de Blas, J.C. del Hoyo, R. Muelas, A. Santaballa, S. Ulargui, and P. Vallés. 2011. HVOF-deposited WCCoCr as replacement for hard Cr in landing gear actuators. *Journal of Thermal Spray Technology* 20 (6): 1292–1309.
- Ahmed, R., and M. Hadfield. 2002. Mechanisms of fatigue failure in thermal spray coatings. *Journal of Thermal Spray Technology* 11 (3): 334–349.
- Aksel, C., and P.D. Warren. 2003. Thermal shock parameters [R, R''' and R'''] of magnesia–spinel composites. *Journal of the European Ceramic Society* 23: 301–308.
- Allen, A.J., G.G. Long, H. Boukari, J. Ilavsky, A. Kulkarni, S. Sampath, H. Herman, and A.N. Goland. 2001a. Microstructural characterization studies to relate the properties of thermal spray coatings to feedstock and spray conditions. *Surface and Coating Technology* 146–147: 544–552.

- Barradas, S., F. Borit, V. Guipont, M. Jeandin, C. Bolis, M. Boustie, and L. Berthe. 2002. Laser shock flier impact simulation of particle-substrate interactions in cold spray. In *ITSC-2002*, ed. E. Lugscheider and C.C. Berndt, 592–597. Düsseldorf: DVS Deutscher Verband für Schweißen.
- Barradas, S., R. Molins, M. Jeandin, M. Arrigoni, M. Boustie, C. Bolis, L. Berthe, and M. Ducos. 2005. Application of laser shock adhesion testing to the study of the interlamellar strength and coating-substrate adhesion in cold-sprayed copper coating of aluminum. *Surface and Coating Technology* 197: 18–27.
- Basak, A.K., P. Matteazzi, M. Vardavoulias, and J.-P. Celis. 2006. Corrosion-wear behaviour of thermal sprayed nanostructured FeCu/WC-Co coatings. *Wear* 261: 1042–1050.
- Beghini, M., L. Bertini, and E. Frendo. 2001a. Measurement of coatings' elastic properties by mechanical methods: Part 1. Consideration on experimental errors. *Experimental Mechanics* 41 (4): 293–304.
- Beghini, M., G. Benamati, L. Bertini, and F. Frendo. 2001b. Measurement of coatings' elastic properties by mechanical methods: Part 2. Application to thermal barrier coatings. *Experimental Mechanics* 41 (4): 305–311.
- Berka, L., and N. Murafa. 2004. On the estimation of the toughness of surface microcracks. *International Journal of Fracture* 128: 115–120.
- Berndt, C.C. 1985. Acoustic emission evaluation of plasma-sprayed thermal barrier coatings. *Journal of Engineering for Gas Turbines and Power* 107: 142–146.
- Berndt, C.C., and R. McPherson. 1981. A fracture mechanics approach to the adhesion of flame and plasma sprayed coatings. *Transaction of the Institute of Engineers* 6 (4): 53–58.
- Białucki, P., and S. Kozerski. 2006. Study of adhesion of different plasma-sprayed coatings to aluminium. *Surface and Coating Technology* 201: 2061–2064.
- Bobzin, K., N. Kopp, T. Warda, and M. Öte. 2012. Determination of the effective properties of thermal spray coatings using 2-D and 3-D models. *Journal of Thermal Spray Technology*. <https://doi.org/10.1007/s11666-012-9809-3>.
- Boccaccini, D.N., and A.R. Boccaccini. 1997. Dependence of ultrasonic velocity on porosity and pore shape in sintered materials. *Journal of Nondestructive Evaluation* 16 (4): 187–192.
- Bolcavage, A., A. Feuerstein, J. Foster, and P. Moore. 2004. Thermal shock testing of thermal barrier coating/bondcoat systems. *Journal of Materials Engineering and Performance* 13 (4): 389–397.
- Bolelli, G., V. Cannillo, L. Lusvardi, and T. Manfredini. 2006. Wear behaviour of thermally sprayed ceramic oxide coatings. *Wear* 261: 1298–1315.
- Bolelli, G., L. Lusvardi, T. Varis, E. Turunen, M. Leoni, P. Scardi, C.L. Azanza-Ricardo, and M. Barletta. 2008. Residual stresses in HVOF-sprayed ceramic coatings. *Surface and Coating Technology* 202: 4810–4819.
- Bolelli, G., J. Rauch, V. Cannillo, A. Killinger, L. Lusvardi, and R. Gadow. 2009. Microstructural and tribological investigation of high-velocity suspension flame sprayed (HVSFS) Al₂O₃ coatings. *Journal of Thermal Spray Technology* 18 (1): 35–49.
- Bolis, C., et al. 2002. Developments in laser shock adhesion test (LASAT). In *ITSC-2002*, ed. E. Lugscheider et al., 587–593. Materials Park: ASM International.
- Bolot, R., G. Antou, G. Montavon, and C. Coddet. 2005. A two-dimensional heat transfer model for thermal barrier coating average thermal conductivity computation. *Numerical Heat Transfer, Part A: Applications* 47 (9): 875–898.
- Bolot, R., J.-L. Seichepine, J. Hao Qiao, and C. Coddet. 2011. Predicting the thermal conductivity of AlSi/polyester abrasible coatings: Effects of the numerical method. *Journal of Thermal Spray Technology* 20 (1–2): 39–47.
- Bradai, M.A., M. Braccini, A. Ati, N. Bounar, and A. Benabbas. 2008. Microstructure and adhesion of 100Cr6 steel coatings thermally sprayed on a 35CrMo4 steel substrate. *Surface and Coating Technology* 202: 4538–4543.
- Brousse, E. 2010. Elaboration by thermal spraying of finely structured elements of a high temperature electrolyser for hydrogen production: Processes, structures and characteristics. PhD thesis, University of Limoges, France (in French).
- Bucaille, J.L., E. Felder, and G. Hochstetter. 2002. Identification of the viscoplastic behavior of a polycarbonate based on experiments and numerical modeling of the nano-indentation test. *Journal of Materials Science* 37: 3999–4011.
- Bunker, G. 2010. *Introduction to XAFS: A practical guide to X-ray absorption fine structure spectroscopy*. Cambridge: Cambridge University Press.
- Cernuschi, F., L. Lorenzoni, S. Ahmaniemi, P. Vuoristo, and T. Mäntylä. 2005. Studies of the sintering kinetics of thick thermal barrier coatings by thermal diffusivity measurements. *Journal of the European Ceramic Society* 25: 393–400.
- Chandler, H., ed. 2004. *Hardness testing*, 2nd ed. Materials Park: ASM.
- Chandra, S., and P. Fauchais. 2009. Formation of solid splats during thermal spray deposition. *Journal of Thermal Spray Technology* 18 (2): 148–180.
- Chattopadhyay, R. 2001. *Surface wear: Analysis, treatment, and prevention*, 307 p. Materials Park: ASM International.
- Chen, H., Y. Hao, H. Wang, and W. Tang. 2010. Analysis of the microstructure and thermal shock resistance of laser glazed nanostructured zirconia TBCs. *Journal of Thermal Spray Technology* 19 (3): 558–565.
- Chi, W., S. Sampath, and H. Wange. 2006. Ambient and high-temperature thermal conductivity of thermal sprayed coatings. *Journal of Thermal Spray Technology* 15 (4): 773–778.
- Chivavibul, P., M. Watanabe, S. Kuroda, J. Kawakita, M. Komatsu, K. Sato, and J. Kitamura. 2010. Effect of powder characteristics on properties of warm-sprayed WC-Co coatings. *Journal of Thermal Spray Technology* 19 (1–2): 81–88.
- Choi, S.R., D. Zhu, and R.A. Miller. 2005. Fracture behavior under mixed-mode loading of ceramic plasma-sprayed thermal barrier coatings at ambient and elevated temperatures. *Engineering Fracture Mechanics* 72: 2144–2158.
- Chraska, T. 1999. TEM studies of microstructures and interfaces of zirconia produced by plasma spraying. Ph.D. thesis, State University of New York at Stony Brook, New York.
- Chraska, T., and A.H. King. 2001. Transmission electron microscopy study of rapid solidification of plasma sprayed zirconia—Part I. First splat solidification. *Thin Solid Films* 397: 30–39.
- Christoulis, D.K., S. Guetta, E. Irissou, V. Guipont, M.H. Berger, M. Jeandin, J.-G. Legoux, C. Moreau, S. Costil, M. Boustie, Y. Ichikawa, and K. Ogawa. 2010. Cold-spraying coupled to nano-pulsed Nd-YaG laser surface pre-treatment. *Journal of Thermal Spray Technology* 19 (5): 1062–1073.
- Clark, H.M.I., H.M. Hawthorne, and Y. Xie. 1999. Wear rates and specific energies of some ceramic, cermet and metallic coatings determined in the Coriolis erosion tester. *Wear* 233–235: 319–327.
- Clyne, T.W., and S.C. Gill. 1996. Residual stresses in thermal spray coatings and their effect on interfacial adhesion: A review of recent work. *Journal of Thermal Spray Technology* 5 (4): 401–418.
- Cockeram, B.V., and W.L. Wilson. 2001. The hardness, adhesion and wear resistance of coatings developed for cobalt-base alloys. *Surface and Coating Technology* 139: 161–182.
- Costil, S., C. Verdy, R. Bolot, and C. Coddet. 2007. On the role of spraying process on microstructural, mechanical, and thermal response of alumina coatings. *Journal of Thermal Spray Technology* 16 (5–6): 839–843.

- Craig, B.D. 2005. Material failure modes, Part II: A brief tutorial on impact, spalling, wear, brinelling, thermal shock, and radiation damage. *Journal of Failure Analysis and Prevention* 5 (6): 7–12.
- CSM Instruments. 2010. *Advanced mechanical surface testing: Characterization of thermal spray coatings by instrumented indentation and scratch testing. Part II: Indentation of plasma sprayed coatings*, CSM instruments application bulletin, vol. 32. Peseux: CSM Instruments.
- Curran, J.A., and T.W. Clyne. 2006. Porosity in plasma electrolytic oxide coatings. *Acta Materialia* 54 (7): 1985–1993.
- Dallaire, S. 2001. Hard arc-sprayed coating with enhanced erosion and abrasion wear resistance. *Journal of Thermal Spray Technology* 10 (3): 511–519.
- Deevi, S.C., V.K. Sikka, C.J. Swindeman, and R.D. Seals. 1997. Reactive spraying of nickel-aluminide coatings. *Journal of Thermal Spray Technology* 6 (3): 335–344.
- Deshpande, S., A. Kulkarni, S. Sampath, and H. Herman. 2004. Application of image analysis for characterization of porosity in thermal spray coatings and correlation with small angle neutron scattering. *Surface and Coating Technology* 187: 6–16.
- Dey, A., A.K. Mukhopadhyay, S. Gangadharan, M.K. Sinha, and D. Basu. 2009. Weibull modulus of nano-hardness and elastic modulus of hydroxyapatite coating. *Journal of Materials Science* 44: 4911–4918.
- Drexler, J.M., A. Aygun, D. Li, R. Vaßen, T. Steinke, and N.P. Padture. 2010. Thermal-gradient testing of thermal barrier coatings under simultaneous attack by molten glassy deposits and its mitigation. *Surface and Coating Technology* 204: 2683–2688.
- Du, H., W. Hua, J. Liu, J. Gong, C. Sun, and L. Wen. 2005. Influence of process variables on the qualities of detonation gun sprayed WC–Co coatings. *Materials Science and Engineering A* 408: 202–210.
- Eaton, P., and P. West. 2010. *Atomic force microscopy*. Oxford: Oxford University Press.
- Elsebaei, A., J. Heberlein, M. Elshaer, and A. Farouk. 2010. Comparison of in-flight particle properties, splat formation, and coating microstructure for regular and nano-YSZ powders. *Journal of Thermal Spray Technology* 19 (1–2): 2–10.
- Emiliani, M.L. 1993. Debond coating requirements for brittle matrix composites. *Journal of Materials Science* 28: 5280–5296.
- Era, H., F. Otsubo, T. Uchida, S. Fukuda, and K. Kishitake. 1998. A modified shear test for adhesion evaluation of thermal sprayed coating. *Materials Science and Engineering A* 251: 166–172.
- Erickson, L.C., R. Westergard, U. Wiklund, N. Axén, H.M. Hawthorne, and L.S. Hogmark. 1998. Cohesion in plasma-sprayed coatings – A comparison between evaluation methods. *Wear* 214: 30–37.
- Etchart-Salas, R., V. Rat, J.F. Coudert, P. Fauchais, N. Caron, K. Wittman, and S. Alexandre. 2007. Influence of plasma instabilities in ceramic suspension plasma spraying. *Journal of Thermal Spray Technology* 16 (5–6): 857–865.
- Factor, M., and I. Roman. 2000a. Vickers micro-indentation of WC-12%Co thermal spray coating. Part 1: Statistical analysis of microhardness data. *Surface and Coating Technology* 132: 181–193.
- . 2000b. Vickers micro-indentation of WC-12%Co thermal spray coating. Part 2: The between-operator reproducibility limits of microhardness measurement and alternative approaches to quantifying hardness of cemented-carbide thermal spray coatings. *Surface and Coating Technology* 132: 65–75.
- Faisal, N.H., J.A. Steel, R. Ahmed, and R.L. Reuben. 2009. The use of acoustic emission to characterize fracture behavior during Vickers indentation of HVOF thermally sprayed WC-Co coatings. *Journal of Thermal Spray Technology* 18 (4): 525–535.
- Fan, X., and T. Ishigaki. 2001. Mo₅Si₃-B and MoSi₂ deposits fabricated by radio frequency induction plasma spraying. *Journal of Thermal Spray Technology* 10 (4): 611–617.
- Fauchais, P., G. Montavon, R.S. Lima, and B.R. Marple. 2011. Engineering a new class of thermal spray nano-based microstructures from agglomerated nanostructured particles. Suspensions and solutions: An invited review. *Journal of Physics D* 44: 093001.
- Feng, C., and B.S. Kang. 2006. A transparent indenter measurement method for mechanical property evaluation. *Experimental Mechanics* 46 (1): 91–103.
- . 2008. Young's modulus measurement using a simplified transparent indenter measurement technique. *Experimental Mechanics* 48: 9–15.
- Fernandez, J.E., R. Rodriguez, Y. Wang, R. Vijande, and A. Rincon. 1995. Sliding wear of a plasma-sprayed A₂O₃ coating. *Wear* 181–183: 417–425.
- Flores Renteria, A., B. Saruhan, J. Ilavsky, and A.J. Allen. 2007. Application of USAXS analysis and non-interacting approximation to determine the influence of process parameters and ageing on the thermal conductivity of electron-beam physical vapor-deposited thermal barrier coatings. *Surface and Coating Technology* 201: 4781–4788.
- Flores, A., Saruhan B. Renteria, J. Ilavsky, and A.J. Allenc. 2007. Application of USAXS analysis and non-interacting approximation to determine the influence of process parameters and ageing on the thermal conductivity of electron-beam physical vapor deposited thermal barrier coatings. *Surface and Coating Technology* 201: 4781–4788.
- Fowler, D.B., W. Riggs, and J.C. Russ. 1990. Inspecting thermal sprayed coatings. *Advanced Materials and Processes* 11: 41–52.
- Fox, A.C., and T.W. Clyne. 2004. Oxygen transport by gas permeation through the zirconia layer in plasma sprayed thermal barrier coatings. *Surface and Coating Technology* 184: 311–321.
- Fridrici, V., S. Fouvry, and P. Kapsa. 2003. Fretting wear behavior of a Cu–Ni–In plasma coating. *Surface and Coating Technology* 163–164: 429–434.
- Garcia, J.R., J.M. Cuetos, E. Fernandez, and V. Higuera. 2007. Laser surface melting Cr–Ni coatings, in the erosive-corrosive atmosphere of boilers. *Tribology Letters* 28: 99–108.
- Garcia, E., J. Mesquita-Guimaraes, P. Miranzo, M.I. Osendi, C.V. Cojocar, Y. Wang, C. Moreau, and R.S. Lima. 2011. Phase composition and microstructural responses of graded mullite/YSZ coatings under water vapor environments. *Journal of Thermal Spray Technology* 20 (1–2): 83–91.
- Gawne, D.T., Z. Qiu, Y. Bao, T. Zhang, and K. Zhang. 2001. Abrasive wear resistance of plasma-sprayed glass-composite coatings. *Journal of Thermal Spray Technology* 10 (4): 599–603.
- Gean, M.C., and T.N. Farris. 2009. Elevated temperature fretting fatigue of Ti-17 with surface treatments. *Tribology International* 42: 1340–1345.
- Geels, K. 2007. *Metallographic and materialographic specimen preparation, light microscopy, image analysis and hardness testing*, ASTM MNL46. West Conshohocken: ASTM International.
- Giannuzzi, L.A., and F.A. Stevens. 2004. *Introduction to focused ion beams: Instrumentation, theory, techniques and practice*. Berlin: Springer.
- Gill, S.C., and T.W. Clyne. 1994. Investigation of residual stress generation during thermal spraying by continuous curvature measurement. *Thin Solid Films* 250: 172–180.
- Giolli, C., A. Scrivani, G. Rizzi, F. Borgioli, G. Bolelli, and L. Lusvardi. 2009. Failure mechanism for thermal fatigue of thermal barrier coating systems. *Journal of Thermal Spray Technology* 18 (2): 223–230.
- Giraud, D., F. Borit, V. Guipont, and M. Jeandin. 2012. Metallization of a polymer using cold spray: Application to aluminum coating of polyamide 66. In *Thermal spray 2012: Proceedings (ITSC-2012)*, ed. R.S. Lima et al. Materials Park: ASM International. (e-proc).
- Gitzhofer, F., D. Lombard, A. Vardelle, M. Vardelle, C. Martin, and P. Fauchais. 1986. Thermophysical properties of zirconia coatings stabilized with calcia or yttria: Influence of spraying parameters and

- heat treatment. In *Advances in thermal spraying*, 269–275. Oxford: Pergamon.
- Gobinda, C.S., and T.I. Khan. 2010. The corrosion and wear performance of microcrystalline WC-10Co-4Cr and near-nanocrystalline WC-17Co high velocity oxy-fuel sprayed coatings on steel substrate. *Metallurgical and Materials Transactions A: Physical Metallurgy and Materials Science* 41A: 3000–3009.
- Golosnoy, I.O., S. Paul, and T.W. Clyne. 2008. Modelling of gas permeation through ceramic coatings produced by thermal spraying. *Acta Materialia* 56: 874–883.
- Greving, D.J., J.R. Shadley, and E.F. Rybicki. 1994a. Effects of coating thickness and residual stresses on the bond strength of ASTM C633-79 thermal spray coating test specimens. *Journal of Thermal Spray Technology* 3 (4): 371–378.
- Greving, D.J., E.F. Rybicki, and J.R. Shadley. 1994b. Through-thickness residual stress evaluations for several industrial thermal spray coatings using a modified layer-removal method. *Journal of Thermal Spray Technology* 3 (4): 379–388.
- Guetta, S., M.H. Berger, F. Borit, V. Guipont, M. Jeandin, M. Boustie, Y. Ichikawa, K. Sakaguchi, and K. Ogawa. 2009. Influence of particle velocity on adhesion of cold-sprayed splats. *Journal of Thermal Spray Technology* 18 (3): 331–342.
- Guilemany, J.M., J.M. Miguel, S. Armada, S. Vizcaino, and F. Climent. 2001. Use of scanning white light interferometry in the characterization of wear mechanisms in thermal-sprayed coatings. *Materials Characterization* 47: 307–314.
- Guilemany, J.M., N. Espallargas, P.H. Suegama, A.V. Benedetti, and J. Fernández. 2005. High-velocity oxyfuel Cr₃C₂-NiCr replacing hard chromium coatings. *Journal of Thermal Spray Technology* 14 (3): 336–341.
- Guilemany, J.M., M. Torrell, and J.R. Miguel. 2008. Study of the HVOF Ni-based coatings corrosion resistance applied on municipal solid-waste incinerators. *Journal of Thermal Spray Technology* 17 (2): 254–262.
- Guilemany, J.M., N. Cinca, S. Dosta, and I.G. Cano. 2009. FeAl and NbAl₃ intermetallic-HVOF coatings: Structure and properties. *Journal of Thermal Spray Technology* 18 (4): 536–545.
- Guinier, A., and G. Fournet. 1955. *Small angle scattering of X-rays*. New York: Wiley.
- Guipont, V. 2013. Microstructures and interfaces ceramic/metal obtained by physical processes. State thesis, University of Limoges, Limoges.
- Han, W., E.E. Rybicki, and J.R. Shadley. 1993a. An improved specimen geometry for ASTM C633-79 to estimate bond strengths of thermal spray coatings. *Journal of Thermal Spray Technology* 2 (2): 145–150.
- Han, W., E.F. Rybicki, and J.R. Shadley. 1993b. Application of fracture mechanics to the interpretation of bond strength data from ASTM Standard C633-79. *Journal of Thermal Spray Technology* 2 (3): 235–241.
- Hanson, T.C., and G.S. Settles. 2003. Particle temperature and velocity effects on the porosity and oxidation of an HVOF corrosion-control coating. *Journal of Thermal Spray Technology* 12 (3): 403–415.
- Harok, V., and K. Neufuss. 2001. Elastic and inelastic effects in compression in plasma-sprayed ceramic coatings. *Journal of Thermal Spray Technology* 10 (1): 126–132.
- Hasselman, D.P.H. 1970. Thermal stress resistance parameters for brittle refractory ceramics: A compendium. *American Ceramic Society Bulletin* 49 (12): 1033–1037.
- He, G.H., J.D. Guo, Y.Y. Zhang, B.Q. Wang, and B.L. Zhou. 2000. Measurement of thermal diffusivity of thermal control coatings by the flash method using two-layer composite sample. *International Journal of Thermophysics* 21 (2): 535–542.
- He, D., N. Dong, and J. Jiang. 2007. Corrosion behavior of arc sprayed nickel-base coatings. *Journal of Thermal Spray Technology* 16 (5–6): 850–856.
- He, D.-Y., B.-Y. Fu, J.-M. Jiang, and X.-Y. Li. 2008. Microstructure and wear performance of arc sprayed Fe-FeB-WC coatings. *Journal of Thermal Spray Technology* 17 (5–6): 757–761.
- Heintze, G.N., and R. McPherson. 1988. Fracture toughness of plasma sprayed zirconia coatings. *Surface and Coating Technology* 134: 15–23.
- Hejwowski, T. 2009. Erosive and abrasive wear resistance of overlay coatings. *Vacuum* 83: 166–170.
- Hejwowski, T., S. Szewczyk, and A. Weronki. 2000. An investigation of the abrasive and erosive wear of flame-sprayed coatings. *Journal of Materials Processing Technology* 106: 54–57.
- Heping, L., P. Nie, Y. Yan, J. Wang, and B. Sun. 2010. Characterization and adhesion strength study of detonation-sprayed MoB-CoCr alloy coatings on 2Cr13 stainless steel substrate. *Journal of Coating Technology and Research* 7 (6): 801–807.
- Higuera Hidalgo, V., J. Belzunce Varela, A. Carriles Menéndez, and S. Poveda Martínez. 2001. High temperature erosion wear of flame and plasma-sprayed nickel-chromium coatings under simulated coal-fired boiler atmospheres. *Wear* 247: 214–222.
- Hivart, P., and J. Crampon. 2007. Interfacial indentation test and adhesive fracture characteristics of plasma sprayed cermet Cr₃C₂/Ni-Cr coatings. *Mechanics of Materials* 39: 998–1005.
- Hugot, F., J. Patru, P. Fauchais, and L. Bianchi. 2007. Modelling of a substrate thermomechanical behavior during plasma spraying. *Journal of Materials Processing Technology* 190 (1–3): 317–323.
- Hung, Y.Y., Y.S. Chen, S.P. Ng, L. Liu, Y.H. Huang, B.L. Luk, R.W.L. Ip, C.M.L. Wu, and P.S. Chung. 2009. Review and comparison of shearography and active thermography for non-destructive evaluation. *Materials Science and Engineering R* 64: 73–112.
- Ibrahim, A., and C.C. Berndt. 2007. Fatigue and deformation of HVOF sprayed WC-Co coatings and hard chrome plating. *Materials Science and Engineering A* 456: 114–119.
- Ibrahim, A., R.S. Lima, C.C. Berndt, and B.R. Marple. 2007. Fatigue and mechanical properties of nanostructured and conventional titania (TiO₂) thermal spray coatings. *Surface and Coating Technology* 201: 7589–7596.
- Ilavsky, J. 2010. Characterization of complex thermal barrier deposits pore microstructures by a combination of imaging, scattering and intrusion techniques. *Journal of Thermal Spray Technology* 19 (1–2): 178–189.
- Ilavsky, J., and C.C. Berndt. 1998. Thermal expansion properties of metallic and cermet coatings. *Surface and Coating Technology* 102: 19–24.
- Ilavsky, J., H. Herman, C.C. Berndt, A.N. Goland, G.G. Long, S. Krueger, and A.J. Allen. 1994. In *Thermal spray industrial applications*, ed. C.C. Berndt and S. Sampath, 709–715. Materials Park: ASM International.
- Ilavsky, J., C.C. Berndt, and J. Karthikeyan. 1997. Mercury intrusion porosimetry of plasma-sprayed ceramic. *Journal of Materials Science* 32: 3925–3932.
- Ilavsky, J., G.G. Long, A.J. Allen, L. Leblanc, M. Prystay, and C. Moreau. 1999a. Anisotropic microstructure of plasma-sprayed deposits. *Journal of Thermal Spray Technology* 8 (3): 414–420.
- Ilavsky, J., G.G. Long, A.J. Allen, and C.C. Berndt. 1999b. Evolution of the void structure in plasma-sprayed YSZ deposits during heating. *Materials Science and Engineering A* 272: 215–221.
- Ilavsky, J., P.R. Jemian, A.J. Allen, F. Zhang, L.E. Levine, and G.G. Long. 2009a. Ultra-small-angle X-ray scattering at the advanced photon source. *Journal of Applied Crystallography* 42: 1–11.

- . 2009b. Ultra-small-angle X-ray scattering at the advanced photon source. *Journal of Applied Crystallography* 42 (3): 469–479.
- Ingo, G.M., S. Kaciulis, A. Mezzi, T. Valente, F. Casadei, and G. Gusmano. 2005. Characterization of composite titanium nitride coatings prepared by reactive plasma spraying. *Electrochimica Acta* 50: 4531–4537.
- Irisawa, T., and H. Matsumoto. 2006. Thermal shock resistance and adhesion strength of plasma-sprayed alumina coating on cast iron. *Thin Solid Films* 509: 141–144.
- Ishikawa, Y., J. Kawakita, S. Osawa, T. Itsukaichi, Y. Sakamoto, M. Takaya, and S. Kuroda. 2005. Evaluation of corrosion and wear resistance of hard cermet coatings sprayed by using an improved HVOF process. *Journal of Thermal Spray Technology* 14 (3): 384–390.
- Jadhav, A.D., N.P. Padture, E.H. Jordan, M. Gell, P. Miranzo, and E.R. Fuller Jr. 2006. Low-thermal-conductivity plasma-sprayed thermal barrier coatings with engineered microstructures. *Acta Materialia* 54: 3343–3349.
- James, J.D., J.A. Spittle, S.G.R. Brown, and R.W. Evans. 2001. A review of measurement techniques for the thermal expansion coefficient of metals and alloys at elevated temperatures. *Measurement Science and Technology* 12: R1–R15.
- Jayaraj, B., V.H. Desai, C.K. Lee, and Y.H. Sohn. 2004. Electrochemical impedance spectroscopy of porous ZrO_2 -8 wt.% Y_2O_3 and thermally grown oxide on nickel aluminide. *Materials Science and Engineering A* 372 (1–2): 278–286.
- Jeandin, M., D.K. Christoulis, F. Borit, M.H. Berger, S. Guetta, G. Rolland, V. Guipont, E. Irissou, J.G. Legoux, C. Moreau, M. Nivard, L. Berthe, M. Boustie, K. Sakaguchi, Y. Ichikawa, K. Ogawa, and S. Costil. 2010. Lasers and thermal spray. *Materials Science Forum* 174: 638–642.
- Jennifer, S.Y., H. Wang, W.D. Porter, A.R. de Arellano Lopez, and K.T. Faber. 2001. Thermal conductivity and phase evolution of plasma-sprayed multilayer coatings. *Journal of Materials Science* 36: 3511–3518.
- Ji, G.-C., C.-J. Li, Y.-Y. Wang, and W.-Y. Li. 2007. Erosion performance of HVOF-sprayed Cr_3C_2 -NiCr coatings. *Journal of Thermal Spray Technology* 16 (4): 557–565.
- Kang, H.-K., and S. Bong Kange. 2004. Behavior of porosity and copper oxidation in W/Cu composite produced by plasma spray. *Journal of Thermal Spray Technology* 13 (2): 223–228.
- Kawakita, J., S. Kuroda, and T. Kodama. 2003. Evaluation of through-porosity of HVOF sprayed coating. *Surface and Coating Technology* 166: 17–23.
- Kennedy, D.M., and M.S.J. Hashmi. 1998. Methods of wear testing for advanced surface coatings and bulk materials. *Journal of Materials Processing Technology* 77: 246–253.
- Kim, H.J., Y.G. Kweon, and R.W. Chang. 1994. Wear and erosion behavior of plasma-sprayed WC-Co coatings. *Journal of Thermal Spray Technology* 3 (2): 169–178.
- Kishitake, K., H. Era, and F. Otsubo. 1996. Characterization of plasma sprayed Fe-17Cr-38Mo-4C amorphous coatings crystallizing at extremely high temperature. *Journal of Thermal Spray Technology* 5 (3): 283–288.
- Koiprasert, H., S. Dumrongrattana, and P. Niranatlumpong. 2004. Thermally sprayed coatings for protection of fretting wear in land-based gas-turbine engine. *Wear* 257: 1–7.
- Koivuluoto, H., J. Lagerbom, M. Kylmälahti, and P. Vuoristo. 2008. Microstructure and mechanical properties of low-pressure cold-sprayed (LPCS) coatings. *Journal of Thermal Spray Technology* 17 (5–6): 721–727.
- Kovarik, O., J. Siegl, J. Nohava, and P. Chraska. 2005. Young's modulus and fatigue behavior of plasma-sprayed alumina coatings. *Journal of Thermal Spray Technology* 14 (2): 231–238.
- Kovarik, O., J. Siegl, and Z. Prochazka. 2008. Fatigue behavior of bodies with thermally sprayed metallic and ceramic deposits. *Journal of Thermal Spray Technology* 17 (4): 525–532.
- Krishnamurthy, N., S.C. Sharma, M.S. Murali, and P.G. Mukunda. 2009. Adhesion behavior of plasma sprayed thermal barrier coatings on Al-6061 and cast-iron substrates. *Frontiers of Materials Science in China* 3 (3): 333–338.
- Kucuk, A., C.C. Berndt, U. Senturk, and R.S. Lima. 2000a. Influence of plasma spray parameters on mechanical properties of yttria stabilized zirconia coatings. I: Four-point bend test. *Materials Science and Engineering A* 284: 29–40.
- . 2000b. Influence of plasma spray parameters on mechanical properties of yttria stabilized zirconia coatings. II: Acoustic emission response. *Materials Science and Engineering A* 284: 41–50.
- Kulkarni, A., Z. Wang, T. Nakamura, S. Sampath, A. Goland, H. Herman, J. Allen, J. Ilavsky, G.G. Long, J. Frahm, and R.W. Steinbrech. 2003. Comprehensive microstructural characterization and predictive property modeling of plasma-sprayed zirconia coatings. *Acta Materialia* 51: 2457–2475.
- Kulkarni, A.A., A. Goland, H. Herman, A.J. Allen, J. Ilavsky, G.G. Long, and F. De Carlo. 2005. Advanced microstructural characterization of plasma-sprayed zirconia coatings over extended length scales. *Journal of Thermal Spray Technology* 14 (2): 239–250.
- Kulkarni, A., A. Goland, H. Herman, A.J. Allen, T. Dobbins, F. DeCarlo, J. Ilavsky, G.G. Long, S. Fang, and P. Lawton. 2006. Advanced neutron and X-ray techniques for insights into the microstructure of EB-PVD thermal barrier coatings. *Materials Science and Engineering A* 426: 43–52.
- Kulu, P., and T. Pihl. 2002. Selection criteria for wear resistant powder coatings under extreme erosive wear conditions. *Journal of Thermal Spray Technology* 11 (4): 517–522.
- Kuroda, S., T. Kukushima, and S. Kitahara. 1988. Simultaneous measurement of coating thickness and deposition stress during thermal spraying. *Thin Solid Films* 164: 157–163.
- Kuroda, S., Y. Tashiro, H. Yumoto, S. Taira, H. Fukanuma, and S. Tobe. 2001. Peening action and residual stresses in high-velocity oxygen fuel thermal spraying of 316L stainless steel. *Journal of Thermal Spray Technology* 10 (2): 367–374.
- Landa, M., F. Kroupa, K. Neufuss, and P. Urbanek. 2003. Effect of uniaxial pressure on ultrasound velocities and elastic moduli in plasma-sprayed ceramics. *Journal of Thermal Spray Technology* 12 (2): 226–233.
- Langford, J.I., and A.J.C. Wilson. 1978. Scherrer after sixty years: A survey and some new results in the determination of crystallite size. *Journal of Applied Crystallography* 1: 102–113.
- Lee, H., S. Mall, J.H. Sanders, and S.K. Sharma. 2005. Wear analysis of Cu–Al coating on Ti–6Al–4V substrate under fretting condition. *Tribology Letters* 19 (3): 239–248.
- Lee, H., S. Mall, and K.N. Murray. 2007. Fretting wear behavior of Cu–Al coating on Ti–6Al–4V substrate under dry and wet (lubricated) contact condition. *Tribology Letters* 28: 19–25.
- Leigh, S.H., and C.C. Berndt. 1994. A test for coating adhesion on flat substrates – A technical note. *Journal of Thermal Spray Technology* 3 (2): 184–190.
- Leigh, S.-H., and C.C. Berndt. 1999. Modelling of elastic constants of plasma spray deposits with ellipsoid-shaped voids. *Acta Materialia* 47 (5): 1575–1586.
- Lesage, J., M.H. Staiab, D. Chicot, C. Godoy, and P.E.V. De Mirandad. 2000. Effect of thermal treatments on adhesive properties of a NiCr thermal sprayed coating. *Thin Solid Films* 377–378: 681–686.
- Li, J., and C. Ding. 2001. Determining microhardness and elastic modulus of plasma-sprayed Cr_2C_3 -NiCr coatings using Knoop indentation testing. *Surface and Coating Technology* 135: 229–237.

- Li, C.-J., and Y.-Y. Wang. 2002. Effect of particle state on the adhesive strength of HVOF sprayed metallic coating. *Journal of Thermal Spray Technology* 11 (4): 523–529.
- Li, H., K.A. Khor, and P. Cheanga. 2002. Young's modulus and fracture toughness determination of high velocity oxy-fuel-sprayed bioceramic coatings. *Surface and Coating Technology* 155: 21–32.
- Li, C.-J., X.-J. Ning, and C.-X. Li. 2005. Effect of densification processes on the properties of plasma-sprayed YSZ electrolyte coatings for solid oxide fuel cells. *Surface and Coating Technology* 190: 60–64.
- Li, L., N. Hitchman, and J. Knapp. 2010. Failure of thermal barrier coatings subjected to CMAS attack. *Journal of Thermal Spray Technology* 19 (1–2): 148–155.
- Li, C.-J., H.-T. Wang, G.-J. Yang, and C.-G. Bao. 2011. Characterization of high-temperature abrasive wear of cold-sprayed FeAl intermetallic compound coating. *Journal of Thermal Spray Technology* 20: 227–233.
- Lima, C.R.C., and J.M. Guilemany. 2007. Adhesion improvements of thermal barrier coatings with HVOF thermally sprayed bond coats. *Surface and Coating Technology* 201: 4694–4701.
- Lima, R.S., and B.R. Marple. 2003. High Weibull modulus HVOF titania coatings. *Journal of Thermal Spray Technology* 12 (2): 240–249.
- Lima, R.S., A. Kucuk, and C.C. Berndt. 2001a. Integrity of nanostructured partially stabilized zirconia after plasma spray processing. *Materials Science and Engineering A313*: 75–82.
- . 2001b. Evaluation of microhardness and elastic modulus of thermally sprayed nanostructured zirconia coatings. *Surface and Coating Technology* 135: 166–172.
- . 2002. Bimodal distribution of mechanical properties on plasma sprayed nanostructured partially stabilized zirconia. *Materials Science and Engineering A327*: 224–232.
- Lima, R.S., S.E. Kruger, G. Lamouche, and B.R. Marple. 2003a. Elastic modulus measurements via laser-ultrasonic and Knoop indentation techniques. In *ITSC-2003: Advancing the science and applying the technique*, ed. C. Moreau and B. Marple, 1369–1378. Materials Park: ASM International.
- Lima, M.M., C. Godoy, J.C. Avelar-Batista, and P.J. Modenesi. 2003b. Toughness evaluation of HVOF WC-Co coatings using non-linear regression analysis. *Materials Science and Engineering A357*: 337–345.
- Lima, M.M., C. Godoy, P.J. Modenesi, J.C. Avelar-Batista, A. Davison, and A. Matthews. 2004. Coating fracture toughness determined by Vickers indentation: An important parameter in cavitation erosion resistance of WC-Co thermally sprayed coatings. *Surface and Coating Technology* 177–178: 489–496.
- Lima, C.R.C., J. Nin, and J.M. Guilemany. 2006. Evaluation of residual stresses of thermal barrier coatings with HVOF thermally sprayed bond coats using the modified layer removal method (MLRM). *Surface and Coating Technology* 200: 5963–5972.
- Lin, C.K., and C.C. Berndt. 1993. Microhardness variations in thermally sprayed coatings. In *Proceedings of the national thermal spray conference*, ed. C.C. Berndt and T.F. Bernicki, 561–564. Materials Park: ASM International.
- . 1994. Measurement and analysis of adhesion strength for thermally sprayed coatings. *Journal of Thermal Spray Technology* 3 (1): 75–104.
- . 1998. Acoustic emission studies on thermal spray materials. *Surface and Coating Technology* 102: 1–7.
- Lin, J.F., M.H. Liu, and J.D. Wu. 1996. Analysis of the friction and wear mechanisms of structural ceramic coatings. Part 1: The effect of processing conditions. *Wear* 194: 1–11.
- Lin, C.K., C.C. Berndt, S.H. Leigh, and K. Murakami. 1997. Acoustic emission studies of alumina-13% titania free-standing forms during four-point bend tests. *Journal of the American Ceramic Society* 80: 2382–2394.
- Liu, X., and C. Ding. 2002. Thermal properties and microstructure of a plasma sprayed wollastonite coating. *Journal of Thermal Spray Technology* 11 (3): 375–379.
- Liu, R., and D.Y. Li. 1999. Protective effect of yttrium additive in lubricants on corrosive wear. *Wear* 225–229: 968–974.
- Liu, Y., and H.M. Wang. 2010. Microstructure and wear property of laser-clad $\text{Co}_3\text{Mo}_2\text{Si}/\text{Co}_{ss}$ wear resistant coatings. *Surface and Coating Technology* 205: 377–382.
- Liu, X.Q., Y.G. Zheng, X.C. Chang, W.L. Hou, J.Q. Wang, Z. Tang, and A. Burgess. 2009. Microstructure and properties of Fe-based amorphous metallic coating produced by high velocity axial plasma spraying. *Journal of Alloys and Compounds* 484: 300–307.
- Luiz de Assis, S., S. Wolyneec, and I. Costa. 2006. Corrosion characterization of titanium alloys by electrochemical techniques. *Electrochimica Acta* 51: 1815–1819.
- Lypouth, C., P. Nylén, A. Manescu, and T. Pirling. 2008. Residual stresses distribution through thick HVOF sprayed Inconel 718 coatings. *Journal of Thermal Spray Technology* 17 (5–6): 915–923.
- Ma, X.Q., and M. Takemoto. 2001. Quantitative acoustic emission analysis of plasma, sprayed thermal barrier coatings subjected to thermal shock tests. *Materials Science and Engineering A308*: 101–110.
- Ma, X.Q., Y. Mizutani, and M. Takemoto. 2001a. Laser-induced surface acoustic waves for evaluation of elastic stiffness of plasma sprayed materials. *Journal of Materials Science* 36: 5633–5641.
- Ma, X.Q., S. Cho, and M. Takemoto. 2001b. Acoustic emission source analysis of plasma sprayed thermal barrier coatings during four-point bend tests. *Surface and Coating Technology* 139: 55–62.
- Ma, X.Q., D.W. Gandy, and G.J. Frederick. 2008. Innovation of ultra-fine structured alloy coatings having superior mechanical properties and high temperature corrosion resistance. *Journal of Thermal Spray Technology* 17 (5–6): 933–941.
- Ma, D., C.W. Ong, and T. Zhang. 2009. An instrumented indentation method for Young's modulus measurement with accuracy estimation. *Experimental Mechanics* 49: 719–729.
- Magnani, M., P.H. Suegama, N. Espallargas, C.S. Fugivara, S. Dosta, J.M. Guilemany, and A.V. Benedettir. 2009. Corrosion and wear studies of Cr_3C_2 -NiCr-HVOF coatings sprayed on AA7050 T7 under cooling. *Journal of Thermal Spray Technology* 18 (3): 354–363.
- Majzoobi, G.H., R. Hojjati, M. Nematian, E. Zalnejad, A.R. Ahmadkhani, and E. Hanifepoor. 2010. A new device for fretting fatigue testing. *Transactions of the Indian Institute of Metals* 63 (2–3): 493–497.
- Maldague, X., and S. Marinetti. 1996. Pulse phase infrared thermography. *Journal of Applied Physics* 79 (5): 2694–2698.
- Mancini, C.E., C.C. Berndt, L. Sun, and A. Kucuk. 2001. Porosity determinations in thermally sprayed hydroxyapatite coatings. *Journal of Materials Science* 36: 3891–3896.
- Mann, B.S., and V. Arya. 2001. Abrasive and erosive wear characteristics of plasma nitriding and HVOF coatings: Their application in hydro turbines. *Wear* 249: 354–360.
- Marcano, Z., J. Lesage, D. Chicot, G. Mesmacque, E.S. Puchi-Cabrera, and M.H. Staiaa. 2008. Microstructure and adhesion of Cr_3C_2 -NiCr vacuum plasma sprayed coatings. *Surface and Coating Technology* 202: 4406–4410.
- Marinetti, S., D. Robba, F. Cernuschi, P.G. Bison, and E. Grinzato. 2007. Thermographic inspection of TBC coated gas turbine blades: Discrimination between coating over-thicknesses and adhesion defects. *Infrared Physics & Technology* 49: 281–285.
- Marot, G., P. Démarécaux, J. Lesage, M. Hadad, and Staia M.H. St. Siegmann. 2008. The interfacial indentation test to determine adhesion and residual stresses in NiCr VPS coatings. *Surface and Coating Technology* 202: 4411–4416.

- Marshall, D.B., T. Noma, and A.G. Evans. 1982. A simple method for determining elastic-modulus-to-hardness ratios using Knoop indentation measurements. *Communications of the American Ceramic Society* 65: C175–C176.
- Matějček, J., B. Kolman, J. Dubský, K. Neufuss, N. Hopkins, and J. Zwick. 2006. Alternative methods for determination of composition and porosity in abradable materials. *Materials Characterization* 57: 17–29.
- Matthews, S., B. James, and M. Hyland. 2010. The effect of heat treatment on the oxidation mechanism of blended powder Cr₃C₂-NiCr coatings. *Journal of Thermal Spray Technology* 19 (1–2): 119–127.
- Mauer, G., R. Vaßen, and D. Stöver. 2009. Atmospheric plasma spraying of yttria-stabilized zirconia coatings with specific porosity. *Surface and Coating Technology* 204: 172–179.
- McGrann, R.T.R., D.J. Greving, J.R. Shadley, E.F. Rybicki, B.E. Bodger, and D.A. Somerville. 1998. The effect of residual stress in HVOF tungsten carbide coatings on the fatigue life in bending of thermal spray coated aluminum. *Journal of Thermal Spray Technology* 7 (4): 546–552.
- Meacham, B.E., M.C. Marshall, and D.J. Branagan. 2006. Palmqvist fracture toughness of a new wear-resistant weld alloy. *Metallurgical and Materials Transactions A* 37A: 3617–3627.
- Michlik, P., and C.C. Berndt. 2006. Image-based extended finite element modeling of thermal barrier coatings. *Surface and Coating Technology* 201: 2369–2380.
- Montavon, G. 2004. *Quality control of thermal sprayed coatings, course thermal spraying*. Limoges: Aliderte.
- Montavon, G., and G. Antou. 2007. Quantifying thermal spray coating architecture by stereological protocols: Part I. A historical perspective. *Journal of Thermal Spray Technology* 16 (1): 6–14.
- Montavon, G., C. Coddet, C.C. Berndt, and S.-H. Leigh. 1998. Microstructural index to quantify thermal spray deposit microstructures using image analysis. *Journal of Thermal Spray Technology* 7 (2): 229–241.
- Musalek, R., J. Matejček, M. Vilemova, and O. Kovarik. 2010. Non-linear mechanical behavior of plasma sprayed alumina under mechanical and thermal spray loading. *Journal of Thermal Spray Technology* 19 (1–2): 422–428.
- Musil, J., F. Kunc, H. Zeman, and H. Polakova. 2002. Relationships between hardness, Young's modulus and elastic recovery in hard nanocomposite coatings. *Surface and Coating Technology* 154: 304–313.
- Nolan, D.J., and M. Samandi. 1997. Revealing true porosity in WC-Co thermal spray coatings. *Journal of Thermal Spray Technology* 6 (4): 422–424.
- Noone, M.J., and R.L. Mehan. 1974. In *Fracture mechanics of ceramics*, ed. R.C. Bradt, Hasselman DPH, and F.F. Lange, 201–229. Plenum: New York.
- Nusair Khan, A., and J. Lu. 2003. Behavior of air plasma sprayed thermal barrier coatings, subject to intense thermal cycling. *Surface and Coating Technology* 166: 37–43.
- Ozdemir, I., I. Hamanaka, Y. Tsunekawa, and M. Okumiya. 2005. In-process exothermic reaction in high-velocity oxyfuel and plasma spraying with SiO₂/Ni/Al-Si-Mg composite powder. *Journal of Thermal Spray Technology* 14 (3): 321–329.
- Paul, S., and K. Yadav. 2010. Corrosion behavior of surface-treated implant Ti-6Al-4V by electrochemical polarization and impedance studies. *Journal of Materials Engineering and Performance* 20 (3): 422–435.
- Pawlowski, L. 1995. *The science and engineering of thermal spray coatings*. New York: Wiley, 2nd (2008), Ed. (656 p).
- Pejryd, L., J. Wigren, D.J. Greving, J.R. Shadley, and E.E. Rybicki. 1995. Residual stresses as a factor in the selection of tungsten carbide coatings for a jet engine application. *Journal of Thermal Spray Technology* 4 (3): 268–274.
- Pershin, V., M. Lufitha, S. Chandra, and J. Mostaghimi. 2003. Effect of substrate temperature on adhesion strength of plasma-sprayed nickel coatings. *Journal of Thermal Spray Technology* 12 (3): 370–376.
- Petorak, C., J. Ilavsky, H. Wang, W. Porter, and R. Trice. 2010. Microstructural evolution of 7 wt.% Y₂O₃-ZrO₂ thermal barrier coatings due to stress relaxation at elevated temperatures and the concomitant changes in thermal conductivity. *Surface and Coating Technology* 205: 57–65.
- Podrezov, Y.N., Y.V. Mil'man, D.V. Lotsko, N.L. Lugovoi, D.G. Verbilo, and N.A. Efimov. 1999. A method of determining the mechanical properties of a two-layer composite consisting of a steel matrix and a plasma spray coating based on amorphizing powders. *Powder Metallurgy and Metal Ceramics* 38 (5–6): 224–227.
- Prasad, B.K. 2000. Effects of alumina particle dispersion on the erosive-corrosive wear response of a zinc-based alloy under changing slurry conditions and distance. *Wear* 238: 151–159.
- Prasad Sahu, S., A. Satapathy, A. Patnaik, K.P. Sree Kumar, and P.V. Ananthapadmanabhan. 2010. Development, characterization and erosion wear response of plasma sprayed fly ash-aluminum coatings. *Materials and Design* 31: 1165–1173.
- Prudenziati, M., G.C. Gazzadi, M. Medici, G. Dalbagni, and M. Caliori. 2010. Cr₃C₂-NiCr HVOF-sprayed coatings: Microstructure and properties versus powder characteristics and process parameters. *Journal of Thermal Spray Technology* 19 (3): 541–550.
- Puerta, D.G. 2005. Metallographic preparation and evaluation of thermal spray coatings: Mounting, TSS committee on accepted practices. *Journal of Thermal Spray Technology* 14 (4): 450–452.
- . 2006. Metallographic preparation and testing of thermal spray coatings: Grinding, TSS committee on accepted practices. *Journal of Thermal Spray Technology* 15 (1): 31–32.
- . 2008. TSS accepted practices committees—Metallography and mechanical testing. *Journal of Thermal Spray Technology* 17 (4): 435–436.
- Qi, Z.M., S. Amada, S. Akiyama, and C. Takahashi. 1988. Evaluation of thermal shock strength of thermal-sprayed coatings by the laser irradiation technique. *Surface and Coating Technology* 110: 73–80.
- Rainforth, W.M. 2004. The wear behaviour of oxide ceramics—A review. *Journal of Materials Science* 39: 6705–6721.
- Rammo, N.N., H.R. Al-Amery, T. Abdul-Jabbar, and H.I. Jaffer. 2009. Adhesion, hardness and structure of thermal sprayed Al/SiC composite, coat on graphite. *Surface and Coating Technology* 203: 2891–2895.
- Rätzer-Scheibe, H.-J., U. Schulz, and T. Krell. 2006. The effect of coating thickness on the thermal conductivity of EB-PVD PYSZ thermal barrier coatings. *Surface and Coating Technology* 200: 5636–5644.
- Ravi, B.G., A.S. Gandhi, X.Z. Guo, J. Margolies, and S. Sampath. 2008. Liquid precursor plasma spraying of functional materials: A case study for yttrium aluminum garnet (YAG). *Journal of Thermal Spray Technology* 17 (1): 82–90.
- Reed, J.S. 1995. *Principles of ceramics processing*. New York: Wiley.
- Rendler, N.J., and I. Vigness. 1966. Hole drilling method of measuring residual stresses. *Experimental Mechanics* 6 (12): 577–586.
- Rice, R.W. 1996. Porosity dependence of physical properties of materials: A summary review. *Key Engineering Materials* 115: 1–19.
- Richard, C.S., J. Lu, G. Béranger, and F. Decomps. 1995. Study of Cr₂O₃ coatings. Part II: Adhesion to a cast-iron substrate. *Journal of Thermal Spray Technology* 4 (4): 347–352.
- Richard, C.S., G. Béranger, J. Lu, J.F. Flavenot, and T. Grégoire. 1996. Four-point bending tests of thermally produced WC-Co coatings. *Surface and Coating Technology* 78 (284): 294.
- Rickerby, D.S. 1988. A review of the methods for the measurement of coating-substrate adhesion. *Surface and Coating Technology* 36 (1–2): 541–557.

- Riggs, W. 2004. Metallography and image analysis. In *Handbook of thermal spray technology*, ed. J.R. Davis, 224–259. Metals Park: ASM International.
- Robin, P., F. Gitzhofer, P. Fauchais, and M. Boulos. 2010. Remaining fatigue life assessment of plasma sprayed thermal barrier coatings. *Journal of Thermal Spray Technology* 19 (5): 911–920.
- Rolland, G., P. Sallamand, V. Guipont, M. Jeandin, E. Boller, and C. Bourda. 2011. Laser-induced damage in cold-sprayed composite coatings. *Surface and Coating Technology* 205: 4915–4927.
- Rosa, G., P. Psyllaki, R. Oltra, S. Costil, and C. Coddet. 2001. Simultaneous laser generation and laser ultrasonic detection of the mechanical breakdown of a coating-substrate interface. *Ultrasonics* 39: 355–365.
- Roy, M., A. Pauschitz, J. Bernardi, T. Koch, and F. Franek. 2006. Microstructure and mechanical properties of HVOF sprayed nanocrystalline Cr₃C₂-25(Ni20Cr) coating. *Journal of Thermal Spray Technology* 15 (3): 372–381.
- Russ, J.C. 1995. *The image processing handbook*, 2nd ed. Boca Raton: CRC.
- . 2011. *The image processing handbook*, 6th ed. Boca Raton: CRC, Taylor & Francis Group.
- Russ, J.C., and R.T. DeHoff. 1999. *Practical stereology*, 2nd ed. New York: Plenum.
- Salimijazi, H., M. Hosseini, J. Mostaghimi, L. Pershin, T.W. Coyle, H. Samadi, and A. Shafyei. 2012. Plasma sprayed coating using mullite and mixed alumina/silica powders. *Journal of Thermal Spray Technology* 21 (5): 825–830.
- Sampath, S., X.Y. Jiang, J. Matejcek, L. Prchlik, A. Kulkarni, and A. Vaidya. 2004. Role of thermal spray processing method on the microstructure, residual stress and properties of coatings: An integrated study for Ni-5 wt.%Al bond coats. *Materials Science and Engineering A* 364: 216–231.
- Sansoucy, E., G.E. Kim, A.L. Moran, and B. Jodoin. 2007. Mechanical characteristics of Al-Co-Ce coatings produced by the cold spray process. *Journal of Thermal Spray Technology* 16 (5–6): 651–660.
- Santana, Y.Y., P.O. Renault, M. Sebastiani, J.G. La Barbera, J. Lesage, E. Bemporad, E. Le Bourhis, E.S. Puchi-Cabrera, and M.H. Staia. 2008. Characterization and residual stresses of WC–Co thermally sprayed coatings. *Surface and Coating Technology* 202: 4560–4565.
- Saravanan, P., V. Selvarajan, M.P. Srivastava, D.S. Rao, S.V. Joshi, and G. Sundararajan. 2000. Study of plasma- and detonation gun-sprayed alumina coatings using Taguchi experimental design. *Journal of Thermal Spray Technology* 9 (4): 505–512.
- Sauer, J.P. 2005. Metallographic preparation and testing of thermal spray coatings: Sectioning. TSS committee on accepted practices. *Journal of Thermal Spray Technology* 14 (3): 313–314.
- Sauer, J.P., and G. Blann. 2006. Metallographic preparation and testing of thermal spray coatings: Fine grinding and polishing, TSS committee on accepted practices. *Journal of Thermal Spray Technology* 15 (2): 174–176.
- Schajer, G.S. 1988. Measurement of non-uniform residual stress using the hole drilling method. Part 1. *Journal of Engineering Materials and Technology* 110 (4): 338–343, Part 2. 110(4):345–349.
- Schajer, G.S., and E. Altus. 1996. Stress calculation error analysis for incremental hole drilling residual stress measurement. *Journal of Engineering Materials and Technology* 118 (1): 120–126.
- Schmidt, G., and S. Steinhäuser. 1996. Characterization of wear protective coatings. *Tribology International* 29 (3): 207–214.
- Scrivani, A., G. Rizzi, U. Bardi, C. Giolli, M. Muniz Miranda, S. Ciattini, A. Fossati, and F. Borgioli. 2007. Thermal fatigue behavior of thick and porous thermal barrier coatings systems. *Journal of Thermal Spray Technology* 16 (5–6): 816–821.
- Scrivani, A., G. Rizzi, and C.C. Berndt. 2008. Enhanced thick thermal barrier coatings that exhibit varying porosity. *Materials Science and Engineering A* 476: 1–7.
- Shepard, S.M. 2001. Advances in pulsed thermography. In *Proceedings of SPIE, Thermo sense XXIII, Orlando, FL, USA, 16–19 April 2001*, pp. 511–515.
- Shivamurthy, R.C., M. Kamaraj, R. Nagarajan, S.M. Shariff, and G. Padmanabham. 2010. Slurry erosion characteristics and erosive wear mechanisms of Co-based and Ni-based coatings formed by laser surface alloying. *Metallurgical and Materials Transactions A: Physical Metallurgy and Materials Science* 41A: 470–486.
- Shrestha, S., A. Neville, and T. Hodgkiess. 2001. The effect of post-treatment of a high-velocity oxy-fuel Ni-Cr-Mo-Si-B coating. Part I: Microstructure/corrosion behavior relationships. *Journal of Thermal Spray Technology* 10 (3): 470–479.
- Sidhu, T.S., S. Prakash, and R.D. Agrawal. 2006a. Hot corrosion resistance of high-velocity oxyfuel sprayed coatings on a nickel-base superalloy in molten salt environment. *Journal of Thermal Spray Technology* 15 (3): 387–399.
- . 2006b. Characterizations and hot corrosion resistance of Cr₃C₂-NiCr coating on Ni-base superalloys in an aggressive environment. *Journal of Thermal Spray Technology* 15 (4): 811–816.
- . 2007. Study of molten salt corrosion of high velocity oxy-fuel sprayed cermet and nickel-based coatings at 900 °C. *Metallurgical and Materials Transactions A: Physical Metallurgy and Materials Science* 38A: 77–85.
- Siebert, B., C. Funke, R. Vaßen, and D. Stöver. 1999. Changes in porosity and Young's modulus due to sintering of plasma sprayed thermal barrier coatings. *Journal of Materials Processing Technology* 92–93: 217–223.
- Singh, H., D. Puri, and S. Prakash. 2005. Corrosion behavior of plasma-sprayed coatings on a Ni-base superalloy in Na₂SO₄-60 Pct V₂O₃ environment at 900 °C. *Metallurgical and Materials Transactions A: Physical Metallurgy and Materials Science* 36A: 1008–1015.
- Slifka, A.J., B.J. Filla, J.M. Phelps, G. Bancke, and C.C. Berndt. 1998. Thermal conductivity of a zirconia thermal barrier coating. *Journal of Thermal Spray Technology* 7 (1): 43–46.
- Sorai, M., and N.N. Gakkai. 2004. *Comprehensive handbook of calorimetry and thermal analysis*, 534 p. New York: Wiley.
- Souza, V.A.D., and A. Neville. 2006. Mechanisms and kinetics of WC-Co-Cr high velocity oxy-fuel thermal spray coating degradation in corrosive environments. *Journal of Thermal Spray Technology* 15 (1): 106–117.
- Speyer, R. 1993. *Thermal analysis of materials*, Materials engineering. Seattle: Amazon.
- Stack, M.M., F.H. Stott, and G.C. Wood. 1993. Review of mechanisms of erosion-corrosion of alloys at elevated temperatures. Part 2. *Wear* 162–164: 706–712.
- Staia, M.H., E. Ramos, A. Carrasquero, A. Roman, J. Lesage, D. Chicot, and G. Mesmacque. 2000. Effect of substrate roughness induced by grit blasting upon adhesion of WC-17% Co thermal sprayed coatings. *Thin Solid Films* 377–378: 657–664.
- Stewart, S., R. Ahmed, and T. Itsukaichi. 2005. Rolling contact fatigue of post-treated WC – NiCrBSi thermal spray coatings. *Surface and Coating Technology* 190 (1–2): 171–189.
- Stokes, J., and L. Looney. 2008. Predicting quenching and cooling stresses within HVOF deposits. *Journal of Thermal Spray Technology* 17 (5–6): 908–914.
- Strunz, P., G. Schumacher, R. Vaßen, and A. Wiedenmann. 2004. In situ SANS study of pore microstructure in YSZ thermal barrier coatings. *Acta Materialia* 52: 3305–3312.
- Sundararajan, G., N.M. Chavan, G. Sivakumar, and P. Sudharshan Phani. 2010. Evaluation of parameters for assessment of inter-splat bond strength in cold-sprayed coatings. *Journal of Thermal Spray Technology* 19 (6): 1255–1266.
- Taha-al, Z.Y., M.S. Hashmi, and B.S. Yilbas. 2009. Effect of WC on the residual stress in the laser treated HVOF coating. *Journal of Materials Processing Technology* 209: 3172–3181.

- Tan, Y., J.P. Longtin, and S. Sampath. 2006. Modeling thermal conductivity of thermal spray coatings: Comparing predictions to experiments. *Journal of Thermal Spray Technology* 15 (4): 545–552.
- Théry, P.-Y., M. Poulain, M. Dupeux, and M. Braccini. 2007. Adhesion energy of a YPSZ EB-PVD layer in two thermal barrier coating systems. *Surface and Coating Technology* 202: 648–652.
- Tiana, W., Y. Wang, T. Zhang, and Y. Yang. 2009. Sliding wear and electrochemical corrosion behavior of plasma sprayed nanocomposite Al_2O_3 -13% TiO_2 coatings. *Materials Chemistry and Physics* 118: 37–45.
- Tillmann, W., E. Vogli, and B. Krebs. 2008a. Influence of the spray angle on the characteristics of atmospheric plasma sprayed hard material-based coatings. *Journal of Thermal Spray Technology* 17 (5–6): 948–955.
- Tillmann, W., E. Vogli, I. Baumann, G. Matthaeus, and T. Ostrowski. 2008b. Influence of the HVOF gas composition on the thermal spraying of WC-Co submicron powders (28 + 1 μm) to produce superfine structured cermet coatings. *Journal of Thermal Spray Technology* 17 (5–6): 924–932.
- Tillmann, W., B. Klusemann, J. Nebel, and B. Svendsen. 2011. Analysis of the mechanical properties of an arc-sprayed WC-FeCSiMn coating: Nanoindentation and simulation. *Journal of Thermal Spray Technology* 20 (1–2): 328–335.
- Tjitra Salim, N., M. Yamada, H. Nakano, K. Shima, H. Isago, and M. Fukumoto. 2011. The effect of post-treatments on the powder morphology of titanium dioxide (TiO_2) powders synthesized for cold spray. *Surface and Coating Technology* 206: 366–371.
- Underwood, E.E. 1970. *Quantitative stereology*. Reading: Addison-Wesley.
- Valente, T., C. Bartuli, M. Sebastiani, and A. Loreto. 2005. Implementation and development of the incremental hole drilling method for the measurement of residual stress in thermal spray coatings. *Journal of Thermal Spray Technology* 14 (4): 462–470.
- Van Brakel, J., S. Modrý, and M. Svatá. 1981. Mercury porosimetry: State of the art. *Powder Technology* 29 (1): 1–12.
- Van der Voort, G.F. 1999. *Metallography principles and practice*, Material science and engineering series. Materials Park: ASM International.
- Vander Voort, George, ed. 2004. *ASM handbook*, Metallography and microstructures, vol. 09, 1184 p. Materials Park: ASM International.
- Venkataraman, R., G. Das, S.R. Singh, L.C. Pathak, R.N. Ghosh, B. Venkataraman, and R. Krishnamurthy. 2007. Study on influence of porosity, pore size, spatial and topological distribution of pores on microhardness of as plasma sprayed ceramic coatings. *Materials Science and Engineering A* 445–446: 269–274.
- Volenk, K., F. Hanousek, P. Chraska, J. Ilavsky, and K. Neufuss. 1999. In-flight oxidation of high-alloy steels during plasma spraying. *Materials Science and Engineering A* 272: 199–206.
- Voyer, J., F. Gitzhofer, and M.I. Boulos. 1998. Study of the performance of TBC under thermal cycling conditions using an acoustic emission rig. *Journal of Thermal Spray Technology* 7: 181–190.
- Wallace, J.S., and J. Ilavsky. 1998. Elastic modulus measurements in plasma sprayed deposits. *Journal of Thermal Spray Technology* 7 (4): 521–526.
- Walpole, R.E., and R.H. Myers. 1978. *Probability and statistics for engineers and scientists*, 2nd ed. New York: Macmillan.
- Wang, H.-P. 1979. The alignment error of the hole-drilling method. *Experimental Mechanics* 19: 23–27.
- Wang, H., and R.B. Dinwiddie. 2000. Reliability of laser flash thermal diffusivity measurements of the thermal barrier coatings. *Journal of Thermal Spray Technology* 9 (2): 210–214.
- . 2004. Development of a lab view based portable thermal diffusivity system. In *Thermal conductivity 27, thermal expansion 15*, ed. H. Wang, 484–492. Lancaster: DESTech.
- Wang, Z., A. Kulkarni, S. Deshpande, T. Nakamura, and H. Herman. 2003. Effects of pores and interfaces on effective properties of plasma sprayed zirconia coatings. *Acta Materialia* 51: 5319–5334.
- Wang, H.-R., B.-R. Hou, J. Wang, Q. Wang, and W.-Y. Li. 2008. Effect of process conditions on microstructure and corrosion resistance of cold-sprayed Ti coatings. *Journal of Thermal Spray Technology* 17 (5–6): 736–741.
- Wang, J., E.H. Jordan, and M. Gell. 2010. Plasma sprayed dense MgO - Y_2O_3 nanocomposite coatings using sol-gel combustion synthesized powder. *Journal of Thermal Spray Technology* 19 (5): 873–878.
- Washburn, E.W. 1921. The dynamics of capillary flows. *Physics Review* 17: 273–283.
- Watanabe, M., S. Kuroda, K. Yokoyama, T. Inoue, and Y. Gotoh. 2008. Modified tensile adhesion test for evaluation of interfacial toughness of HVOF sprayed coatings. *Surface and Coating Technology* 202: 1746–1752.
- Westergård, R., N. Axén, U. Wiklund, and S. Hogmark. 2000. An evaluation of plasma sprayed ceramic coatings by erosion, abrasion and bend testing. *Wear* 246: 12–19.
- Wielage, B., S. Steinhäuser, T. Schnick, and D. Nickelmann. 1999. Characterization of the wear behavior of thermal sprayed coatings. *Journal of Thermal Spray Technology* 8 (4): 553–558.
- Wigren, J. and J. Johansson. 2011. Improving reliability of thermal spray coatings in production environment. In Presented at 3rd plasma round table, 31 October–4 November 2011, South Africa.
- Wigren, J., and K. Täng. 2007. Quality considerations for the evaluation of thermal spray coatings. *Journal of Thermal Spray Technology* 16 (4): 533–540.
- Williams, D.B., and C.B. Carter. 2009. *Transmission electron microscopy*, 2nd ed. New York: Springer.
- Wittmann-Ténéze, K., N. Caron, and S. Alexandre. 2008. Gas permeability of porous plasma-sprayed coatings. *Journal of Thermal Spray Technology* 17 (5–6): 902–907.
- Xie, Y., and H.M. Hawthorne. 2001. A model for compressive coating stresses in the scratch adhesion test. *Surface and Coating Technology* 141: 15–25.
- Xie, X.Y., H.B. Guo, and S.K. Gong. 2010. Mechanical properties of $\text{LaTi}_2\text{Al}_9\text{O}_{19}$ and thermal cycling behaviors of plasma sprayed $\text{LaTi}_2\text{Al}_9\text{O}_{19}$ /YSZ thermal barrier coatings. *Journal of Thermal Spray Technology* 19 (6): 1179–1185.
- Xu, G.-Z., J.-J. Liu, and Z.-R. Zhou. 2002. The effect of the third body on the fretting wear behavior of coatings. *Journal of Materials Engineering and Performance* 11 (3): 288–293.
- Yan, L., Y. Leng, and J. Chen. 2003. Torsional fatigue resistance of plasma sprayed HA coating on Ti-6Al-4V. *Journal of Materials Science. Materials in Medicine* 14: 291–295.
- Yan, D., Y. Dong, Y. Yang, L. Wang, X. Chen, J. He, and J. Zhang. 2011. Microstructure characterization of the FeAl_2O_4 -based nanostructured composite coating synthesized by plasma spraying $\text{Fe}_2\text{O}_3/\text{Al}$ powders. *Journal of Thermal Spray Technology* 20 (6): 1269–1277.
- Yang, G., H. Zu-kun, X. Xiaolei, and X. Gang. 2001. Formation of molybdenum boride cermet coating by the detonation spray process. *Journal of Thermal Spray Technology* 10 (3): 456–460.
- Yanga, Q., T. Senda, and A. Hirose. 2006. Sliding wear behavior of WC-12% Co coatings at elevated temperatures. *Surface and Coating Technology* 200: 4208–4212.
- Ye, F.-X., S.-H. Wu, and A. Ohmori. 2008. Microstructure and oxidation behavior of Cr₃Ni₇C cermet coatings deposited by diamond jet spray process. *Journal of Thermal Spray Technology* 17 (5–6): 942–947.
- Yin, B., G. Liu, H. Zhou, J. Chen, and F. Yan. 2010. Sliding wear behavior of HVOF-sprayed Cr_3C_2 -NiCr/CeO₂ composite coatings at elevated temperature up to 800 °C. *Tribology Letters* 37: 463–475.

- Zhang, J., and V. Desai. 2005. Evaluation of thickness, porosity and pore shape of plasma sprayed TBC by electrochemical impedance spectroscopy. *Surface and Coating Technology* 190: 98–109.
- Zhang, D.-W., and T.C. Lei. 2003. The microstructure and erosive–corrosive wear performance of laser-clad Ni–Cr3C2 composite coating. *Wear* 255: 129–133.
- Zhang, T., and D.Y. Li. 2001. Improvement in the resistance of aluminum with yttria particles to sliding wear in air and in a corrosive medium. *Wear* 251: 1250–1256.
- Zhang, X.C., B.S. Xu, S.T. Tu, F.Z. Xuan, H.D. Wang, and Y.X. Wu. 2009a. Fatigue resistance and failure mechanisms of plasma-sprayed CrC–NiCr cermet coatings in rolling contact. *International Journal of Fatigue* 31: 906–915.
- Zhang, X.C., B.S. Xu, F.Z. Xuan, H.D. Wang, Y.X. Wu, and S.T. Tu. 2009b. Statistical analyses of porosity variations in plasma-sprayed Ni-based coatings. *Journal of Alloys and Compounds* 467: 501–508.
- Zhang, X.C., B.S. Xu, F.Z. Xuan, H.D. Wang, and Y.X. Wu. 2009c. Microstructural and porosity variations in the plasma-sprayed Ni-alloy coatings prepared at different spraying powers. *Journal of Alloys and Compounds* 473: 145–151.
- Zhao, X.B., and Z.H. Ye. 2012. Microstructure and wear resistance of molybdenum based amorphous nanocrystalline alloy coating fabricated by atmospheric plasma spraying. *Surface and Coating Technology* 228: S226–S270.
- Zhao, Y., L. Lin, X.M. Li, and M.K. Lei. 2010. Simultaneous determination of the coating thickness and its longitudinal velocity by ultrasonic nondestructive method. *NDT and E International* 43: 579–585.
- Zhou, Y.C., and T. Hashida. 2002. Thermal fatigue failure induced by delamination in thermal barrier coating. *International Journal of Fatigue* 24: 407–417.
- Zhu, S., R.H. Pelton, and K. Collver. 1995. Mechanistic modelling of fluid permeation through compressible fiber beds. *Chemical Engineering Science* 50 (22): 3557–3572.
- Zhu, D., S.R. Choi, and R.A. Miller. 2004. Development and thermal fatigue testing of ceramic thermal barrier coatings. *Surface and Coating Technology* 188–189: 146–152.